Modelling of transformations during induction hardening and tempering

Daniel Gaude-Fugarolas
Corpus Christi College
Cambridge

A dissertation submitted for the Doctor of Philosophy degree at the University of Cambridge.

PREFACE

This dissertation is submitted for the degree of Doctor of Philosophy at the University of Cambridge. The research described herein was conducted under the supervision of Professor H. K. D. H. Bhadeshia in the Department of Materials Science and Metallurgy, University of Cambridge, between October 1999 and October 2002.

This work is to my best knowledge original, except where acknowledgements and references are made to previous work. Neither this, nor any substantially similar dissertation has been or is being submitted for any other degree, diploma or other qualification at any other university. This dissertation contains less than 60,000 words.

Part of this work has been presented in the following publications:

1. D. Gaude-Fugarolas, and H. K. D. H. Bhadeshia. *A model for austenitisation of hypoeutectoid steels.* Unpublished; submitted to Journal of Materials Science.

2. D. Gaude-Fugarolas *Phase transformations in steel during induction hardening.* International Conference: "Mathematical Modelling and Information Technologies in Welding and Related Processes", Katsiveli, Crimea, Ukraine (16-20 September 2002). In press.

Daniel Gaude i Fugarolas

October 2002

ACKNOWLEDGEMENTS

I am indebted to Professors D. J. Fray and A. H. Windle for the provision of laboratory facilities in the Department of Materials Science and Metallurgy of Cambridge. I would like to express my sincere gratitude to my supervisor Professor H. K. D. H. Bhadeshia for his guidance, knowledge and great enthusiasm.

I am indebted to GKNT Ltd. for funding this project, and in particular to Dr. Nick Hurd, Dr. Graham Hollox and Dr. John Garnham for their valuable comments and input throughout the project.

I would also like to thank the past and present members of the Phase Transformations and Complex Properties Research Group for their help and friendship, in particular, Pedro Rivera, Carlos Garcia Mateo, John Street, Thomas Sourmail, Vicky Yardley, Philippe Opdenacker, Shingo Yamasaki, Miguel Yescas, Yann de Carlan, Gareth Hopkin, Francisca Caballero, Carlos Capdevila, Harsha Lalam, Marimuthu Murugananth, Mathew Peet, Dominique Carrouge, Frank Tancret and Yanhong Wei; as well as Ton van Helvoort for his friendship and lengthy scientific discussions; and Kevin Roberts, David Vowles, and John Carter and his team for their help, pacience and advise. It was an enormous pleasure to work with them.

Thanks also to my friends and to the people I met both in Corpus Christi College and other Colleges and outside the University during my time in Cambridge.

Finally, I take this opportunity to express my gratitude to my family for their unfailing encouragement and support, specially my parents Ma.Teresa and Antonio.

ABSTRACT

There are many circumstances in industry where steel components are locally heated into the austenite phase field, and then quenched rapidly to produced a hardened region. Induction hardening is one such process used widely in the manufacture of automobile components, in particular to enhance the wear and contact–fatigue resistance of rubbing surfaces.

One critical component of this kind is the so–called *constant velocity joint* (CVJ), which allows the transmission of engine–torque to wheels which can be steered over rough surfaces. The components are complex in shape and have to be mass–produced with impressive reliability. The motivation for the work presented in the thesis was to create and validate a model which describes the evolution of microstructure following the induction hardening and subsequent low–temperature tempering of the sort of steels used in the manufacture of CVJs. However, many aspects of the work are of general relevance to the theory for phase transformations in steels.

The thesis begins with an introduction and a review of phase transformations in steels, with Chapter 3 focusing on the formation of austenite, a process which is an integral part of induction hardening. Induction hardened components frequently have to be tempered in order to enhance the long–term properties. Tempering is therefore reviewed in Chapter 4, followed by a review of neural network analysis, a technique exploited in the modelling of tempering later in the thesis.

The work done to model the complex heating and cooling cycles involved in induction treatment is described in Chapter 6, including an analytical approach which captures the essence of the process and a finite–difference method which is a more precise representation of the complexity.

A theory has been developed for the formation of austenite from a mixture of ferrite and pearlite and the results have been compared against new experimental data in Chapter 7. Many components are in practice in a cold–deformed state prior to austenitisation. The

effect of deformation on austenite formation has been investigated using dilatometry. Two interesting principles emerge from this work. Firstly, slow heating can stabilise the initial microstructure such that austenite formation is retarded. Secondly, the combined effects of heating rate on the initial microstructure and on the kinetics of thermally activated processes, can lead to a minimum in the austenite–start temperature as a function of the heating rate. Otherwise, deformation accelerates transformation by adding to the stored energy in the initial microstructure.

A comprehensive phase–transformations model describing the transformations that occur during the cooling of austenite is presented in Chapter 9. This model integrates previous work and hence allows the calculation of continuous cooling transformation diagrams, including all the major phases that occur in steels (allotriomorphic ferrite, pearlite, Widmanstätten ferrite, bainite, martensite and retained austenite).

Finally, an interesting neural network model containing sound phase transformations theory is presented in Chapter 10, a model which captures the details on low–temperature tempering processes as far as martensite is concerned. The totality of models described in the thesis (thermal cycle, austenitisation, transformations during cooling, tempering) in effect provides a full representation of the induction hardening process. The thesis finishes with a summary and some suggestions for future work, together with appendices documenting the computer software.

Notation

a_c	-	Number of atoms in a nucleus of critical size which are at the interface
A_{c1}	-	Lower critical temperature of transformation to austenite
A_{c3}	-	Higher critical temperature of transformation to austenite
A_i	-	Area i
Bi	-	Biot number $= \frac{h\,L}{k}$
B_s	-	Bainite-start temperature
c	-	Carbon content of a steel
c^{α}	-	Carbon content of ferrite
$c^{\alpha\gamma}$	-	Carbon content of ferrite in paraequilibrium with austenite
$c^{\gamma\alpha}$	-	Carbon content of austenite in paraequilibrium with ferrite
$c^{\gamma\theta}$	-	Carbon content of austenite at the interface with cementite
C_X	-	Constant
C_p	-	Specific heat
d_{max}	-	Maximum diffusion distance
d_{α}	-	Thickness of ferrite lamella in pearlite
d_{θ}	-	Thickness of cementite lamella in pearlite
dr	-	Coordinate axis direction in spherical symetry
$d\phi$	-	Coordinate axis direction in spherical symetry
$d\varphi$	-	Coordinate axis direction in spherical symetry
D	-	Diffusion coefficient
D_{α}	-	Diffusion coefficient of carbon in ferrite
$D_{\alpha'}$	-	Diffusion coefficient of carbon in martensite
$\bar{D}$	-	Average diffusion coefficient
$\bar{D}$	-	Corrected 3-dimensional intersect diameter
Δf^*	-	Zenner ordering term
Fo	-	Fourier number $= \frac{k\ t}{\rho\ C_p\ L^2}$
ΔF_m^V	-	Maximum free energy change acompanying the formation of a nucleus

g	-	Geometrical constant
G	-	Growth rate
G	-	Gibbs free energy
G^*	-	Activation free energy for nucleation
G_i^0	-	Gibbs free energy of pure substance i
G_{mix}^i	-	Gibbs free energy of ideal mixing
G_{mix}^{ni}	-	Gibbs free energy of non-ideal mixing or excess Gibbs energy of mixing
G_{max}^p	-	Maximum driving energy available for nucleation
G_N	-	Minimum free energy change to nucleate Widmanstätten ferrite or bainite
G_{SB}	-	Stored energy of bainite
G_t^*	-	Activation energy for the transfer of atoms across an interface
$G_{\gamma\beta}$	-	Gibbs free energy difference between phases γ and β
k	-	Boltzman constant
k	-	Thermal conductivity
h	-	Heat transfer coefficient
h	-	Planck constant
h	-	Output of a node of the hidden layer of a neural network
H	-	Severity of quench
H	-	Hardness
H_F	-	Hardness of fully tempered martensite
H^T	-	Hardness after tempering at temperature T
$H_{\alpha'}$	-	Hardness of as-quenched martensite
ΔH_{mix}	-	Enthalpy increase of mixing
$\Delta_f H$	-	Enthalpy of formation
I	-	Nucleation rate per unit time
l	-	Extension on a constent velocity joint
$\bar{l}$	-	Linear intersect
l_{col}	-	Pearlite colony diameter
$2l_e$	-	Thickness of a ferrite and cementite lamini pair in pearlite
l_h	-	$= l_\alpha + l_p$

$2l_p$ - Thickness of pearlite regions in banded steel

$2l_\alpha$ - Thickness of plate-like ferrite grains in banded steel

$2L$ - Thickness of a plate

m - Spatial node number

m - Constant

M_s - Martensite-start temperature

n - Constant

n_c - Number of atoms in a nucleus of critical size

N - Number density of of nucleation sites

$\dot{N}$ - Nucleation rate

$\tilde{N}$ - Number density of of available nuclei

$N+1$ - Number of spatial nodes considered in heat transfer model

N_0 - Number of nucleation sites per unit volume

N_a - Avogadro number

O_B - Planar boundary with the total grain boundary area per unit volume in an alloy

$Oven$ - Parameter to differentiate between oven and induction tempering

$\Delta O_{y,j}$ - Change in real area intersected with the plane at distance y by phase j

p - Péclet number

P - Parameter used during numerical integration

P - Pearlite

P_{XY} - Number of atomic bonds between species X and Y

$\dot{q}$ - Surface heat flux

$\tilde{q}$ - Normalised heat flux

q_i - Half thickness of disc of phase i

Q - Activation energy

Q_D - Activation energy for diffusion

Q_F - Generic activation energy for nucleation or growth

Q_I - Activation energy for nucleation

Q_G - Activation energy for growth

r - Normalised position along the radius of a cylinder

r	-	Radius
r	-	Position
r_c	-	Critical radius of stable nucleus
r^{int}	-	Position of the interface
r_θ	-	Radius of cementite spheroid
R	-	Gas constant
R_i	-	Radius i
s	-	Ratio of spontaneous magnetisation in iron at T K to that at 0 K
S_{298}	-	Entropy at 298 K
S_D	-	Activation entropy for diffusion
ΔS_{mix}	-	Increase in configurational entropy of mixing
t	-	Time
T	-	Temperature
T_q	-	Temperature of quench
T_0	-	Curve that describes the locus of points on the phase diagram where ferrite and austenite of the same composition have the same free energy
$\Delta T_{mag,i}$	-	Magnetic contribution of element i to the shift in temperature at which the free energy for transformation is calculated with respect to pure iron
$\Delta T_{nmag,i}$	-	Non-magnetic contribution of element i to the shift in temperature at which the free energy for transformation is calculated with respect to pure iron
u	-	Normalised temperature
U_c	-	Energy needed to move a carbon atom to a neighbouring site in martensite
v	-	Volume fraction
$\dot{v}^\beta$	-	Transformation rate to phase β
x	-	Normalised position within a plate
$\triangle x$	-	Spatial step or node thickness
x_i	-	Atomic fraction of component i
x_C	-	Amount of carbon precipitated to form carbides whithin bainitic ferrite
x_{T_0}	-	Carbon concentration of austenite when it aproaches the T_0 curve
$x^{\gamma\alpha}$	-	Carbon concentration at the interface between γ and α

X^e - Extended value of X

y - Distance from boundary

y_i^j - Site fraction of component i in sub-lattice j

Y_i - Mole fraction of substitutional element i

v - Temporal step number $0 \leq$ v

v^{int} - Velocity of interface

v_β - Volume fraction of phase β

V - Volume

V_m - Molar volume of ferrite

w_C - Average weigth percent of carbon in an alloy

W_s - Widmanstätten-start temperature

z - Coordination number

α - Ferrite

α - Thermal diffusivity $= \frac{k}{\rho\ C_p}$

α' - Martensite

β - Arbitrary phase

γ - Austenite

Γ - Capilarity constant

Γ_C - Activity coefficient of carbon in austenite

ε - True strain

ε - $= \varepsilon_{AB} - \frac{1}{2}(\varepsilon_{AA} + \varepsilon_{BB})$

ε_{AB} - Bond energy between atoms A and B

σ - Standard deviation

σ_ν - Perceived level of noise in the database

$\sigma_{\gamma\beta}$ - Surface energy of interface between phases γ and β

ρ - Density

$\triangle\theta$ - Normalised time step $= Fo$

θ - Cementite

θ_i - Angle i

$\theta_i^{(j)}$ - Constant of node i of the hidden layer of a neural network

Θ	-	Hyperparameters of a Gaussian process
$\xi\{T,t\}$	-	Normalised hardness
$\xi\{T,t\}$	-	Volume fraction of cementite, normalised by its equilibrium volume fraction
ψ_i	-	One-dimensional parabolic thickening rate constant for phase i
τ	-	Incubation time
τ	-	Nucleation time
τ_c	-	Time required to nucleate a nucleus of critical size
ω	-	$= \frac{N_a z}{2}(2\varepsilon_{AB} - \varepsilon_{AA} - \varepsilon_{BB})$
$\omega_i^{(j)}$	-	Weigth of node i of the hidden layer of a neural network
ω_γ	-	Pairwise interaction energy between nearest neighbour carbon atoms in austenite

Contents

Chapter 1

General introduction

The work described in this thesis began with the aim of understanding and producing a quantitative description of the process of induction hardening, as applied in the production of *constant velocity joints*. These components, which are described later, are mass-produced and form a safety-critical feature of most modern cars.

1.1 Constant velocity joint

A constant velocity joint is a component that transfers a torque on a shaft over several degrees of freedom without a change in rotational speed. The joints are used mainly in front-wheel drive automobiles, in which the shaft transferring the torque from the engine, past the gear box onto the front wheels, has to be articulated to allow the travel of the wheel along the suspension and at the same time permit steering of the car, as shown in Figure 1.1 [1].

The complete joint is a complex mechanical assembly, which has to withstand a severe combination of loads. The main components of the *outer race*, which is the external articulation of the component and the specific loads applied to each of them are shown in Figure 1.3 [2].

The work done during this thesis has been aimed at the study of the microstructural changes during the manufacturing process of a generic structural component, but in the cases in which specific information about the alloy, manufacturing process and heat treatments have been needed, the *outer race bell* (Figure 1.2) of the constant velocity joint has been taken as a reference.

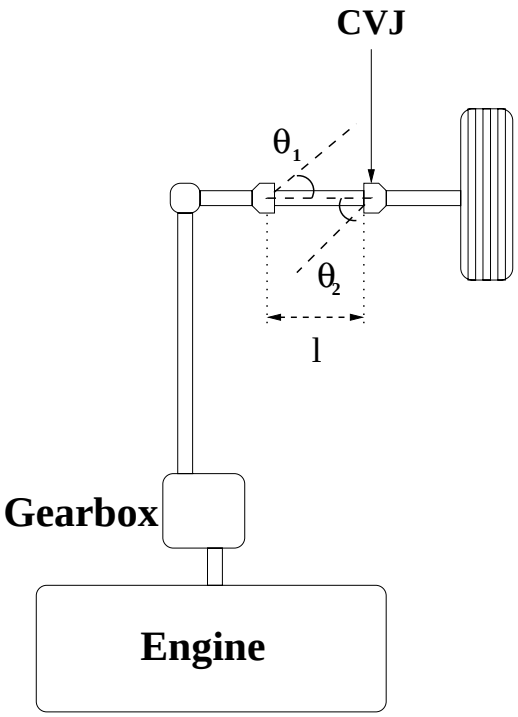

Figure 1.1: Position of a constant velocity joint in the shaft that transmits the torque from the engine to the wheels in a front-wheel drive car.

Figure 1.2: *Outer race bell* of a constant velocity joint.

1.2 Manufacturing route

The details of the manufacturing process for constant velocity joints differ across the industry, but share the same general structure. What follows is a description of the most general manufacturing process of an outer race bell [2].

A range of steels is used to manufacture outer races for constant velocity joints, although the most common is a *manganese-carbon steel*, chosen specifically for induction hardening. There is a high carbon content within the hypoeutectoid range to obtain hard martensite. Small additions of hardenability-enhancing elements such as chromium, nickel and molybdenum are also common. The composition of an average steel is shown in Table 1.1. The steel is usually supplied in the form of billets or long bars of rolled metal,

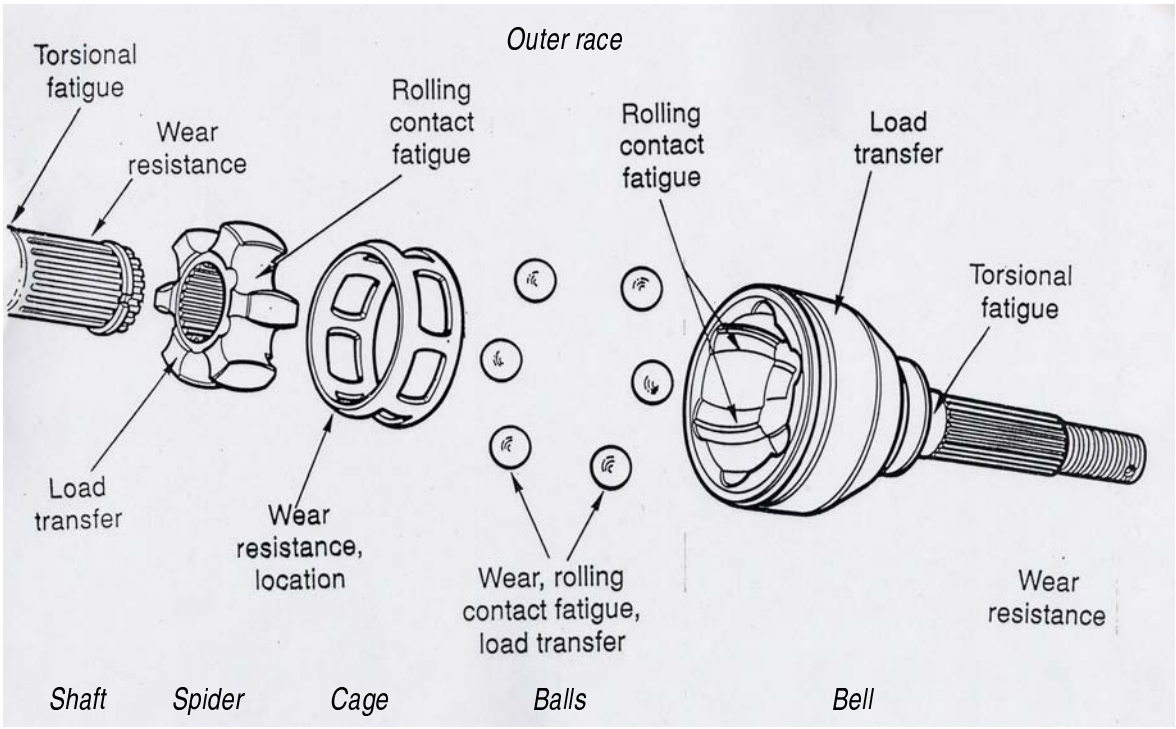

Figure 1.3: Schematic view of the components of the outer race of a constant velocity joint, with information about the loads applied to each of them. Plot reproduced from [2].

i.e., ideal shapes for the forming processes involved in making of the outer race bells.

wt.%	**C**	**Si**	**Mn**	**Cr**	**Ni**	**Mo**
UC1	0.52	0.21	0.75	0.19	0.07	0.04

Table 1.1: Composition of an average steel used for constant velocity joints.

The first operation performed on the billet is the cutting of the bar into pieces of the correct size to be forged. Prior to forging, the workpiece is first heated to around 100°C and coated with graphite. It is then heated to the working temperature and fed into the forge.

The first forming steps can be either hot (1250°C) or warm (920°C) forging. Hot-forging is completed in a single step, followed by cooling to ambient temperature and reaustenitisation at 850-900°C to obtain a finer austenite grain size, before cooling in air (*normalising*). Warm-forging is more common; it requires four stages of deformation but a better finish is achieved and the life of the forging die is lengthened. After warm-forming, the component is also normalised.

Following forging, there are two further steps of cold-forming performed on the component, to achieve the accurate dimensions needed before machining operations. The surfaces that require accurate dimensions are machined at this point of the process.

Some of the surfaces of the component need higher hardness and resistance to wear. To achieve this hardness, a layer of martensite is created in the appropriate locations by induction hardening.

Induction hardening is a process in which the surface of the metal is heated for a short period of time to around 1000°C by electric currents induced via an alternating magnetic field. The component is then cooled down rapidly with water sprays, thereby quenching sufficiently rapidly to induce martensitic transformation. If necessary, polymer quench additives are added to the cooling water to enhance the severity of the quench.

After quenching, the component is tempered in order to reduce some of the stresses produced during the quenching operation. The tempering can be conducted using an oven

at 150-200°C for about an hour, although induction tempering is beginning to become popular.

The final operations are labelling the component and assembly of all the parts of the constant velocity joint, adding lubrication grease, protection rubber cap and packing.

1.3 Modelling strategy

In order to model the evolution of the microstructure of an alloy used for a structural component, a modular approach has been selected. The complete modelling process has been divided in four submodels, each associated with a specific part of the manufacturing process (Figure 1.4).

The initial microstructure is that obtained after the normalising heat treatment. Cold sizing, induction hardening and tempering are the only thermo-mechanical treatments that define the final microstructure and properties of the component. Therefore, the four independent submodels needed by the model describe temperature evolution, austenitisation of a hypoeutectoid steel, cooling/quench, and low temperature tempering.

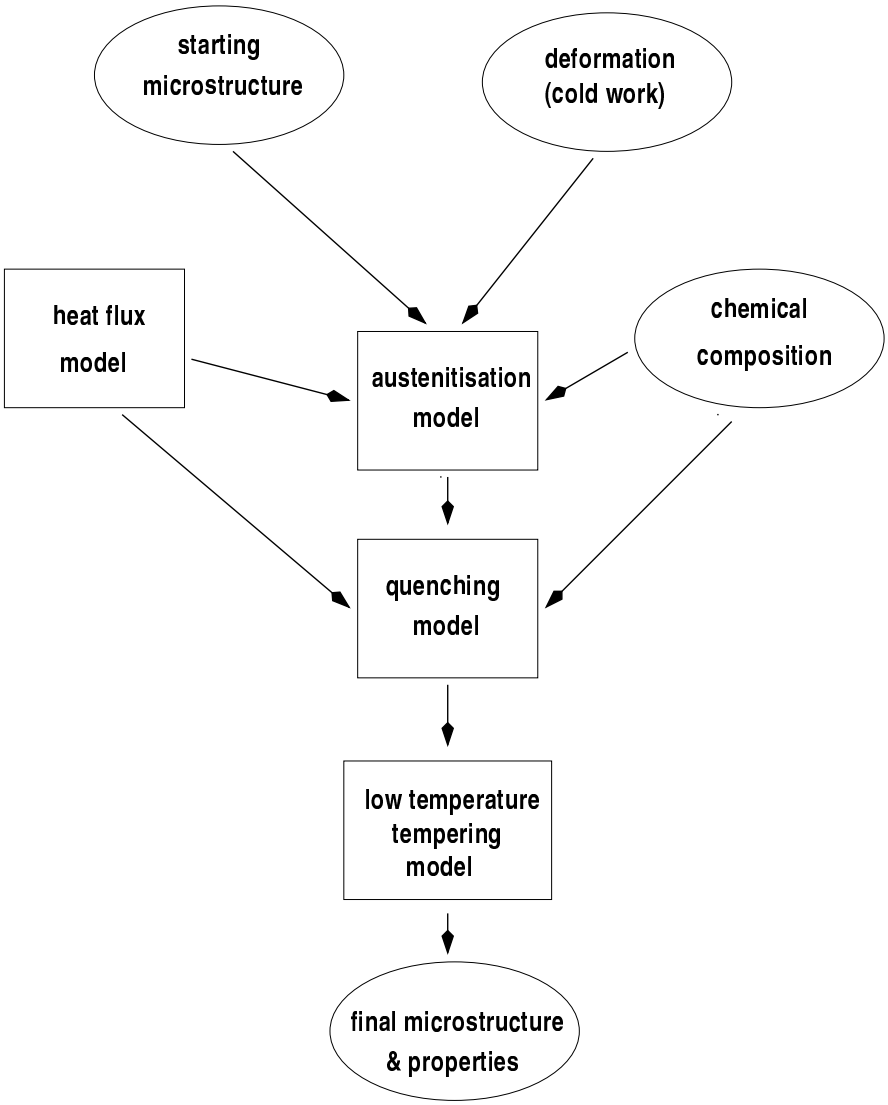

Figure 1.4: Structure of the model on phase transformations during manufacture. The ellipses represent inputs of information and the boxes the independent submodels.

Chapter 2

General phase transformation theory

2.1 Thermodynamic calculations

The ability to calculate the thermodynamic stability of phases is vital in the study of phase transformations. One of the traditional approaches has been the use of empirically determined *phase diagrams*. Phase diagrams have undoubted academic importance to depict the basic regions of phase stability for two (up to three) component systems but they offer seriously limited information when dealing with real, multicomponent systems.

A modern approach to the representation of phase stability involves the calculation of the Gibbs energy of all the possible combinations of phases and the determination of the stable mixtures via the minimisation of Gibbs energy. The Gibbs energy of each phase is determined from its composition, and the temperature and pressure of the system. The CALPHAD method (CALculation of PHAse Diagrams) allows the extrapolation of thermodynamic properties in complex multicomponent systems, transforming the thermodynamic problem into a purely, although still complex, mathematical one. The CALPHAD method uses the SGTE (Scientific Group Thermodata Europe) databases, and is implemented in commercial thermodynamic software packages like MTDATA or ThermoCalc [3, 4, 5].

There are various models used in the determination of the Gibbs energy of phases of different characteristics. The following sections contain an introduction to some of the basic thermodynamic models in use. This section is essentially based on references [3, 4, 5].

2.1.1 Pure substances

The Gibbs energy of a stoichiometric compound can be determined from the heat capacity C_P. The heat capacity is represented using polynomials of the type:

$$C_P\{T\} = A + BT + CT^2 + DT^{-2} \tag{2.1}$$

the parameters A, B, C and D have been determined and are stored in the SGTE databases

as a function of temperature intervals. The SGTE databases also store values of enthalpy of formation $\Delta_f H$ for the substance concerned and of the entropy S_{298} at 298 K.

2.1.2 Random substitutional solutions

The Gibbs energy of a random solution, like a liquid metal, or solid solution can be determined by adding the Gibbs energy of its pure constituent elements, and then adding terms for the energy of mixing:

$$G = \sum_i x_i G_i^0 + G_{mix}^i + G_{mix}^{ni} \tag{2.2}$$

where G_i^0 is the contribution of the i^{th} pure component, x_i its atomic fraction and G_{mix}^i and G_{mix}^{ni} are the ideal and non-ideal mixing contributions. The latter is also known as the excess Gibbs energy of mixing.

2.1.2.1 Ideal solutions

This is the simplest case, in which $G_{mix}^{ni} = 0$. The interactions between the different constituents are identical and there is no enthalpy increase during the formation of the solution. The increase in Gibbs energy is solely due to an increase in configurational entropy ΔS_{mix}, which can be approximated as [4]:

$$\Delta S_{mix} \approx -R \sum_i (x_i \ln x_i) \tag{2.3}$$

where R is the gas constant. The Gibbs energy per mole of solution then becomes:

$$G = \sum_i x_i G_i^0 + RT \sum_i x_i \ln x_i \tag{2.4}$$

2.1.2.2 Regular and non-regular solutions

For most systems however, the interaction between components will produce a finite increase in enthalpy, and the reaction will be either exothermic or endothermic. The model

used for an ideal solution can be extended to include the enthalpy increase term by using the so called *regular solution* approach.

The regular solution model assumes that the change in entropy is as if the solution is random even though there is a finite enthalpy of mixing.

Consider a binary $A-B$ solution. The change in binding energy, ε, when an AA and a BB bond is broken to create AB bonds is:

$$\varepsilon = \varepsilon_{AB} - \frac{1}{2}(\varepsilon_{AA} + \varepsilon_{BB}) \tag{2.5}$$

If $\varepsilon = 0$ the solution is ideal and $\Delta H_{mix} = 0$. Otherwise, for small values of ε, the following approximation can be used:

$$\Delta H_{mix} = \omega x_A x_B \tag{2.6}$$

where $\omega = N_a z \varepsilon$, N_a is Avogadro's number, and z the coordination number of the structure. The Gibbs energy of mixing for a regular solution can be determined as:

$$G_{mix} = \omega x_A x_B + RT(x_A \ln x_A + x_B \ln x_B) \tag{2.7}$$

which generalised to a multicomponent system produces:

$$G = \sum_i x_i G_i^0 + RT \sum_i x_i \ln x_i + \sum_i \sum_{j>i} x_i x_j \omega_{ij} \tag{2.8}$$

The regular solution model presented above assumes that the interactions are not dependent of the actual composition, which is not true in most cases. The sub-regular model introduces a linear composition dependency and when generalised to any composition dependency can express H_{mix}^{ni} as:

$$H_{mix}^{ni} = \sum_i \sum_{j>i} x_i x_j \sum_k \omega_{ij}^k (x_i - x_j)^v \tag{2.9}$$

The values of ω_{ij}^{k} are stored in the SGTE databases.

2.1.3 Sub-lattice models

When the atoms in a substitutional solid solution are completely randomly arranged, all the possible atom positions are equivalent, and the probability that any given position in the lattice is occupied by an atom A is x_A, and similarly is x_B for B atoms, *etc.* However, there are many cases in which some atoms will occupy some specific positions in the lattice and not others, to the limit at which several coexisting *sub-lattices* can be identified. In these sorts of systems some elements mix in one of the sub-lattices, while some others do in another. One example of this is found considering the case of austenite in steel, in which elements such as carbon and nitrogen mix in the interstitial lattice while iron, silicon, magnesium, *etc* mix in the substitutional lattice.

In this situation, the calculation of the excess Gibbs energy G_{mix}^{ni} is performed considering the interactions between elements in the same and in different sub-lattices, and substituting mole fractions x_i for *site fractions* y_X^N, where the superindex N denotes the sub-lattice. Considering a system in which two substitutional elements A and B and two interstitial elements C and D coexist, and where $L_{X,Y:Z}^{0}$ is the lattice independent regular solution parameters, the entropy of mixing can be determined as:

$$G_{mix}^{ni} = y_A^1 y_B^1 y_C^2 L_{A,B:C}^0 + y_A^1 y_B^1 y_D^2 L_{A,B:D}^0 + y_C^2 y_D^2 y_A^1 L_{A:B,C}^0 + y_C^2 y_D^2 y_B^1 L_{B:C,D}^0 \qquad (2.10)$$

$L_{X,Y:Z}^{0}$ are expressed as a polynomial function of temperature and natural logarithms of temperature. As in previous cases, the coefficients for those functions are stored in the SGTE databases.

2.1.4 Limitations of the method

The CALPHAD method, implemented in software packages like MTDATA or Thermo-Calc, is one of the most powerful tools that can be used in the study of phase transforma-

tions. Its strength relies in the use of the SGTE databases but this is at at the same time its weakness, as such databases may sometimes have particular limitations. Indeed, the database may lack some information on the existence of some phase in a given system, or on the existence and solubility of some element in some phase (*i.e.* silicon in cementite), or of some missing parameters (*i.e.* interactions of boron in austenite), and therefore may produce unexpected or inaccurate results when doing calculations that involve one of those cases.

2.2 Classic kinetic theory

The study of the kinetics of phase transformations, especially in metals, has produced a great volume of scientific literature. Any comprehensive review must therefore be focused. In the present case, only the most important theories used in process modelling, especially those dealing with the quench processes, are taken into account.

2.2.1 Classical theory for homogeneous nucleation

At any temperature above absolute zero there small fluctuations in the movements of atoms. There is a definite probability that these fluctuations may rearrange a group of atoms in a different structure from that of the rest of the alloy. These atoms form a nucleus presenting an increase in Gibbs free energy with respect to the original arrangement $\Delta G_{\gamma\beta}$, with γ indicating the newly formed microstructure and β the initial one. In certain cases the new arrangement is thermodynamically more favourable that the initial one. When that is the case, every atom that jumps across the interface between both microstructures to join the more stable phase will reduce the overall energy of the system, and it will provide a driving force for the growth of the new phase. However, before that happens the nucleus of γ has to reach a critical size. The critical size is defined from the balance between the decrease in $\Delta G_{\gamma\beta}$ due to the formation of additional γ, and the increase in $\Delta G_{\gamma\beta}$ due to the increase in boundary surface. Considering a spherical nucleus with radius

r, $\Delta G_{\gamma\beta}$ can be determined as:

$$\Delta G_{\gamma\beta} = \frac{4\pi r^3}{3}\Delta G^V_{\gamma\beta} + 4\pi r^2 \sigma_{\gamma\beta} \tag{2.11}$$

where $\Delta G^V_{\gamma\beta}$ in the change in Gibbs energy per unit volume during the transition from β to γ and $\sigma_{\gamma\beta}$ is the interface energy between such phases. Once the nucleus reaches a critical size, it will tend to grow. Before that the trend will be towards redissolution. The critical radius r_c for the transition can be determined to be:

$$r_c = -\frac{2\sigma_{\gamma\beta}}{\Delta G^V_{\gamma\beta}} \tag{2.12}$$

and the activation energy of formation of such nucleus G^* is:

$$G^* = \frac{16\pi}{3}\frac{(\sigma_{\gamma\beta})^3}{(\Delta G^V_{\gamma\beta})^2} \tag{2.13}$$

A rate for homogeneous nucleation can then be derived by considering the frequency at which new atoms are added to the nucleus. If the frequency is taken to be kT/h, with k is the Boltzmann constant, T absolute temperature, h the Planck constant and N a number density of nucleation sites and G^*_t the activation energy for the transfer of atoms across the γ/β interface, the homogeneous nucleation rate I becomes [6]:

$$I = N\frac{kT}{h}\exp\left(-\frac{G^*}{RT}\right)\exp\left(-\frac{G^*_t}{RT}\right) \tag{2.14}$$

In most cases of solid solid transformations however, nucleation does not happen homogeneously, but heterogeneously, at defects of the microstructure, like grain boundaries, dislocations, *etc.*

2.2.2 Overall transformation kinetics

Regarding isothermal transformation involving nucleation, growth and impingement, early research by Kolmogorov led to the "Statistical theory of metallic crystallisation"[7]

for overall transformation kinetics. Two years later Johnson and Mehl, and subsequently Avrami, independently arrived at the same concepts.

In 1939, Johnson and Mehl presented to the A.I.M.E. their work on overall transformations [8] applicable to reactions like freezing from liquid and solid-state reactions like recrystallisation or phase transitions.

Previous authors had suggested different curves defining the kinetics of transformation in isothermal conditions, in nucleation and growth defined processes, and applied them to the decomposition of austenite into ferrite and pearlite, for instance. Most of those isothermal reaction curves are valid only when the untransformed phase suffers no changes in composition. If these changes occur, the nucleation and/or the growth rate will be affected and hence, so will the kinetics of the process.

Johnson and Mehl's original work was applied to the case of random nucleation. Their basic assumptions were that the reaction evolves by random nucleation and growth and that the nucleation ($\dot{N}$) and isotropic growth (G) rates stay constant throughout the process. The reacted or transformed volume fraction predicted according to these assumptions is then,

$$V\{t\} = 1 - \exp\left(-\frac{\pi}{3}\,\dot{N}\,G^3\,t^4\right) \tag{2.15}$$

where $V\{t\}$ is the volume transformed and t is time.

For the case of the kinetics of reactions occurring at grain boundaries, like the decomposition of austenite, the assumptions considered were [8]:

1. The reaction evolves by nucleation and growth with constant rates.
2. Nucleation happens only at grain boundaries.
3. The grains are assumed to be of spherical shape.
4. The new grains grow into the grain where they originated without crossing any boundary to another grain.

5. The rate of growth is retarded towards the end of the reaction due to impingement into other grains.

The kinetic curves resulting in this case show a similar shape to the ones represented by Equation 2.15.

The theory presented by Johnson and Mehl received mixed replies of encouragement and criticism. Especially critical was Melvin Avrami who, at that time was about to publish the first of a series of three articles on the subject.

In Avrami's approach to the transformation reaction kinetics [9, 10, 11], he considered that all the parameters controlling the reaction (*e.g.* pressure), were fixed except for temperature and time. He assumed the presence in the original matrix of nuclei that could be either heterogenities or minute crystals of the new phase.

Contrary to Johnson and Mehl assumptions, he affirmed, based on experimental data from the literature, that the assumption of constant rate of nucleation is in many cases contrary to the experimental facts. He was more of the idea that a certain number of nuclei already exist in the old phase as a function of, *e.g.* degree of undercooling, that at some point during the process become activated leading to the growth of new grains. Moreover, as more of them become new grains, the number of nuclei available for activation becomes scarce. $\tilde{N}$ is defined as the number of nuclei, a function of temperature of overheating and time, which decreases with an increase in either quantity.

The range of temperatures or composition in which the ratio between the probability of activation of a given nucleus and its growth rate is constant, is defined as the *isokinetic range*. In this range of temperatures or compositions, a time scale transformation can be used to be able to analyse the transformation phenomena as if they had constant kinetic characteristics.

Under these circumstances, the transformed volume fraction becomes,

$$v\{t\} = 1 - \exp\left(-g\{t\}\right) \tag{2.16}$$

where $g\{x\}$ is a function of the cube of the growth rate, the number of nuclei, a constant and some power of time. At the beginning of a 3-dimensional transformation with random nucleation and a constant growth rate, this exponent is 4, while if growth begins from a specified set of sites, without a need for nucleation, the exponent becomes 3. If all the other parameters are included in a parameter b, the well known expression is reached:

$$v\{t\} = 1 - \exp\left(-b\,t^n\right) \tag{2.17}$$

where the factor n varies depending on the specific situation in which this expression is applied. In three-dimensional growth it can take the values 3 or 4 as previously stated, in plate-like growth it is reduced to 2 or 3 and 1 or 2 in linear growth [10].

In his articles, he explicitly developed the concept of *extended* volume as opposed to *real* volume, to deal with the impingement of growing grains, although this concept is also present in the work by Johnson and Mehl and Kolmogorov. The extended volume includes also the volume of transformed phase that in its growth has already overlapped other growing grains. During the reaction of transformation to a phase β, the ratio between the extended volume v_β^e, to real transformed volume v_β is assessed considering the volume that has to be transformed yet $1 - v_\beta$, related to the total volume of material V.

$$dv_\beta = (1 - v_\beta)\; dv_\beta^e \tag{2.18}$$

In the third instalment of the series [11], Avrami further simplified the method by introducing the concept of *locally random nucleation*, implying that that was the only condition needed to apply the method of the extended volume because a locally random nucleation already produces a locally random distribution of growing nuclei, allowing us to use the general expression of the theory in cases as grain boundary nucleation.

The "Avrami" theory for overall transformation kinetics was extended by Cahn who modelled heterogeneous nucleation at the parent phase's grain boundaries. It was able therefore to deal with nucleation site saturation (*i.e.* when all the grain boundary nucleation sites are exhausted).

More recently, Robson and Bhadeshia have adapted the theory to deal with more than one reaction occurring at the same time [12, 13]. The same development has been used by Jones and Bhadeshia in the study of the simultaneous decomposition of austenite into several transformation products [14] (allotriomorphic ferrite, Widmanstätten ferrite and pearlite), and the competitive formation of inter and intra granularly nucleated ferrite [15], as a function of composition of the steel, austenite grain size and heat treatment.

2.2.3 Martensitic transformations

Most martensitic transformations are athermal, *i.e.* the fraction of transformation depends more on the undercooling below the transformation-start temperature (M_s) than on the time.

In 1958, Koistinen and Marburger [16] deduced the relationship between the extent of transformation and the undercooling by fitting to experimental data. The form of the equation was later justified by Magee [17]:

$$1 - V_{\alpha\prime} = \exp\left[-1.1\,10^{-2} \times (M_s - T_q)\right] \tag{2.19}$$

where $V_{\alpha\prime}$ is the volume fraction of martensite and T_q the temperature below M_s.

2.2.4 Transformation diagrams and critical cooling rates

Time-temperature-transformation (TTT), also known as isothermal transformation (IT), diagrams are determined experimentally to describe the evolution of transformation during isothermal heat treatments at different temperatures. As the construction of the equivalent diagram for transformations happening during continuous cooling (CCT) is a more complex matter, several techniques have been developed to allow the determination of the second from the first or to be able to determine directly the resulting microstructure relying on the information that a TTT provides.

A method to predict the result of heat treatments composed of several isothermal

stages at different temperatures using isothermal transformation diagrams was published by Scheil [18] in 1935. The amount of transformation was related to the partial time to obtain some degree of transformation at each of the different temperature steps. At the end, if the reaction can be considered additive (the instantaneous transformation rate is only function of the amount of transformation and the temperature) the time t needed to reach the amount of transformation v_a can be calculated as,

$$\int_0^t \frac{dt}{t_a\{T\}} = 1 \tag{2.20}$$

where $t_a(T)$ is the time needed, at temperature T to reach the fraction of transformation v_a on a isothermal diagram.

Later, in 1940, Grange and Kieffer studied the relationship between isothermal and continuous cooling decomposition of austenite [19]. These authors developed an empirical method for calculating CCT diagrams only based on the TTT diagrams.

The austenite transformation in a certain alloy was studied and the CCT diagram constructed. The authors observed that as the cooling rate becomes higher, the transformation temperature becomes lower. The relationship between the IT and CCT diagrams was studied and a method to predict the latter from the former was suggested. Their method is empirical and based on representing any stage of the cooling by a point on the isothermal diagram which indicates the equivalent amount of transformation that has occurred on cooling to that temperature at the specified rate. In order to avoid *"complex and tedious calculations"* the authors made two assumptions:

1. The extent of the transformation of the austenite at the instant it cools to the intersection point with the IT curve is not substantially greater than it would have been if quenched instantly to that temperature.

2. On cooling through a limited temperature range (T_1 to T_2 ; $T_2 < T_1$), the amount of transformation is substantially equal to the amount indicated by the TTT diagram

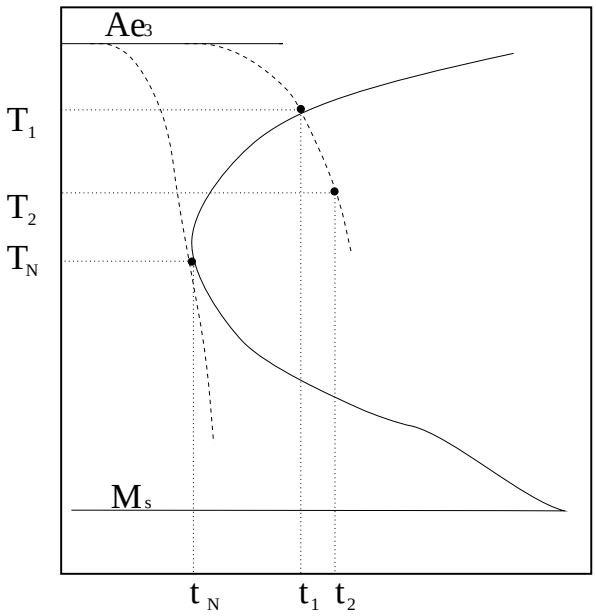

Figure 2.1: Diagram illustrating the method devised by Grange and Kieffer on how to determine continuous cooling transformation diagrams from isothermal transformation ones.

if the isothermal transformation was considered at temperature $\frac{T_1+T_2}{2}$ during a time interval $t_2 - t_1$.

After these considerations, and following their method, the calculated CCT diagrams showed good agreement with those determined experimentally.

Another empirical tool is to use mathematical expressions based on the study of many CCT diagrams [20] to determine the critical constant cooling rate needed to have a certain amount of transformation of such a phase (*i.e.*100% martensite) [21, 22]. Usually these expressions take into account the composition of the steel, and the effects of each alloying element. Often an intermediate step to determine the effect of alloying elements is to determine a "carbon equivalent" of the multi-element composition. The results obtained from this method are only reliable when dealing with a very narrow range of alloys similar to the ones from which the critical cooling rate expressions were determined.

However, this method can still be successfully applied nowadays in some cases, like

microstructure modelling. Ion *et al.* [23] have used a carbon equivalent based expression for critical temperatures of transformation, including the effect of grain size, to model the microstructure and hardness of heat-affected zones in welds.

A more recent approach towards the determination of CCT diagrams for various compositions is the one used by Wang *et al.* who trained an artificial neural network (see section 5.1) to model the generation of continuous cooling transformation diagrams. In their article [24] they interrogated that model about the effect of the carbon content and cooling rate in the continuous cooling reactions. This is a new (although still empirical) approach to complex problems like non-isothermal reactions and kinetics.

Bhadeshia [25] produced a thermodynamic method for the prediction of isothermal transformation diagrams for steels. The diagrams are basically defined as two curves, one describing the start of the diffusional transformations (pearlite, allotriomorphic ferrite) and another the displacive ones (Widmanstätten ferrite, bainite), together with start-temperatures for each of the phase changes. These curves are determined using classic nucleation theory [6] and Russell's method to determine the incubation period τ_s for each phase [26]. According to this method, τ_s is proportional to

$$\frac{T}{(\Delta F_m^V)^p D} \tag{2.21}$$

where ΔF_m^V is the maximum volume free energy change accompanying the formation of a nucleus, determined following Hillert [27] and Aaronson *et al.* [28, 29], p is an exponent that is function of the nature of the nucleus, being $p = 2$ for coherent nucleus and $p = 3$ for incoherent one [26], and D is an effective diffusion coefficient related to boundary or volume diffusion, depending on the coherency state of the nature of the phase considered, and according to theory of diffusion coefficients is proportional to [6]:

$$\exp\left(\frac{S_D}{R}\right)\exp\left(-\frac{Q_D}{RT}\right) \tag{2.22}$$

where S_D is the activation entropy for diffusion and Q_D the activation enthalpy for diffusion.

2.3 Process models

Studies dealing with processes like quenching and induction hardening are aimed primarily at the prediction of residual stresses. This requires the calculation of the microstructural evolution, but in most cases this has not been the main focus of the studies.

Most researchers model reconstructive phase transformations during induction hardening and quenching using a general form of the Johnson-Mehl-Avrami equation (equation 2.17) [30, 31, 32, 33, 34, 35]. The parameters b and n are fitted to experimental data using various methods, *i.e.* determined from isothermal experiments [31, 36, 32, 33, 34, 37]. Some authors use a set of averaged parameters for all of the temperature range considered, but the rest of models take account of the temperature dependence of b and n [32, 33, 37].

Pokrovskii and Leshkovtsev use TTT diagrams to determine the start and end of the pearlite and bainite transformations, and fit the Johnson-Mehl-Avrami equation to the former, and apply an additional fitting parameter to calculate the extent of the bainite reaction [30]. The transformation from isothermal transformation to anisothermal is carried out [32, 33, 34, 37] by assuming that the additivity principle [6] holds and applying Scheil's rule [18].

Transformation to martensite is in most cases [28, 32, 33, 34, 35, 38] determined using the equation published by Koistinen and Marburger [16] (equation 2.19).

Some other authors have used extremely simplistic methods. Xu and others [39, 36] only consider the transformation to martensite during quenching, and ignore the distribution of the rest of the possible phases of decomposition of austenite [39, 36]. Jahanian [40] presents a model with a very elaborate calculation of the transient thermal cycle, and the stresses and strains created during phase transformations, but the phase transformation model itself is reduced to consider that the volume of material that cools faster that some critical rate, transforms to martensite, and the rest transforms to pearlite.

Pokrovskii and Leshkovtsev [30] modelled quenching using polynomial equations fitted to experimental data to describe the hardness H^T of two steels after complete transfor-

mation during isothermal hold at temperature T. The cooling curves for the process are discretised in many isothermal steps T_i, and the volume fraction Δv^{T_i} of austenite transformed to a particular product phase at each step determined. The final hardness of the alloy is determined as the sum of the hardness of the fraction of phase transformed at each temperature, averaged by the volume fraction transformed.

$$H = \sum_{T_i} H^{T_i} \Delta v^{T_i} \tag{2.23}$$

Finally, Fuhrmann *et al.* [41] present a model on induction hardening, in which phase transformation modelling is based on the work by Leblond, Devaux and others [38, 42]. These authors discard the use of methods based on the Johnson-Mehl-Avrami equation and the use of the Scheil's method in front of a rate law of the form:

$$\dot{v}^{\beta} = \frac{v^{\beta}_{eq}\{T\} - v^{\beta}}{\tau\{T\}} \tag{2.24}$$

where $\dot{v}^{\beta}$ is the transformation rate to phase β, v^{β} is the volume fraction of β and $v^{\beta}_{eq}\{T\}$ is the equilibrium volume fraction of β at temperature T. $\tau\{T\}$ is a time constant, conveniently determined so that the method fits the experimental results.

In summary, most research on modelling of induction hardening and quenching has focused on the determination of residual stresses, often incorporating empirical or very simplistic microstructure models.

2.4 Phases considered

What follows is a brief description of the most significant product phases due to the decomposition of austenite.

2.4.0.1 Ferrite

The first phase to form during the cooling of austenite is allotriomorphic ferrite. Allotriomorphic ferrite forms at 910°C in pure iron but can start to form as low as 723°C in a steel containing a 0.77 wt% carbon. Ferrite nucleates at the austenite grain boundaries, and grows by a reconstructive process that involves the rearrangement of all atoms. In the case of complex alloys, containing alloying elements other than carbon, the diffusivity of some of the substitutional elements diffuse at a rate which is several orders of magnitude smaller than that of carbon, which is an interstitial alloying element.

Idiomorphic ferrite forms by the same mechanism as allotriomorphic ferrite with the only difference that it nucleates at inclusions and particles within the austenite grain.

Widmanstätten ferrite presents a plate-like structure. It nucleates at austenite grain boundaries and at previously formed allotriomorphs of ferrite. Widmanstätten ferrite is formed below the temperature where allotriomorphic ferrite forms but still above the temperature where bainite starts to appear. The mechanism of transformation is displacive, and although substitutional atoms do not partition, there is not enough driving force to avoid the partitioning of carbon, the flux of which becomes the limiting factor for growth.

2.4.0.2 Pearlite

Pearlite is probably the most widely known microstructure of steel. Discovered at the end of the 19^{th} century by Sorby, and named after its *pearl-like* appearance under the microscope, this phase is a substantial constituent of many commercial steels, because of its versatile mechanical properties.

Pearlite is a lamellar composite of interpenetrating ferrite and cementite crystals that grow in a cooperative way, side by side, by a diffusive process, usually from the austenite grain boundaries. It can also develop from inclusions or austenite-ferrite interfaces. Pearlite is nucleated by ferrite in hypoeutectoid steels and by cementite in hypereutectoid ones. The growth rate of the new pearlite bicrystal is mainly determined by diffusion of carbon ahead of the pearlite austenite interface. For this reason, the transformation

temperature will define the diffusion rate of carbon, the plausible diffusion distances and in turn, the final interlamellar spacing. The lamellar spacing in pearlite is a function of the transformation temperature and cooling rate. The spacing of the lamellae is the main parameter that defines the mechanical properties of pearlite in a given alloy.

2.4.0.3 Bainite

Bainite forms by a displacive mechanism, nucleating at the austenite boundaries. Bainite consists in thin plates (sub-units) of bainitic ferrite, that cluster in sheaves. Nucleation starts at the austenite grain boundaries, and the transformation is, initially, diffusionless, but immediately after transformation carbon diffuses to the remaining austenite, and a new set of bainite sub-units can then form nucleating at the tip of the just-formed ones. As austenite keeps being enriched with carbon, the driving force becomes smaller with subsequent transformation until this process eventually stops. Substitutional elements do not diffuse.

In upper bainite, some of the carbon that has been expelled from bainitic ferrite and that enriches austenite precipitates in the form of intersheave cementite. This is still possible because upper bainite grows at temperatures in which the diffusion of carbon is still faster that precipitation of carbides. At lower temperatures, the mobility of carbon is reduced, and some of it cannot leave the supersaturated ferrite, so it precipitates in the form of fine carbides inside the ferrite plates. The rest of the carbon that has been able to diffuse to the austenite still precipitates as inter-plate carbides. This gives the characteristic morphology of lower bainite.

2.4.0.4 Martensite

The formation of martensite is usually an athermal process. Martensite nucleates and grows without diffusion, only with small, well defined shifts of planes of atoms. The speed of transformation is enormous, of the order of the speed of sound in the metal. The extent of transformation only depends on the undercooling below the martensite-start (M_s) temperature. Martensite forms in the shape of thin plates or lathes. The lathes have

well defined habit plane and they appear in several variants of this plane on each grain. The maximum value of hardness that martensite can achieve in steel is approximately 800 HV [43].

Chapter 3

Austenitisation and deformation

3.1 Austenitisation

3.1.1 Phenomenology

The stable crystalline phase in pure iron above 910°C (and up to 1390°C) is austenite. Austenite has a face-centred cubic crystal structure (FCC). Formation of austenite occurs by nucleation and growth [44]. The transformation from ferrite to austenite in pure iron occurs at faster rates than in carbon steels where carbon is occupying some of the interstices between iron atoms in steel, or forming various ferrous carbides. In alloy steels the limiting factors for transformation are the diffusion of solutes, making austenite growth more sluggish [45].

The graphical depiction of an isothermal transformation diagram to austenite presents the shape of the lower half of a "C", as shown in Figure 3.1. This shape is a consequence of the fact that both the driving force for transformation and diffusion rate increase with temperature.

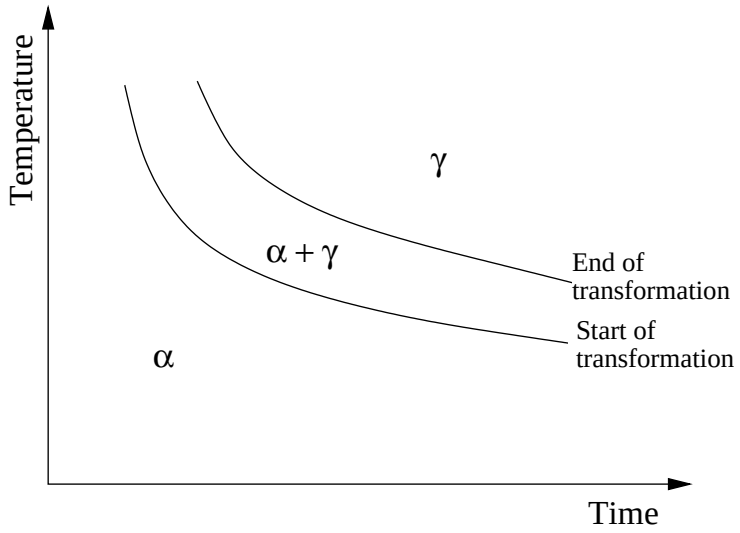

Figure 3.1: Schematic isothermal austenite transformation diagram. α represents ferrite and γ austenite.

3.1.2 Nucleation and growth

The transformation to austenite follows a nucleation and growth mechanism [44], both of which depend on the initial microstructure.

Considering that austenite forms by the eutectoid reaction,

$$\text{ferrite} + \text{cementite} \rightarrow \text{austenite}$$

already implies that the reaction will have to nucleate at the interface surfaces between ferrite and cementite. As the progress of the reaction depends on the diffusion of carbon released from the decomposition of cementite, the coarseness of the microstructure will correspond to a decrease in reaction rate. The reaction proceeds faster the finer the microstructure [44].

In pearlite, the ratio of ferrite/carbide surface area can be high, typically $4 \times 10^5 \text{m}^{-1}$ for pearlite with a interlamellar spacing of 5×10^{-6}m. However, austenite nucleates preferentially at the interfaces between pearlite colonies. This is because the interfacial energy at the colony boundary is presumably larger [45].

The formation of austenite from ferrite/cementite aggregates has also been studied. In ferrite, nucleation occurs primarily at the ferrite/ferrite boundaries, whereas in pearlite it is at ferrite/cementite interfaces on the edges of a pearlite colony [46, 47, 48]. With mixtures of ferrite and spheroidised carbides austenite tends to nucleate at ferrite/carbide interfaces adjacent to ferrite/ferrite grain boundaries [46]. For the mentioned microstructures, the preferred sites are evidently the high angle boundaries whatever the initial microstructure. Moreover, even in untempered martensitic microstructures the most favourable nucleation sites are the prior austenite grain boundaries, and in the case of tempered martensite a fine dispersion of carbides could homogenise the distribution of nucleation sites [49, 48, 50]. In structures containing retained austenite, this phase simply grows transforming other phases [51, 52, 53, 54].

Reed *et al.* present a technique to simulate laser-pulse heat treatments and the relevant austenitisation transformation of ferrite/cementite mixtures [55]. They confirm that

nucleation of austenite starts preferentially at the ferrite cementite interfaces and that the nucleation process is exceedingly rapid ($\approx$ 0.1 s at 1000°C) [55].

The effect of cold deformation prior to austenitisation accelerates the rate of transformation when the initial microstructure is a mixture of ferrite and spheroidised carbides [56]. The deformed microstructure may at slow heating rates recrystallise prior to the formation of austenite [56].

3.1.3 Alloying elements

The effect of alloying elements can be complex in two respects. Firstly, they may not be homogeneously distributed in industrial materials. More fundamentally, some solutes may not partition during transformation even if thermodynamics favours a redistribution between phases.

Chemical segregation is frequent in cast alloys when the solidification occurs under non-equilibrium conditions. This segregation can be reduced during subsequent deformation and heat treatment but it is never eliminated entirely. During rolling, the segregated regions become elongated and oriented in the direction of the deformation, resulting in macroscopic bands of chemical segregation, which then leads to microstructural banding. Microstructural banding can have detrimental effects on mechanical properties and transformation behaviour of steel [57, 58].

When banded steels are heated, austenite nucleates first in the regions where the temperature is above the *local* transformation temperature (*i.e.* those bands containing higher manganese and/or low phosphorus and silicon), resulting in austenite grains that grow along these bands [44].

Banding extends the overall isothermal reaction over a longer time interval, displacing the beginning of transformation to shorter times and extending the time needed to complete austenitisation [44].

3.1.4 Modelling austenitisation from different microstructures

Modelling austenitisation from any possible initial microstructure at once is not possible unless it is dealt with in a very abstract way. Classic kinetic theory allows the use of nucleation and growth rates that are a function of the initial distribution and morphologies of phases [6].

Roósz *et al.* argued that the rate of nucleation is inversely proportional to the product of the average pearlite colony edge length and the square of the average true interlamellar spacing, and that nucleation sites are not used up during the transformation process [47]. Grain growth rate was considered to be inversely proportional to the square of the average true interlamellar spacing [47]. Caballero *et al.* used a model based on classic nucleation and growth theory to study the influence of the microstructure on the kinetics of transformation from pearlite to austenite [59]. Classical kinetic theory has also been used by Yang and Bhadeshia to model austenitisation of bainite and retained austenite mixtures [54].

Oddy *et al.* present a complete microstructure prediction model based on nucleation and growth, and the effect of carbon diffusion [60]. The integration of Fick's equation of diffusion has also been another approach to model austenitisation. These models consider that the diffusion of some element (usually carbon, but some models consider other elements as well) is the limiting parameter to growth of austenite.

Akbay, Atkinson and others have presented a series of models on the austenitisation of steel. In the first of these, the austenitisation of mixtures of ferrite and pearlite considering diffusion of carbon in austenite only and local equilibrium conditions was considered [61]. In this case the exact solutions of the diffusion equation were calculated and the results compared with numerical calculations.

In an article published in 1995 [62], Atkinson *et al.* studied the process of reaustenitisation from ferrite/cementite mixtures. Their model was based on a series of assumptions, like assuming local equilibrium and ignoring the diffusion of carbon in ferrite and cementite. These phases are assumed to be semi-infinite in extent, so that soft impingement effects could be ignored. The model combined the thermodynamic calculation of equi-

librium conditions coupled with kinetic phenomena. Solutions for the decomposition of cementite and reaustenitisation from ferrite/cementite aggregates were presented and the effects of some substitutional elements discussed.

Further insight into the subject was cast in the following article where diffusion of carbon in cementite and ferrite was also considered alongside with diffusion in austenite [63, 64]. In this case a planar interface was considered. Finally, when the diffusivity of carbon in austenite is considered to be concentration dependent the process of reaustenitisation is found to be controlled by the diffusion of carbon in austenite [65].

As these models become more complex, analytical solutions are no longer available, and diverse numerical methods are used. In order to study the morphology of the growing phase, some authors have implemented their models using finite element methods.

Jacot *et al.* [66] used a regular hexagonal grid and elements that could either represent one of the phases involved or part of the interface. The movement of the interfaces was calculated from solute flux and equilibrium condition considerations. The microstructure was incorporated by digitising actual micrographs, but still adjustments were needed to achieve accuracy.

Another model by Jacot *et al.* [67] implemented on finite element grid considering solute diffusion and capillarity effects applied to the reaustenitisation of pearlite. The shape of the interface was correctly predicted, when compared with micrographs, but only for small values of overheating ($\Delta T < 3$ °C). In the case of greater values the system became unstable, and the shape of the interface tended towards a rapid transformation of ferrite and then lateral dissolution of cementite plates.

Finally, the already mentioned model [66] was completed by Jacot *et al.* and a comprehensive model for austenitisation, homogenisation and grain growth from a ferrite pearlite microstructure [68]. A similar model has been presented by Mancini *et al.* to predict the transformation to austenite from ferrite/pearlite microstructures [69].

The phenomenology of transformation to austenite from other initial microstructures has been studied and sometimes modelled by several authors. Law *et al.* produced in 1980

a model considering the transformation of ferrite, bainite and martensite to austenite in low carbon steels [48].

An aspect that adds more complexity to the study of the transformation to austenite is the initial microstructure. The possible combinations of different phases that could become an austenitic structure when heated are infinite. This is the reason why, even though many researchers have dealt with that issue, their models are always limited to specific reactions. Gavard *et al.*, on the other hand, decided to avoid that problem by modelling the transformation to austenite using a neural network (see also Section 5.1 for an introduction to neural networks).

The trends shown by their model are consistent with well known metallurgical trends, and the accuracy of the model falls in a range of $\pm$ 40 K (95% confidence limits). The authors found that the predictability of A_{c1} was lower than that of A_{c3} in many cases. This was assumed to be consequence of the accuracy of the input data, being that in many cases, A_{c1} temperature is more difficult to measure experimentally [53].

The authors found that A_{c1} temperature, clearly, and A_{c3}, showing large uncertainty, but still showed a maximum when plotted against heating rate. This phenomenon was explained as follows. Some of the starting microstructures contained retained austenite. At slow heating rates, the retained austenite has to decompose to ferrite and carbides prior to begin nucleating and growing new austenite when equilibrium permits. At high heating rates, the retained austenite begins to grow as soon as the equilibrium temperature A_{e1} is exceeded [53].

Bailer-Jones *et al.* used a Gaussian process model instead to model the critical transformation temperatures to austenite [70]. A Gaussian process model has some advantages over neural networks in the sense that it does not parameterise the input-output function, and there is no need to take a decision *ad hoc* about the level of complexity of the structure of the model, but it is also more demanding in computer power. A Gaussian process model parameterises instead a probability function over the database (in Section 5.2 there is an introduction to Gaussian processes).

As a summary, although there is considerable literature concerning the austenitisation of diverse starting steel microstructures, only a few of the models reviewed do take into account the specific characteristics of hypoeutectoid steels. Sometimes the starting microstructure is simply ignored, and in other occasions it is taken into account only by using nucleation and growth based models that include some microstructural parameter, like interlamellar spacing, in an abstract way. Only some models implemented using finite element methods describe the process of austenitisation of a ferrite/pearlite microstructure, but these are, in most cases, of limited applicability. Models which attempt to be physically rigorous, such as that of Akbay *et al.*, are grossly simplified, for example to deal with growth alone, and are not in general applicable.

3.2 Effects of deformation

3.2.1 Effect of deformation on kinetics

3.2.1.1 Decomposition of austenite

Deformation tends to accelerate phase transformations. The main effect observed is an increased nucleation rate [71, 72, 73]. The effect on the growth rate is less understood, with contradictory conclusions [71, 72, 73].

An increase in nucleation is expected because the number density of heterogeneous nucleation sites is increased by deformation. A deformed austenite grain structure has a larger surface to volume ratio [71, 74]. The grain boundaries become serrated so that their efficacy as nucleation sites is increased. Further nucleation sites are introduced at intragranular deformation bands [71, 74].

Deformation, on the other hand, has been proven to be able to stabilise austenite against transformation to bainite [74, 75]. Plastic deformation of austenite does increase the nucleation rate of bainite, but each new nucleus transforms to a smaller amount of bainite, and nuclei then become exhausted as the reaction progresses, yielding a smaller transformed volume fraction. The carbon-enriched austenite remaining can then form mechanically stabilised martensite. Small compressive stresses have been proven to accelerate the kinetics of bainite formation [76].

3.2.1.2 Austenitisation of deformed ferrite/pearlite aggregates

In the first instance, deformation has been found to increase the kinetics of recrystallisation of ferrite during austenitisation [77].

Deformation reduces the incubation period for isothermal austenite formation and increases the rate of transformation [77]. Interestingly, the volume fraction of austenite at first can exceed the equilibrium fraction. Then, given enough time, the excess austenite transforms to ferrite towards the equilibrium volume fraction. This occurs because of the

initial formation of low carbon austenite, that later retransforms to secondary ferrite. The discrepancy between the initial and final fractions of austenite increases with the degree of deformation [77].

3.2.1.3 Austenitisation of deformed martensite

Undeformed martensite has been found to resist recrystallisation during austenitisation. On the other hand, deformed martensite recrystallises prior to austenite formation [78].

With undeformed martensite, austenite nucleates at the prior austenite grain boundaries. Lightly deformed martensite may recrystallise into a mixture of fine ferrite and carbides, and austenite subsequently nucleated at the ferrite grain boundaries. Heavily deformed martensite can recrystallise simultaneously with reaustenitisation. In the latter case austenite nucleates at both ferrite and prior austenite grain boundaries.

3.2.1.4 Effect of prior deformation of austenite on austenitisation

The effect of the deformation of austenite on the kinetics of later phase transformations, have been studied by Kaspar *et al.* [49]. When the transformation of deformed austenite occurs by a reconstructive transformation, subsequent austenitisation kinetics are not affected. In the case of austenite transforming by a displacive reaction, some of the defect structures are inherited by the transformation products, and in turn affect subsequent austenitisation, by acting as enhanced nucleation sites. On the other hand, if martensite is tempered, the distribution of finely precipitated carbides act as more powerful nucleation sites, and the nucleation of austenite happens homogeneously distributed in the bulk of the alloy.

3.2.2 Grain deformation

The topological evolution of crystalline grains during deformation processes has been studied by Toribio and Ovejero [79] and Singh and Bhadeshia [80, 74].

Two main changes occur in pearlite colonies during deformation. During the first stages of deformation the main axis of the colony tends to align towards the direction of drawing. Later in the process, this orientation is accompanied by slenderisation of the colonies in which the main axis (now oriented almost parallel to the drawing direction) becomes elongated and the perpendicular section of the colony shrinks [79].

3.2.3 Deformation of pearlitic steel: effects on ferrite and cementite

A few deformation methods lead to a homogeneous distribution of strains. Wire drawing and swaging produce fairly homogeneous deformation modes. Being processes of considerable technological importance, much of the information reviewed here therefore focuses on them.

Hypoeutectoid steels have a complex microstructure, containing varying proportions of ferrite and pearlite. Pearlite consists of a mixture of ferrite and cementite. Ferrite is almost pure iron, in a body centred cubic crystalline structure, which is able to sustain a substantial amount of plastic deformation. Cementite is relatively brittle, ceramic-like compound that in pearlite is arranged in laminae or sometimes spheroids. Cementite can only deform plastically if the right macroscopical conditions are met [81, 82]. The necessary condition for a crystal to be able to behave in a ductile manner is to have five independent slip systems. In the case of cementite, six possible slip systems have been found to explain its ductile behaviour [82].

Langford affirms that there is no evidence reported of ductile behaviour of cementite laminae thicker that 0.1 μm and in the same way there is no evidence of brittle fragmentation of cementite laminae thinner than 0.01 μm [83]. Besides, in most cases, the evidence for plasticity of cementite has been collected in processes involving wire drawing or swaging whereas most evidence of brittle behaviour in cementite has been obtained from tension or compression experiences [83]. Parameters like the actual level of deformation may also have an influence on these limits [83]. The fractures in cementite observed experimentally, may be caused by shear [82].

Pearlite shows two bulk deformation mechanisms. In homogeneous deformation the slip distances of all the active ferrite slip systems are similar, and the macroscopic deformation is also homogeneous. During inhomogeneous deformation, also referred to as *deck of cards* slip, there is a highly stressed slip system of ferrite that happens to be almost parallel to the plane of the lamellae [81].

Further thermo-mechanical treatment of pearlite produces progressive spheroidisation of cementite. A heat treatment at high temperatures can destroy the lamellar structure of pearlite, and previous cold work or simultaneous deformation can lower the temperature in which this phenomenon starts and accelerate it [84, 85, 86, 87]. Spheroidisation has been observed at temperatures as low as at 250°C in severely deformed steel ($\varepsilon \approx 7$) [88]. The process of spheroidisation occurs by the break-up of cementite plates into smaller platelets with an aspect ratio close to 8:1, which then tend towards spheres, before the onset of gross coarsening [84, 86]. The final size of the spheroid, prior to coarsening, is roughly proportional to the initial interlamelar spacing [86].

Spheroidisation is diffusion controlled [86]. Deformation accelerates this process by introducing defects. The activation energy has been estimated to be 220 to 270 $\mathrm{kJ\,mole^{-1}}$, which is almost identical to that for the self-diffusion of iron [86, 89].

Kinked lamellae tend to spheroidise slightly faster that straight ones because the kinks are defects where the process initiates. The mechanical fragmentation of cementite during deformation only accelerates the process marginally [86].

Most studies on spheroidisation of cementite are based upon a long time at temperature, with a minimum of one hour, but these processes are much faster that that. Weijuan *et al.* have observed spheroidisation *during* mechanical deformation at high temperature [87], and Fougeres *et al.* [90] found globulisation in cold worked specimens after very short heat treatments of a few seconds only. In the first instance cementite orients in the direction in which the wire is being drawn. A higher degree of deformation produces fracture and further orientation of the carbides, and still further deformation produces a finer and finer fibrous structure of ferrite and oriented carbides.

Following deformation, short heat treatments (in the order of 3.5 s) produced the following effects. At temperatures below 450°C and deformations in the range $\varepsilon = 1.24$ to $\varepsilon = 1.73$ few changes were observed in the microstructure, but beyond that temperature spheroidisation occurs. At 480°C fine spheroidisation of cementite can be already observed in samples deformed to $\varepsilon = 1.24$, and the spheroids of cementite have become clearly coarser at 550°C. These authors conclude that spheroidisation is more evident, given enough temperature, with increasing deformation [90].

Annealing of cold worked alloys also produce spheroidisation, and in some cases, with high deformation rates, even dissolution of cementite [91]. When levels of deformation in the order of $\varepsilon \approx 4$ and beyond, like in some wire drawing manufacturing processes, spheroidised cementite spontaneously starts to dissolve in ferrite [88, 92, 93, 94, 95, 96]. A spheroidised microstructure reappears after a post deformation annealing [92, 97].

The dissolution of cementite is explained by the fact that during severe deformation, a very important increase of free energy is accumulated in new surfaces, slip steps, and the fracturing of cementite particles until cementite becomes unstable and dissolves [92].

During heavy cold working, carbon is expelled from cementite particles and is dissolved into ferrite [91, 98, 88, 93, 97]. Some of the carbon atoms liberated are trapped in dislocations while the rest enter the usual interstitial sites [98]. The carbon trapped in dislocations has a severe influence in the kinetics of recovery and recrystallisation. This effect is due to the pinning of dislocations by carbon atoms, retarding the annihilation of dislocations before recrystallisation can start [98].

Other elements can also affect the kinetics of spheroidisation and dissolution of cementite. Silicon has been found to build up in ferrite close to the interface between ferrite and cementite, hindering the progress of spheroidisation [93].

Chapter 4

Tempering of carbon steel

4.1 Tempering of martensite

Martensite can have a body-centred tetragonal structure if it is favourable for the carbon atoms to arrange themselves into one of the three possible sets of interstitial sublattices in the body-centred cubic structure. The level of tetragonality of the unit cell (c/a) is determined by the carbon content of the alloy [99]. Untempered martensite can be strong but frequently lacks ductility and toughness. During tempering, several phenomena occur leading to an increase in ductility at the expense of hardness and strength [100, 101].

The process begins with the diffusion of carbon trapped in the octahedral interstices for the purposes of the precipitation of diverse carbides. Recovery and recrystallisation of ferrite also play an important role if the tempering temperatures are high enough. The phenomena involved can be classified into several overlapping stages [102], as shown in Fig. 4.1.

Tempering of martensites of low carbon content, up to 0.2 wt.%, at temperatures below 150°C promotes the segregation of carbon to dislocation structures. It is not until the carbon content is raised to above 0.2 wt.% that precipitation of carbides begins to happen [101]. The carbide that precipitates from martensite, between room temperature and 250°C, is ε carbide which has a close-packed hexagonal crystal structure. The first stages of ε carbide precipitation in high carbon steels leads to hardening during tempering between 50 and 100 °C [100, 101, 102]. As the carbon precipitates, there is a reduction in the tetragonality of martensite. The activation energy for this precipitation process falls approximatelly in the range 60 to 80 kJ mol^{-1}, which is close to the activation energy for the diffusion of carbon in martensite, although the precise value increases linearly with the carbon concentration [102].

Cementite also precipitates over the temperature range 100 – 350°C. At the low end of this temperature range, cementite is formed as a Widmanstätten distribution of plates. This newly formed cementite can nucleate at the interfaces between ε carbides and the matrix. At the same time, martensite loses its remaining tetragonality and becomes body-

centred cubic (with $c/a = 1.0$), and ε carbides dissolve to form more cementite. Other nucleation sites for cementite are the twin boundaries present in high carbon martensites, interlath boundaries and prior austenite grain boundaries.

Between 200 and 300°C any retained austenite begins to decompose. It has been suggested that this happens by transformation into bainitic ferrite and cementite [102].

Above 350°C cementite particles coarsen and start to spheroidise closer to 700°C. Meanwhile, there is a process of rearrangement of dislocations and structures of defects within what used to be the original martensite lath boundaries, that leads to partial recovery of the structure. These boundaries will still be stable up to about 600 or 700°C when ferrite starts to recrystallise. The final microstructure consists of an equiaxed ferrite matrix with spheroidised cementite precipitates situated mostly at the grain boundaries.

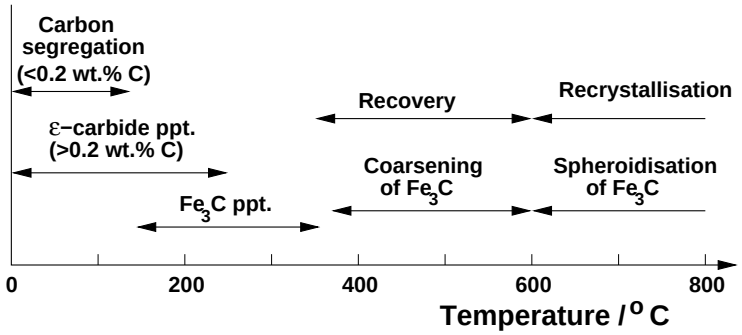

Figure 4.1: Approximate summary of the phenomena occurring during 1 hour of tempering of carbon steels. Diagram based on Fig. 12 of Speich [101].

4.2 Modelling of tempering and hardness prediction

Several parameters affect the final hardness of the steel, notably the chemical composition and microstructure. The composition can be defined precisely, whereas the microstructure is the result of a complex function of the composition and the manufacturing process. Various models exist to estimate the resulting hardness as a function of compo-

sition and/or thermomechanical history, as described below.

4.2.1 Hardness predictions used in process models

Most models dealing with the quenching and tempering of steels aim to predict the residual stresses generated during the thermal treatment, but pay little attention to phase transformations. Very few are designed to predict the final surface hardness or the hardness profile from the surface to the core of a component.

A common method of validating models is to determine the depth of the martensitic region by measuring hardness [32]. This is simple and effective validation but only acceptable as a first qualitative approximation because it does not provide direct information about microstructure changes.

Nagasaka *et al.* [34], using a finite element model for water spray-quenching, estimated an equivalent Jominy distance from the cooling time between 800 and 500 °C, and this value was compared with experimental Jominy curves. The calculation of the equivalent Jominy distance was done following the empirical functions presented by Wever and Rose [103].

4.2.2 Prediction of hardness evolution

There have been a number of studies dealing exclusively with hardness estimation as function of composition and thermal history. A very extended approach is the use of isotemper parameters, some function of time and temperature that permits determination of alternative combinations of time and temperature to yield the same decrease in hardness (equivalent temper).

4.2.2.1 Isotemper parameters

In the classic Hollomon-Jaffe method [104], a purely empirical tempering parameter is determined by fitting to the hardness evolution behaviour during tempering data for many steels:

$$H = f\{T\ (c + \log(t))\} \tag{4.1}$$

where t and T are the tempering time and temperature respectively and c is a fitting parameter related to the carbon content of the alloy considered.

The parameter has been used to integrate non-isothermal heat treatments. The method does not take into account the evolution of the microstructure or the composition of the steel, with the exception of the carbon content. Due to its simplicity of use and wide range of applicability, this tempering parameter has been in use for over 50 years in many industrial processes involving quenching and tempering of carbon steels.

Several similar methods based in the use of isotempering parameters have been presented by other authors, for example Maynier *et al.* and Grange *et al.* [105], who have presented very complete (but completely empirical) methods to predict some of the properties of low carbon steels after heat treatment. In Maynier's *et al.* method [105], a cooling rate is determined from a nomogram in the case of welded parts or from specific plots in other situations using as input the dimensions of the component. The composition of the steel is used to estimate critical cooling rates which define the formation of different phases in a CCT diagram. The cooling rate is then used to interpolate between the critical rates and find the approximate microstructure developed, using the rule of mixtures, and from the microstructure the hardness is determined. For the estimation of the hardness after tempering, a tempering parameter is presented and a new set of empirical equations to calculate the new hardness of each phase after tempering as a function of steel composition and tempering parameter was produced.

In another method, due to Grange *et al.* [106], the hardness is calculated as a function of composition and temperature for a tempering time of 1 hour. The effect of each element (carbon, manganese, phosphorus, silicon, nickel, chromium molybdenum and vanadium) at several temperatures is studied and related to the amount present in the alloy. The tempering conditions can then be adjusted to longer or shorter tempering times, or different temperatures by finding another set of conditions that result in the same value of

the tempering parameter. In this case, isotemper charts have been provided to avoid the explicit calculation of any intermediate parameter.

We have seen that most of the methods, although useful in design, are essentially empirical. Studies such as the one by Grange *et al.* [106] do nevertheless reveal the effects of composition in tempering.

4.2.2.2 Semiempirical modelling methods

Réti *et al.* [107], derived general relationships between isothermal and anisothermal transformation kinetics, and in one of their examples modelled hardness evolution. They introduced the concept of *property kinetics*, to link the kinetics of phase transition with the rate of change of some characteristic property, without having to account explicitly for the relationship between the microstructure and the property.

Thus, during isothermal heat treatment, the hardness is written, by analogy to Avrami kinetics, as:

$$H = H_{\alpha'} - b\left(\exp\left[-\frac{Q}{RT}\right]t\right)^n \tag{4.2}$$

where H is hardness after a heat treatment lasting a time t at a temperature T, $H_{\alpha'}$ is the as-quenched hardness of martensite, and b, Q and n are empirical constants, with R being the gas constant. The corresponding anisothermal form is written:

$$H = H_{\alpha'} - b\left(\int_0^t \exp\left[-\frac{Q}{RT}\right]dt\right)^n \tag{4.3}$$

Fitting to experimental data might then give clues about the mechanisms involved in the process, for example by identifying the activation energy Q.

Modelling the complete phenomena occurring during tempering is complicated. As shown in Fig. 4.1, there are simultaneous reactions which themselves are not well-characterised [108].

If only the first stages of tempering are considered, a model based on the precipitation of carbides from supersaturated martensite can be used. It has to be assumed

that recovery, recrystallisation, or coarsening do not occur. Speich [101] has shown that these assumptions are reasonable when tempering below 320°C which involves primarily a redistribution of carbon, and carbide precipitation.

Takahashi and Bhadeshia [108] used an Avrami type equation [6] to describe the precipitation of cementite precipitation as a function of time.

$$\xi\{t\} = 1 - \exp\left(-kt^n\right) \tag{4.4}$$

where $\xi\{t\}$ is the volume fraction of cementite, normalised by the equilibrium volume fraction of cementite at the reaction temperature. k and n are rate constants determined from experimental data. $\xi\{t\}$ was then assumed to be related to the hardness of martensite $H(t)$ at time t of the process by,

$$\xi\{t\} = \frac{H_{\alpha\prime} - H\{t\}}{H_{\alpha\prime} - H_F} \tag{4.5}$$

where $H_{\alpha\prime}$ is the maximum hardness of martensite and H_F is the hardness of fully tempered martensite before any degree of recovery or recrystallisation occurs. These relationships imply that the change in hardness during the first stages of tempering is directly related to the precipitation of carbon in the form of carbides. The parameter k can be expressed as being function of temperature as follows:

$$k = k_0 \exp\left(-\frac{Q}{RT}\right) \tag{4.6}$$

where Q is the activation energy for tempering. The parameters k_0 and n are finally determined from experimental data.

Chapter 5

Advanced empirical modelling methods

Recent improvements in the calculation power of computers have led to the possibility of implementing some tools that were only theoretical possibilities a few decades ago.

Artificial neural networks (ANN's) and Gaussian processes (GP's) are some of these new tools. In an interdisciplinary and complex subject like materials science, there are a lot of problems that may be well understood in qualitative ways but their solutions are difficult to estimate quantitatively. Some of these problems depend on a huge number of variables, making it difficult to build suitable physical models, without an unacceptable level of simplification.

In all these cases, and given enough data about the process or phenomena studied, an ANN or a GP represents a powerful tool of non-linear regression, able to create reliable empirical models on complex problems, whilst making no assumptions about the form of the relationships involved.

5.1 Artificial neural networks (ANN)

The very beginning of the artificial neural network field can be related to the work of McCulloc and Pitts in 1943 [109] on neurons as elementary logical units of adaptive systems. All neural network models are essentially designed to use the basic principle of information transfer found among biological neurons. In that sense, the input information is linked to the outputs in an adaptative manner, giving each of the input variables a different weight in the function [110]. Artificial neural networks cannot approach the complexity of the brain, which consists of a very large number of highly interconnected nodes ($\approx 10^{11}$ neurons with an average of $\approx 10^4$ connections each). There are nevertheless two main similarities between biological and artificial neural networks. The basic unit of the network is in both cases a relatively simple computational device (even though artificial ones are far simpler that biological ones), that is heavily interconnected. The function of the network if defined by the connections between its units or neurons. In practice, this is where the similarities with biological systems ends. It is interesting to

notice that due to its massively parallel structure, a biological neural network is much faster than any computer even though biological neurons are many orders of magnitude slower that electronic circuits [111].

There are many different structures and implementations of artificial neural networks, but most ANN's are based in one of the following three basic networks.

- Feedforward networks, for example, the *perceptron*. This type of neural network computes the output directly from the inputs in one single pass, without involving any degree of feedback. Feedforward networks are used for automatic control, adaptative filtering and other sorts of function approximation and they are also used in pattern recognition.
- Competitive networks work by determining some sort of distance between the stored prototype patterns and input pattern. Then they perform a competition to find which neuron describes best the prototype pattern closest to the input. Competitive networks *learn* by adding the new inputs to the prototype patterns. These adaptative networks learn to classify or cluster the inputs into different categories.
- Recurrent networks were originally inspired by statistical mechanics. They have been used as associative memories, in which the stored data are recalled by association with input data, rather that by a label or an address. They have been used in optimisation problems.

The most widely used kind of artificial neural network in materials science is the *multilayer feedforward net*. In a sense, this kind of ANN can be understood as a generalisation of the linear regression modelling method [112].

Whereas the linear regression equation lacks in flexibility (being linear or pseudo-linear, and once derived being applied across all the input space), the ANN has some extra advantages.

In an ANN analysis, each of the input variables (x_i) is multiplied by a random weight ($w_i^{(1)}$). All these products are then summed together and a constant $\theta^{(1)}$ is added. The

result of these operations is then used as the argument of, for instance, a hyperbolic tangent.

$$h = \tanh\left(\sum_i w_i^{(1)}\, x_i + \theta^{(1)}\right) \tag{5.1}$$

The output is then calculated as,

$$y = w^{(2)}\, h + \theta^{(2)} \tag{5.2}$$

where $w^{(2)}$ is another weight and $\theta^{(2)}$ another constant respectively. The hyperbolic tangent is usually chosen because of its flexibility.

Further degrees of flexibility and non-linearity are then reached usually by combining several hyperbolic tangents, or *hidden units* in the hidden layer.

Because the hidden units are not linear, these models can capture interactions between the inputs that a linear regression could not. In theory, the weight functions could be studied to find out the nature of these interactions but this is not straightforward.

The weights are systematically changed to develop many different models. Then these models are tested against a new set of data *unknown* to these models. The model or models that fit best to the studied data are chosen and the rest discarded. This optimum model can then be used to make predictions.

Sometimes, a committee of models is used instead of a single model. A committee is a group of the n best models from the training stage, used together, and averaging their results. Doing so, the reliability of the complete committee is usually improved over the areas of the input space where the density of information is scarce.

One of the risks while using ANN's is *overfitting* the model. If the final model or committee is too simple, it will not be able to illustrate the complexity of the real system. But if the data are noisy and the model becomes overcomplex and it could attempt to model the noise in the data. That would lead to extreme oscillations in areas of the input

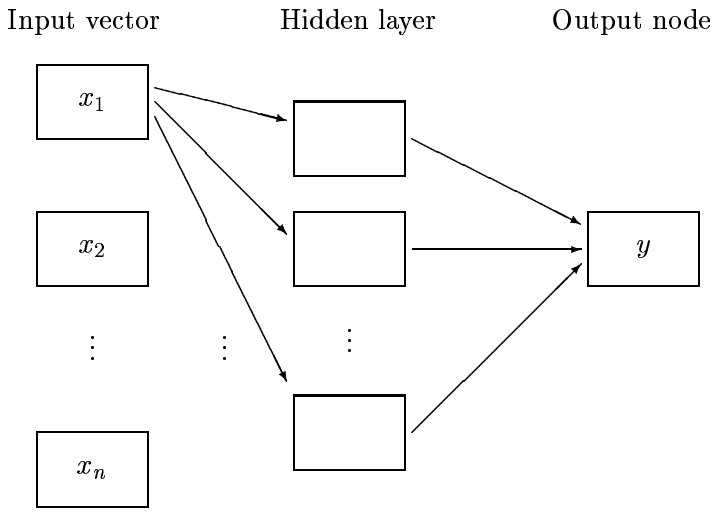

Figure 5.1: Structure of an Artificial Neural Network

space where the information is scarce and in the end to big errors in the predictions. This is also taken into account when selecting the number of hidden units in the models. Another approach to avoid that problem used by MacKay [113] is combining the predictive capability of a neural network with Bayesian statistics. Bayesian probability theory can be used to automatically infer the level of flexibility or complexity needed by the model based on the data, and so be able to avoid finding non-existent structures in the database, and falling into the trap of creating an overcomplex model. This method also allows the confidence level of each prediction to be estimated.

ANN's have been used successfully in many issues related to materials science, like transformation temperature predictions, mechanical properties predictions, monitoring and optimisation of processes. They can also be used to simulate experiments that could be impossible or very difficult to conduct in reality (*e.g.* the effect of varying only one of the governing parameters).

5.2 Gaussian Processes (GP)

As has been shown in Section 5.1, ANN's are a flexible way to approach the empirical modelling of complex phenomena. Another method to take into account is the Gaussian Process (GP) model.

When modelling complex problems in an empirical way, often the parameterised form of the input-output relationship is unknown. In these cases, instead of trying to use a predetermined parameterisation function, a parameterisation of the *probability* of the output over the data input variables can be used [70].

This is the approach used by a GP model. From the database an N-dimensional probability distribution of the output variables is inferred from the input variables. This joint probability distribution in the GP model is assumed to be a multivariate Gaussian.

A set of *hyperparameters* Θ is used to define the probability distribution. They have a similar role to the weights in an ANN.

Once the shape of the covariance functions is chosen, and with the hyperparameters Θ, dataset, targets, a new input, the output prediction and its standard deviation are then completely defined.

As opposed to the ANN's, the Gaussian Processes do not have to be tested against a set of new data, so all the dataset can be used to train it. The ANN's, on the other hand, are not trained in the whole dataset until the optimum structure of the model has been determined.

No decision has to be taken concerning the number hidden nodes and layers or of models in committee used to build the model. The Gaussian Process is trained once and it can be used straight away to make predictions [114].

5.3 Comparison between ANN and GP

These two techniques described in the previous sections (Sections 5.1 and 5.2), seem to give in most situations similar results and accuracy [114]. However, they have some important differences.

The most obvious one is the need when training an ANN to keep some part of the dataset to be used as a testing dataset, once the whole collection of models has been trained. The results of this test operation are then used to decide the optimum number of hidden units and layers in the models, and the number of models in committee. It is not until the optimum structure of the model has been determined that the model is trained with the complete dataset.

On the other hand, a Gaussian Process can be trained on the complete dataset from the start, because only one model is created. That means that all the information contained in the database is transferred to the model.

Another aspect to be taken into account is their respective ability to make accurate predictions beyond the limits of the database. Unless the trained function is well-founded, using this kind of model to make predictions outside those boundaries could mean that the predicted values come with big uncertainty estimators, showing the limited reliability of these predictions.

These predictions can still be made, and each type of model shows a characteristic behaviour. ANN's tend to follow the last trend suggested in the dataset. That means that they, within limits, can still be used to make some predictions not far from the dataset boundaries. GP extrapolative predictions, by contrast, tend to *relax* to a preset value, usually zero, defined prior to the setting of the model.

The labour and computing time required to set one of these models is also an important aspect to bear in mind when choosing one or the other.

To set an ANN requires the developer to train and test many models before the final model or committee of models is chosen and built. In this case, even though the computing

time is far from negligible, the human labour time is far greater. This can be changed by automation of some parts of the process [115], but it will still be a very time consuming operation.

By comparison, the training of a GP is relatively simple, having only to train a single model. The optimisation computer time however, grows as a function of the cube of the database, so that it can be rather short for small datasets but increasingly long for bigger ones.

Prediction times are very short for trained ANN's, because once the model is defined, the dataset does not have to be accessed again to make predictions.

This is different in the case of GP's, since the dataset is used every time that predictions are made. That means that for big databases the prediction times can become prohibitive.

This aspect of ANN's give them another advantage in some situations. When the database is confidential, the ANN model can still be used publicly, because the original database is not used or shown whereas in the case of the GP's, the database needs to be accessed to make predictions. This issue could still be dealt with by encrypting the database, but that would increase the processor load even further.

Last but not least, both kinds of models can be interrogated to find relationships and interactions between the input variables and the output by just studying the weights in ANN's or the hyperparameters in GP's. In the latter case this process is more intuitive than in the former. In fact, if the process is well known, some of the hyperparameters in the GP can be set beforehand.

In summary, ANN's and GP's are two powerful tools to set empirical models to describe complex problems. Both seem to give similar accuracy and trends in their predictions [114]. The work time required to set an ANN is longer than that for a GP, because of the many intermediate operations, but its prediction time is independent of the size of the database. The training of a GP depends on the cube of the dataset and its use to make predictions on the square of that size.

In fact, Tancret *et al.* have published an article [114] comparing the methods. The con-

clusion was that both methods produced similarly accurate results and were equally able to grasp the complexity of the phenomena studied and reproduce the right metallurgical trends.

5.4 ANN applied to materials science

The application of ANN's to materials science has been very extensive and successful [112]. Some examples have already been presented in other sections, but ANN's have also been used for mechanical properties of welds; prediction of cracking; mechanical properties of superalloys, including creep behaviour and determination of microstructural parameters; fatigue life determination and crack growth; phase transformation kinetics and critical transformation temperatures.

Chapter 6

Thermal cycle during induction hardening

6.1 Introduction

A full understanding of phase transformations during induction hardening of a medium carbon steel component requires an accurate knowledge of the heating and cooling thermal cycles. Even though steel is a good conductor of heat, the thermal profiles and the heating and cooling rates cannot be assumed as uniform through the thickness. Uniform conditions might be assumed for thin sections and for slow heating or cooling where the Biot number, $Bi \leq 0.1$, but this does not apply for the process and component considered here. The Biot number is defined as $Bi = hL/k$ where k is the thermal conductivity, L is a characteristic dimension, and h is the heat transfer coefficient, and represents the relative resistance to heat flow within a body with respect to the resistance of the cooling media [116].

A model to predict the evolution of temperature is described here, beginning with the heat transfer equations which are integrated analytically. However, a second, more flexible model, based on a numerical integration of the heat transfer equation is also introduced. Both models have been implemented using FORTRAN.

6.2 Analytical model for temperature evolution

Consider a plate of thickness $2L$ and side dimensions long enough to be designated infinite. For a heat conducting material like steel, considering this geometry is usually acceptably accurate even for other examples such as hollow cylinders, where the thickness is small compared to the diameter. The symmetry of the system permits the use of single space coordinate, x, in the direction of the thickness, that in this case has been normalised to values $0.0 \leq x \leq 1.0$, to allow a more general use of the model. The value $x = 0$ is set at the centre of the plate and $x = 1$ represents its surface.

The heat transmission equation for orthogonal symmetry is then:

$$\alpha \frac{\partial^2 u}{\partial x^2} = \frac{\partial u}{\partial t} \tag{6.1}$$

where $u = u\{x, t\}$ is a normalised temperature, t is time and α the thermal diffusivity.

The physical and thermal properties of the steel are taken to be independent of temperature; the values used are averaged over the temperature range of interest. The temperature at time zero is considered uniform throughout and normalised to zero.

$$u\{x, 0\} = 0 \tag{6.2}$$

The boundary condition at $x = 0$ for both heating and cooling is given by the symmetry of the geometry,

$$\left.\frac{\partial u}{\partial x}\right|_{x=0} = 0 \tag{6.3}$$

During the heating stage, the boundary condition is (Section 6.2.1),

$$\left.\frac{\partial u}{\partial x}\right|_{x=1} = \frac{\dot{q}}{k} \tag{6.4}$$

where $\dot{q}$ is the heat flux at the surface. Finally, during the cooling stage, the temperature evolution is governed by heat extraction using water sprays (Section 6.2.2),

$$\left.\frac{\partial u}{\partial x}\right|_{x=1} = -\frac{h}{k} u\{1, t\} \tag{6.5}$$

Integrating the equation that governs the heating, gives the following expression:

$$u\{x, t\} = \frac{\dot{q}}{Lk} \sum_{n=1}^{\infty} \left(\operatorname{erfc}\left(\frac{\frac{2n+1-x}{\sqrt{k}}}{2\sqrt{t}} \right) - \operatorname{erfc}\left(\frac{\frac{2n+1+x}{\sqrt{k}}}{2\sqrt{t}} \right) \right) \tag{6.6}$$

The integration of equation 6.5 for the cooling process has led to a solution that is a function of an infinite sum of eigen-functions. Different expressions of that solution are

needed to deal with different time scales. To avoid the use of different functions and to keep the expressions used homogeneous, the solution proposed by Geiger & Poirier [116] using work done by Carslaw & Jaeger [117] has been adopted,

$$\begin{aligned} u\{x,t\} = \quad & u\{x,0\}\left[1-\left[\operatorname{erfc}\tfrac{1-x}{2\sqrt{Fo}}+\operatorname{erfc}\tfrac{1+x}{2\sqrt{Fo}}\right]+\right. \\ & \exp\Big(Bi(1-x)+Bi^2Fo\Big)\cdot\operatorname{erfc}\left[Bi\sqrt{Fo}+\tfrac{1-x}{2\sqrt{Fo}}\right]+ \\ & \left.\exp\Big(Bi(1+x)+Bi^2Fo\Big)\cdot\operatorname{erfc}\left[Bi\sqrt{Fo}+\tfrac{1+x}{2\sqrt{Fo}}\right]\right] \end{aligned} \tag{6.7}$$

where Fo is the Fourier number [116].

6.2.1 Induction Heating

The first stage in the induction hardening process is the heating of steel to the austenitisation temperature. Some heat is introduced into the material, within a thin surface layer. This can account for energy losses via the Joule effect due to eddy currents generated by the magnetic field. In reality, this layer changes in thickness, but also becomes more conductive as the temperature rises. Phase transformations can also change the conductivity of the material. Trying to simulate all these changes would lead to an intractable problem in the first attempt.

For the sake of simplicity, it is assumed that the power given by the induction coil generates a variable amount of current in the surface of the material. This in turn produces some heat flux which spreads into the steel. Hence, there is a constant heat flux on the outer layer of the plate.

It is also assumed that the process is temperature-controlled, and that the heat contribution is maintained until the target temperature is reached. At that point, the coil stops heating the material and cooling begins. In practice, the temperature is measured using a pyrometer, but only the surface temperature is monitored, whereas in reality, a gradient must exist between the inner and outer temperatures.

The monitoring system is expected to take periodic measurements of surface temperature. The time step used when evaluating the temperature evolution can then be made the same as the sampling time of the control system. Finally, it is also considered that no time should elapse at high temperatures before cooling begins.

6.2.2 Water Spray Quenching

After the outer surface reaches the desired temperature, the induction coil is switched off and water sprays cool the material rapidly. As this process starts immediately after heating, the temperature in the plate is not uniform. Naturally, a colder region inside the plate cannot start cooling before the hotter surface has cooled. To allow for this, different time scales are used as function of depth into the plate. The material at a given depth x does not begin to cool (time "stopped") until the temperature at a point $x + dx$ is lower than at x.

The cooling process continues until the temperature of the cooling fluid (or alternatively room temperature) is reached at the surface of the plate, or when the maximum number of iterations defined in the computer program is achieved.

6.2.3 Computer program

This model has been programmed using FORTRAN 77, and compiled in a UNIX operating system. The thickness of the plate, properties of steel and thermal variables of the process (density, specific heat, thermal conductivity, severity of the quench, initial and target temperatures, cooling water temperature) are included in the program so the only input needed is the heat flux at the surface. The output of the program is the evolution of temperature as a function of depth and time, during the induction heating and cooling stages.

6.2.4 Results and possible improvements

A plot of the calculated temperature evolution in the steel is shown in Figure 6.1. Several aspects are discussed below, including the main drawbacks of the model.

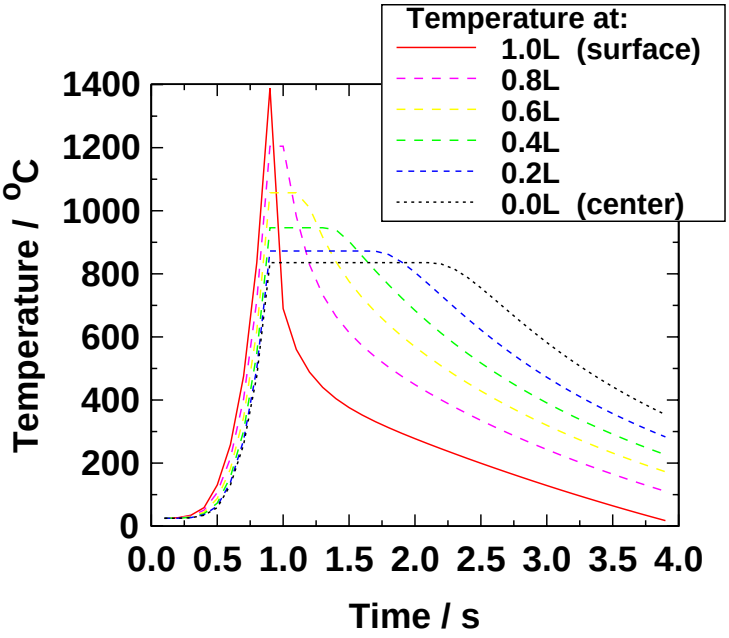

Figure 6.1: Example plot of the evolution of temperature at different depths according to the model

Some of the possible improvements include a better account of the period between the end of the induction heating stage and the point when the whole of the plate is cooling may lead to a more realistic model. In the current state of the model, a temperature gradient exists in the material even when the surface begins to cool. This is because some region of the inner core remains cooler than the more extern regions of the component. It is therefore expected that the core temperature is still rising whilst the surface is being cooled by the water sprays. It would also be interesting to take into account the possibility that this transition from induction heating to water cooling is not instantaneous. In a real industrial process, there is most likely a "dead time" in which the component is neither being heated nor sprayed with water. Other cooling phenomena may have to be taken

into account during that period.

However, analytical solutions for the heat equation can become increasingly difficult to integrate and lack flexibility for simple modifications. The development of a similar model but using any other symmetry, *i.e.* a cylinder, becomes more complex. For that reason, the next logical step is to adopt some numerical method to solve the heat equation. In this way the model could be left open to future improvements and would also represent a great advantage since its aim is to help monitor phase transformations that, in their turn, will influence the heat fluxes within the material.

6.3 Finite difference method

Differential equations sometimes cannot be solved analytically because of complex boundary conditions, changing properties or geometry. In such cases, the differential equation can be substituted by a *difference* equation and this last one is used to obtain approximate solutions of the original system.

In the difference equation the derivative terms are substituted by terms based on the difference of the function over an finite interval:

$$\left(\frac{\partial u}{\partial x}\right)_{m+\frac{1}{2}} \approx \frac{u_{m+1} - u_m}{\triangle x} \tag{6.8}$$

where u_m is the temperature at the node at position m. The temporal derivative is then written:

$$\left(\frac{\partial u}{\partial t}\right) \approx \frac{u^{v+1} - u^v}{\triangle t} \tag{6.9}$$

where u^v is the temperature at the node at instant v.

The resolution of the numerical methods is in principle limited only by the numerical

step-size and there may be a limit imposed by the time needed to reach an adequate computational solution.

A review of the literature for numerical methods used to integrate the heat equation for applications such as induction hardening and/or quenching problems, revealed that most researchers use an explicit method, such as the Euler method [32, 33]. The solutions of the equation for a point $u(x, t_i)$ are estimated using only derivatives of the function u calculated using only values of it at the time t_i, being the subindex i an indication of the time-step.

Calculations done using explicit methods are comparable with the exact values calculated analytically. Instabilities can occur in numerical solutions, for example due to round-off error growth. To be able to use numerical methods without risk, it is necessary to use small time and space increments. Some of the models found in the literature [33] automatically adjust the number of nodes during the course of the calculations to avoid such difficulties.

Implicit methods, on the other hand, tend to be far more accurate and do not suffer from extensive instability problems [118], but they require more complex algebra.

The Crank-Nicholson method [118] is an implicit finite difference method for solving parabolic differential equations and is used often to solve the heat equation. In this case, the second partial derivative is substituted by the average of two central difference quotients, one of them evaluated at the time t_i, and the other at t_{i+1}. In other words, instead of assuming that the second derivative of the function evaluated is zero during the time step studied, an average of the first derivative at the beginning and at the end of the temporal step is used.

This leads to slightly more complex algebra, but better performance. The method leads to a system of linear tridiagonal simultaneous equations that can be solved for each time step to obtain the profile of temperatures at given time t_i.

6.3.1 Notation used in both symmetries

As for the analytic model (Section 6.2), all the variables are normalised. The normalised temperature u is defined as:

$$u = \frac{T - T_{min}}{T_{max} - T_{min}} \tag{6.10}$$

where T_{max} is an arbitrary maximum temperature value (*e.g.* melting temperature), and T_{min} being another arbitrary minimum temperature (*e.g.* room temperature). Normalised time is denoted θ, and defined as the Fourier number:

$$\theta = \frac{\alpha t}{L^2} \tag{6.11}$$

The spatial coordinate X is normalised with respect of the thickness, and as in the previous section is defined $x = 0$ in the centre of the thickness of the plate and $x = 1$ at its surface:

$$x = \frac{X}{L} \tag{6.12}$$

For cylindrical symmetry, the normalised spatial co-ordinate is referred to as r, normalised with respect to the radius of the cylinder R. The spatial step is denoted by $\triangle X$ and the time step by $\triangle t$. Once normalised they become of course $\triangle x$ and $\triangle \theta$. The heat flux at the surface during the induction heating stage is also normalised, but as the expressions are different for the plate and the cylinder symmetry, these will be discussed in later sections (Section 6.3.2 and Section 6.3.3 respectively).

To simplify the mathematical expressions, a parameter P is defined as,

$$P = \frac{\triangle \theta}{\triangle x^2} \tag{6.13}$$

Two sets of indices will be used, superindices (0, 1, ... v, v+1, ... ∞) refer to the time count and subindices (0, 1,... m, ... N), to the spatial count, with $N = L/\triangle X$.

6.3.2 The Crank-Nicholson method applied to a plate

Equation 6.1 is the heat transmission equation for a plate. The corresponding discretised equations are 6.8 and 6.9. The initial conditions are described in equations 6.2 and 6.3, with the boundary conditions expressed by equation 6.4 for heating, and equation 6.5 for cooling.

Using the Crank-Nicholson method, the temperature at position m at the next temporal step, $v+1$, can be calculated as:

$$u_m^{v+1} = u_m^v + \frac{1}{2}\left[\frac{\partial^2 u_m^v}{\partial x^2} + \frac{\partial^2 u_m^{v+1}}{\partial x^2}\right] \triangle\theta \tag{6.14}$$

being the second space derivatives of the temperature function calculated from equation 6.8:

$$\left(\frac{\partial^2 u}{\partial x^2}\right)_m \approx \frac{1}{\triangle x^2}\left[u_{m-1} - 2\,u_m + u_{m+1}\right] \tag{6.15}$$

Applying expression 6.14 to all the nodes from $m = 0$ to N, and considering the boundary conditions (equations 6.3 to 6.5), and finally reordering them to have all the v terms on one side of the equality and the $v+1$ terms on the other, leads to the following expressions:

$$(1+P)\,u_0^{v+1} - P\,u_1^{v+1} = (1-P)\,u_0^v + P\,u_1^v \tag{6.16}$$

$$-\frac{P}{2}\,u_{m-1}^{v+1} + (1+P)\,u_m^{v+1} - \frac{P}{2}\,u_{m+1}^{v+1} = \frac{P}{2}\,u_{m-1}^v + (1-P)\,u_m^v + \frac{P}{2}\,u_{m+1}^v \tag{6.17}$$

$$-P\,u_{N-1}^{v+1} + (1+P)\,u_N^{v+1} = P\,u_{N-1}^v + (1-P)\,u_N^v + \tilde{q} \tag{6.18}$$

during heating.

$$-P\,u_{N-1}^{v+1} + (1 + P + \frac{Bi\,\triangle x\,P}{2})\,u_N^{v+1} = P\,u_{N-1}^{v} + (1 - P - \frac{Bi\,\triangle x\,P}{2})\,u_N^{v} \quad (6.19)$$

during cooling.

The normalised heat flux through the surface of the plate is calculated as:

$$\tilde{q} = \frac{\triangle\theta\,\dot{q}\,L}{k\,(T_{max} - T_{min})} \quad (6.20)$$

where $\dot{q}$ is in W m^{-2}. This heat flux is not a linear factor in the equation, so it cannot be included in the coefficient matrices. In this situation, the normalised heat flux is added directly at the end of each step of the calculation.

Equations 6.16 to 6.19 represent a double set of simultaneous linear equations. As all the parameters in the second part of the matricial system are known, this becomes a vector of independent terms.

$$\begin{pmatrix} 1+P & -P & 0 & \cdots & \cdots & 0 \\ -\frac{P}{2} & 1+P & -\frac{P}{2} & 0 & & \vdots \\ 0 & \ddots & \ddots & \ddots & 0 & \vdots \\ \vdots & \ddots & \ddots & \ddots & \ddots & 0 \\ 0 & \cdots & \cdots & 0 & -P & 1+P\,(1+\frac{Bi\,\triangle x}{2}) \end{pmatrix} \begin{pmatrix} u_0 \\ \vdots \\ u_m \\ \vdots \\ u_N \end{pmatrix}^{v+1} =$$

$$\begin{pmatrix} 1-P & P & 0 & \cdots & \cdots & 0 \\ \frac{P}{2} & 1-P & \frac{P}{2} & 0 & & \vdots \\ 0 & \ddots & \ddots & \ddots & 0 & \vdots \\ \vdots & \ddots & \ddots & \ddots & \ddots & 0 \\ 0 & \cdots & \cdots & 0 & P & 1-P\,(1+\frac{Bi\,\triangle x}{2}) \end{pmatrix} \begin{pmatrix} u_0 \\ \vdots \\ u_m \\ \vdots \\ u_N + \tilde{q} \end{pmatrix}^{v} \quad (6.21)$$

This system of equations can be solved for each consecutive time step to find the evolution of the temperature at different depths into the material at time t. All the variables controlling the heating ($\tilde{q}$) and cooling (Bi) stages of the process have been

included in equation 6.21 for completeness. Only the relevant ones would have non-zero values during each of these stages.

6.3.3 The Crank-Nicholson method applied to a cylinder

When analysing the case of a cylindrical component, such as a shaft, the transmission heat equation takes the form:

$$\frac{\partial u}{\partial t} = \alpha \left[\frac{\partial^2 u}{\partial r^2} + \frac{1}{r} \frac{\partial u}{\partial r} \right] \tag{6.22}$$

The specific differential terms of the cylindrical symmetry are detailed now:

$$\left(\frac{\partial u}{\partial r} \right)_m \approx \frac{u_{m+1} - u_{m-1}}{2 \triangle x} \tag{6.23}$$

and

$$\frac{1}{r} = \frac{1}{m \triangle x} \tag{6.24}$$

Using equation 6.22, including the differential terms in equations 6.8, 6.23 and 6.24 and boundary conditions from equations 6.3 to 6.5, considering nodes $m = 0$ to $m = N$, it is found that,

$$u_0^{v+1} = u_0^v + \frac{\triangle \theta}{2 \triangle x^2} \left[(u_1^v - u_0^v) + \left(u_1^{v+1} - u_0^{v+1} \right) \right] \tag{6.25}$$

$$u_m^{v+1} = u_m^v + \frac{\triangle \theta}{2 \triangle x^2} \left[\frac{2m+1}{2m} u_{m+1}^{v+1} - 2 u_m^{v+1} + \frac{2m-1}{2m} u_{m-1}^{v+1} + \frac{2m+1}{2m} u_{m+1}^v - 2 u_m^v + \frac{2m-1}{2m} u_{m-1}^v \right] \tag{6.26}$$

$$u_N^{v+1} = u_N^v + \frac{\triangle \theta}{2 \triangle x^2} \left[\frac{N-1}{N} u_{N-1}^{v+1} - \frac{N-1}{N} u_N^{v+1} + \frac{N-1}{N} u_{N-1}^v - \frac{N-1}{N}) u_N^v \right] + \tilde{q} \tag{6.27}$$

$$u_N^{v+1} = u_N^v + \frac{\triangle\theta}{2\triangle x^2}\left[\frac{N-1}{N}u_{N-1}^{v+1} - \frac{N-1}{N}(1+Bi\triangle x)\,u_N^{v+1} + \frac{N-1}{N}u_{N-1}^{v} - \frac{N-1}{N}(1+Bi\triangle x)\,u_N^{v}\right] \tag{6.28}$$

Equation 6.27 is used during heating and equation 6.28 during cooling. Reordering and writing the equation system in matricial form, gives:

$$\begin{pmatrix} 1+P & -P & 0 & \cdots & \cdots & 0 \\ -\frac{(2m-1)P}{4m} & 1+P & -\frac{(2m+1)P}{4m} & 0 & & \vdots \\ 0 & \ddots & \ddots & \ddots & 0 & \vdots \\ \vdots & \ddots & \ddots & \ddots & \ddots & 0 \\ 0 & \cdots & \cdots & 0 & -\frac{P}{2}\frac{N-1}{N} & 1+\frac{P}{2}\frac{N-1}{N}(1+Bi\triangle x) \end{pmatrix} \begin{pmatrix} u_0 \\ \vdots \\ u_m \\ \vdots \\ u_N \end{pmatrix}^{v+1} =$$

$$\begin{pmatrix} 1-P & P & 0 & \cdots & \cdots & 0 \\ \frac{(2m-1)P}{4m} & 1-P & \frac{(2m+1)P}{4m} & 0 & & \vdots \\ 0 & \ddots & \ddots & \ddots & 0 & \vdots \\ \vdots & \ddots & \ddots & \ddots & \ddots & 0 \\ 0 & \cdots & \cdots & 0 & \frac{P}{2}\frac{N-1}{N} & 1-\frac{P}{2}\frac{N-1}{N}(1+Bi\triangle x) \end{pmatrix} \begin{pmatrix} u_0 \\ \vdots \\ u_m \\ \vdots \\ u_N + \tilde{q} \end{pmatrix}^{v} \tag{6.29}$$

Once again, this system of equations can be solved for each consecutive time step to find the evolution of the temperature at different depths into the cylinder at time t. All the variables controlling the heating ($\tilde{q}$) and cooling (Bi) stages of the process have been included in equation 6.29 for completeness. Only the relevant ones would have a non-zero value during each of these stages. In any case, air convection will occur during the whole process, except when the water sprays are engaged. Radiation losses may become significant at the end of the heating stage and beginning of the cooling one, so they could also be considered.

For cylindrical symmetry, the heat flux is measured per unit length, so the corresponding normalising function is:

$$\tilde{q} = \frac{\triangle\theta\,\dot{q}}{k\,(T_{max} - T_{min})} \tag{6.30}$$

where $\dot{q}$ is in W m^{-1}.

6.3.4 Implementation of the model and improvements introduced

The model presented above has been used to predict the temperature evolution during the entire process of induction hardening. A detailed description of the induction hardening process has already been given in Section 6.2.1 and Section 6.2.2, so only the new additions to the model will be outlined here.

In the analytic model, there was no delay between the time when the inductors were switched off and when the water spraying commenced. In the present numerical model a dead time has been introduced in which only air convection cools the material, which is closer to reality.

Even though most of the physical and thermal properties have been considered constant, the numerical model allows the use of properties that are a function of temperature (or other variables), without major changes.

The implementation of the model has been programmed in FORTRAN 77. The same program is able to deal with plate and cylinder morphologies. All the variables needed are fed into the model via a formatted input file, and the outputs are also written into a file, in a format suitable for most mathematical or statistical manipulation software packages.

An example of the results calculated using the numerical model is presented in Fig. 6.2, corresponding to a thick plate heated at the rate shown in the figure.

The thermal cycle is very rapid; the rise in temperature affects mainly the surface of the plate, while its core remains cool. As in this example the core remains cooler than the surface during most of the cycle. At some point, it also contributes to levelling the temperature gradient between the core and the subsurface region, so that the decrease of temperature of the latter is not only due to surface cooling but also to heat transfer towards the core.

The temperature evolution during induction hardening of the different parts of a constant velocity joint can be calculated using the cylinder mode of the model for the shaft

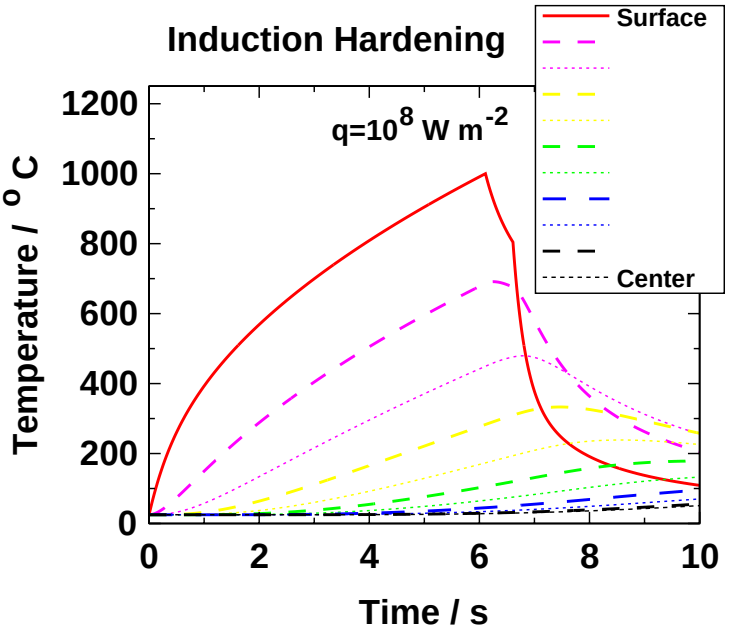

Figure 6.2: Example plot of the evolution of temperature at different depths in a thick plate during induction heating as calculated using the finite difference model.

and the plate mode for the bell. The calculated curves for thin cylinder and thin plate are shown in Figures 6.3 and 6.4.

The heat flux used in the calculations is just a heuristic approximation based in some parameters of the process and the different geometries, and considering in both cases the use of a magnetic field with a power of 150 kW.

6.4 Comparison with measurements

Several methods of comparing the behaviour predicted using the numerical model against experimental data have been examined. The surface temperature can be measured, at least during the heating stage, using a pyrometer. This is not practical for the cooling stage, when water sprays are applied.

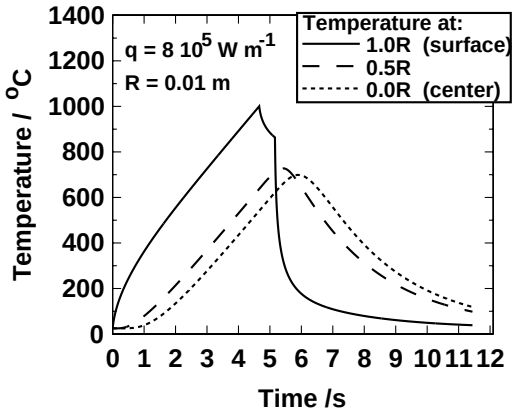

Figure 6.3: Thin cylinder case. This mode of the model is used to modellise induction hardening of the shaft of an outer race bell for a constant velocity joint.

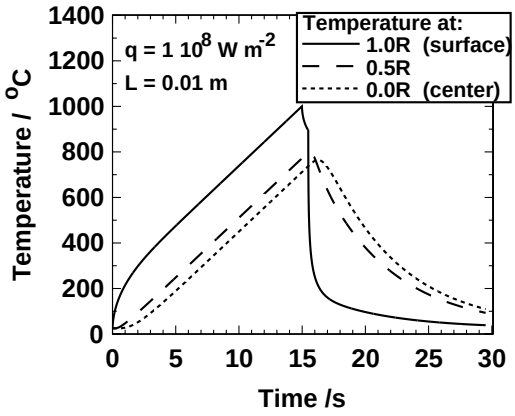

Figure 6.4: Thin plate case. This mode of the model is used to model induction hardening of the bell of a constant velocity joint.

Accurate measures of power used to generate the magnetic field can also give an indication of the heat generated at the surface of the metal during induction heating, but unknown yield factors would limit the usefulness of such measurements to an estimate of the maximum efficiency reachable, without accounting for losses.

The cooling stage of the process can be characterised directly using a thermocouple attached to the surface of the component, or buried underneath. Caution must be exercised since induction currents might be induced in the thermocouple, distorting the measurement. There is, however, an issue as to whether the thermocouple would survive the heating stage of the process and still be able to make correct measurements during quenching.

GKNT has measured the evolution of temperature during induction hardening. The results of one of these tests have been compared against the calculations obtained using the numeric model. This test was conducted on a *tulip GI2300i*, a component of similar characteristics and morphology to an outer race bell in a constant velocity joint. For the test, the component was manufactured in Inconel, to avoid phase transformation. Several holes were drilled in the sides of the component and thermocouples fitted to measure the temperature at 1 mm of depth from the outer surface (Fig. 6.5). The characteristics of

the alloy are described in Table 6.1.

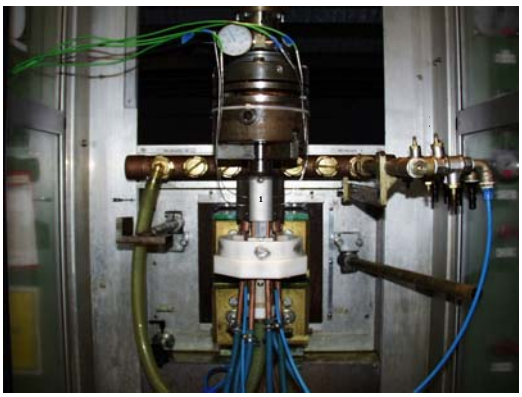

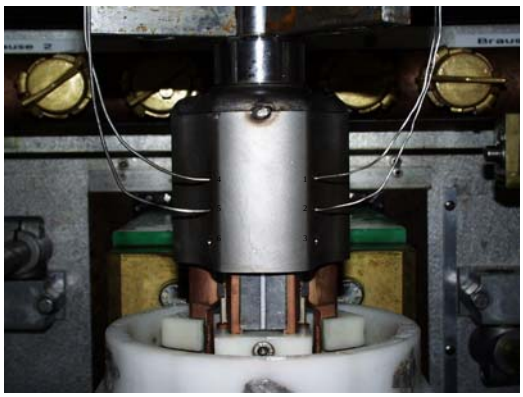

Figure 6.5: Experimental arrangement for temperature measurement during induction hardening

Density	$8.5 \cdot 10^3\,\mathrm{kg\,m^3}$
Specific heat	$460\,\mathrm{J\,kg^{-1}\,K^{-1}}$
Resistivity	$9.8 \cdot 10^{-7}\mathrm{ohm\,m}$
Conductivity	$15.5\,\mathrm{W\,K^{-1}\,m^{-1}}$

Table 6.1: Characteristics of Inconel. All values refer to 20°C.

The numerical model needs several input parameters, some of which are not easily measured (dead time, input heat flux, water sprays heat transfer coefficient), and others which are arbitrary parameters given by the design of the model (maximum, start and water temperatures). Values for the three parameters mentioned first can be inferred from experimental data, by using them as fitting parameters to adjust the modelled curve. All these parameters are summarised in Table 6.2.

The accuracy of the predictions is remarkable (Figure 6.6), especially above 300°C, where most of the studied phenomena occur. The small discrepancies between measured and calculated values are easily explained. During heating the heat flux induced into the metal has been considered constant. However, this a parameter that will certainly change as a function of temperature. The yield of the installation will also increase with time until

Start temperature	18 °C
Water temperature	18 °C
Maximum temperature	1400 °C
Target temperature	1025 °C
Induction input heat flux	$1.9 \cdot 10^8\,\mathrm{W\,m^{-2}}$
Water sprays heat transfer	$22 \cdot 10^3\,\mathrm{W\,m^{-2}\,K^{-1}}$
Dead time	0.25 s

Table 6.2: Input parameters used by the finite difference model.

it reaches a steady state value, instead of starting to function at that value, as assumed in the calculations. During cooling, a similar simplification has been used, allowing the heat transfer coefficient of the water spraying system to remain constant throughout the cooling process. This assumption still gives good predictions at high temperatures, but clearly does not hold when the temperature of the component approaches room temperature.

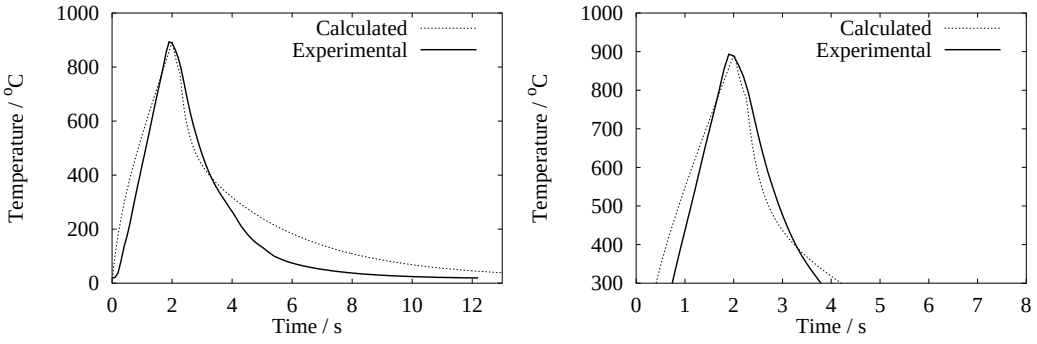

(a) Complete induction hardening process.

(b) Detail of the curves at the temperatures of interest.

Figure 6.6: Comparison of the measured thermal evolution and the predicted one for a point 1 mm below the surface of the component.

6.5 Conclusions

To deal with phase transformations during the manufacturing process, it is necessary to measure or calculate the thermal cycle. A thermal model has therefore been developed for the induction hardening process, describing the two main stages of induction-heating and water-quenching.

As a first approach, an analytical model was integrated but the difficulty in improving it to suit the real process suggested another approach was needed and a second model was developed.

The second model is based on the numerical integration of the heat transmission equation using an explicit method viz., Crank-Nicholson [118]. This method is well known for its reliability and stability and used commonly to integrate parabolic differential equations like the heat transmission equation. Surprisingly, most authors who have studied the induction hardening process have used simpler explicit models.

Numerically integrated expressions have been presented for plate and cylinder symmetries, and implemented in a FORTRAN program.

This model has been compared against a limited set of experimental measurements and has proven to be adequately accurate for its purpose.

Chapter 7

Model for austenitisation of hypoeutectoid steels

7.1 Introduction

The aim of the work presented here was to use phase transformation theory to construct a model for austenite formation, taking into account the chemical composition and the characteristic microstructure of a hypoeutectoid steel. Classical nucleation theory and diffusion-controlled growth equations are used to determine the progressive transformation of the different phases into austenite.

A model such as this may be useful in diverse applications, ranging from the calculation of continuous heating diagrams of steels of precise composition and microstructure, to the simulation and monitoring of manufacturing processes.

7.1.1 Austenitisation of a hypoeutectoid steel

The phenomena associated with the austenitisation of a hypoeutectoid steel are more complex than for the same transformation in other alloys. The equilibrium microstructure is composed of allotriomorphic ferrite and pearlite, the latter being a composite of ferrite and cementite. In two-dimensional sections a colony of pearlite has the appearance of alternate lamellae of ferrite and cementite. In three dimensions, each colony consists of an interpenetrating bi-crystal of ferrite (α) and cementite (θ) [126]. Ferrite has a very low solubility for carbon and hence, on its own, only begins to transform to austenite at high temperatures. But if cementite decomposes and yields its carbon to the transformation front, the reaction from ferrite to austenite can proceed at lower temperatures.

It is logical to expect that the initiation of austenitisation in a hypoeutectoid steel is in pearlite, where the diffusion distances for carbon are small. The reaction can then proceed into the remaining ferrite once the pearlite is consumed.

New grains of austenite nucleate at pearlite colony boundaries [45]. As the diffusion distances for carbon from the dissolving cementite to the ferrite / austenite interface are small (smaller or equal to half the spacing characteristic of the pearlite), these grains grow extremely fast, to the extent that pearlite is sometimes assumed to transform instantly [45]

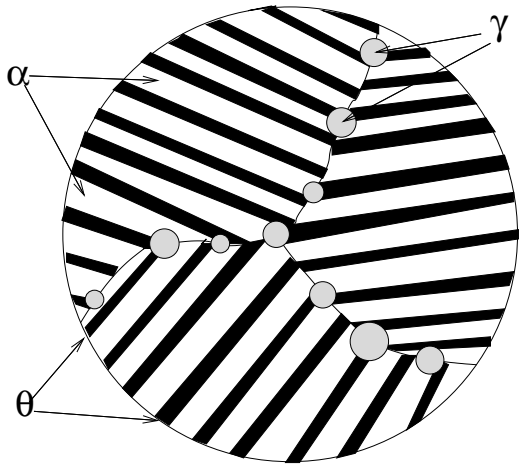

Figure 7.1: Preferential nucleation sites of austenite in pearlite colonies. α stands for ferrite, θ for cementite and γ for austenite.

into austenite, followed by the advance of the interface into the ferrite.

When the austenite starts to grow into the ferrite, carbon has to partition to the austenite/ferrite interface for the reaction to proceed, so the diffusion rate of carbon in austenite becomes one of the limiting factors, but the distances involved in this diffusion process are much larger and the rate of transformation will depend on the morphology, distribution and volume fractions of the phases present.

Any model aiming to describe the austenitisation of a hypoeutectoid steel has to deal with all the parameters referred to above. Austenitisation must clearly be microstructure sensitive. Thermodynamic equilibrium limits the extent of transformation at long times, while nucleation of austenite in pearlite colonies and diffusive processes are expected to control the rates of transformation.

The model described in this work includes nucleation of new austenite grains at the edges of the pearlite colonies. These grains are assumed to grow until the pearlite has completely transformed into austenite, after which allotriomorphic ferrite transforms.

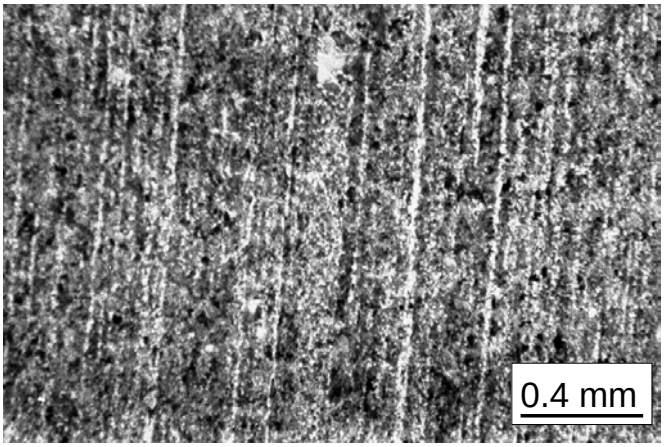

Figure 7.2: Micrograph of hypoeutectoid steel showing a heavily banded microstructure. Bands of ferrite (white) align in the direction of rolling, between parallel bands composed mostly by pearlite colonies (dark).

7.2 Mathematical modelling of austenitisation

7.2.1 Characterisation of the microstructure

A hypoeutectoid carbon steel presents two distinctive microstructures, groups of pearlite colonies and some ferrite grains between them. This distribution of phases is even more accentuated in the case of steels containing chemical segregation, which on rolling leads to a banded structure, as can be seen in Fig 7.2.

If it is assumed that the latter is always the case, it is possible to define the microstructure of the steel using four independent parameters, as shown in Figures 7.3 and 7.4. In a more general microstructure, it is assumed that these parameters would still represent the extent of each phase (ignoring its internal microstructure) in a way which accounts for austenite formation.

The parameters l_α and l_p define the thickness of the ferrite and pearlite layers respectively. Their sum gives l_h. In a microstructure that is not heavily banded, l_α and l_p are used in an abstract way to define the relative volume fractions of allotriomorphic ferrite

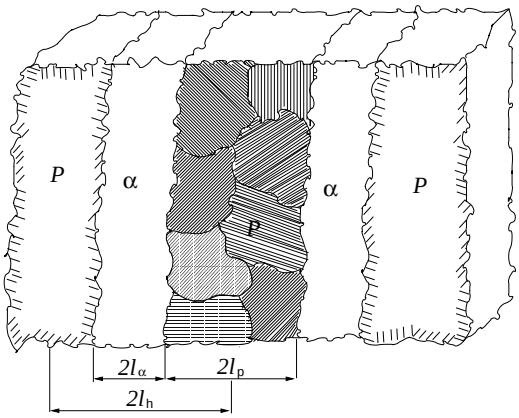

Figure 7.3: Definition of microstructure parameters l_p, l_α and l_h, in a heavily banded microstructure. P denotes pearlite regions and α the allotriomorphic ferrite regions. These parameters are defined in such a way that they can still be used in other cases where microstructure does not show such level of directionality.

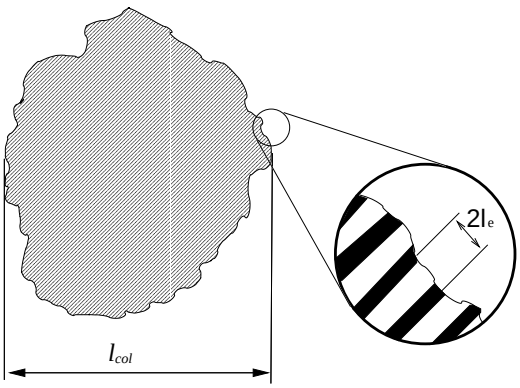

Figure 7.4: Definition of microstructural parameters l_{col} and l_e. The later characterises the distance between the midthickness of adjacent ferrite and cementite laminae. l_{col} is meant to be a representative dimension of the average pearlite colony.

and pearlite. Assuming that the carbon content of ferrite is zero, and that pearlite as a whole has the eutectoid carbon composition (about 0.77 wt %), l_p can be written:

$$l_p = \frac{l_h \, w_C}{0.77} = \frac{(l_\alpha + l_p) w_C}{0.77} \tag{7.1}$$

where w_C is the average weight percent of carbon in the alloy.

The dimension l_{col} of a typical colony is illustrated in Figure 7.4, and in the present work it has been measured using the linear mean intercept method. Finally, l_e characterises the distance between the midthickness of adjacent ferrite and cementite laminae in the eutectoid microstructure.

There is no need to define the thicknesses of the cementite and ferrite layers in pearlite because it is assumed here that both layers decompose into austenite at a common transformation front, and the cementite layer is assumed to be much thinner than the ferrite one.

All the quantitative measurements used during this study were conducted following Sellars [127] unless stated otherwise, and stereological corrections, when needed, were done as in Chang *et al.* [128].

7.2.2 Quantitative measurements

7.2.2.1 Volume fraction measurements in microstructures with several phases

The determination of the volume fraction of the various phases present in the microstructures under study has been done following a method by Sellars [127]. A grid of suitable spacing is superimposed on to micrographs of the microstructure. The spacing of the grid needs to be fine enough to allow some of the intersections of the grid to lie in every phase under consideration. The volume fraction of phase β in the micrograph can be determined from the proportion of grid intersections laying on it, determining for each micrograph

$$v_\beta = \frac{n_\beta}{n_T} \tag{7.2}$$

where v_β is the volume fraction of phase β, n_β is the number of grid intersections that lay on phase β on the micrograph and n_T the total intersections of the grid onto the micrograph. The standard deviation of the measure σ is determined as

$$\sigma = \sqrt{\frac{1 - v_\beta}{n_\beta}} \cdot v_\beta \tag{7.3}$$

This procedure is repeated for a number of micrographs, to obtain a reliable measure with an acceptably low variance.

7.2.2.2 Grain size measurement on multiphase microstructures

To determine the grain size of a given phase β the volume fraction v_β of such phase has to be measured first (section 7.2.2.1). A similar grid to the one used to determine the volume fraction can be used, but the grid spacing has to be fine enough so that each grain of the phase considered is intersected by at least one of the horizontal lines (alternatively vertical lines can be used) of the grid. If the number of grains intersected by all the lines (horizontal or vertical, but not both) contained on the micrograph is N_β, and L_T is the real length of the lines used, the planar mean intersect is [127],

$$\bar{l}_\beta = \frac{L_T}{N_\beta v_\beta} \tag{7.4}$$

and the standard deviation of the measure $\sigma_{\bar{l}}$ is [127],

$$\sigma_{\bar{l}} = \frac{0.65}{\sqrt{N_\beta}} \cdot \bar{l}_\beta \tag{7.5}$$

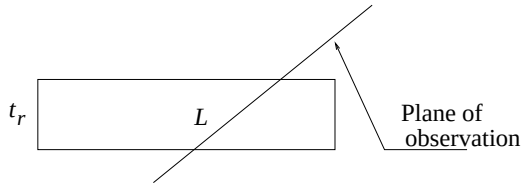

Figure 7.5: Measure of the thickness of a plate-like structure on an arbitrary plane.

This method is only valid if the microstructure is equiaxic. If this is the case, the measure of planar mean intersection can be corrected to a three dimension intersect diameter, considering a tetrakaidecahedron shape model as [103],

$$\bar{D}_\beta = \frac{\pi}{2}\bar{l}_\beta \tag{7.6}$$

7.2.2.3 Stereological correction

When the thickness of plate-like structures have been measured, a stereological correction following the method used by Chang and Bhadeshia [128] has been used. If the shortest distance perpendicular to the longest dimension of the plate in the plane of the micrograph is measured (figure 7.5), the relationship between the average measure $\bar{L}$ and the real thickness of the plate t_r is,

$$t_r = \frac{2}{\pi}\bar{L} \tag{7.7}$$

7.3 Mathematical modelling of austenitisation

7.3.1 Nucleation of austenite

Austenite nucleates at the surfaces of the pearlite colonies [45]. Classical nucleation theory [6] is used to calculate the dependence of nucleation rate on temperature:

$$I = C_0 N_0 \frac{6}{l_{col}} \frac{kT}{h} \exp\left(-\frac{G^* + Q}{RT}\right) \tag{7.8}$$

where I is the nucleation rate per unit time in a single colony, N_0 is the number of nucleation sites per unit area of colony interface, and C_0 is a fitting parameter. As the active nucleation sites are all assumed to be located at the surface of the pearlite colonies, and not evenly distributed in the volume of material the ratio between colony surface to volume has to be determined. This factor takes into account the coarseness of the pearlitic microstructure. This calculation gives the factor $\frac{6}{l_{col}}$. k is the Boltzmann constant; R the gas constant; h the Planck constant; Q is an activation energy representing the barrier for the iron atoms to cross the interface, estimated to be 270,000 J mol^{-1} [129]. T is the absolute temperature and G^* is the activation free energy for nucleation.

The activation free energy for nucleation is determined from a balance of interface and volume energy of the critical nucleus, which is assumed to be spherical. The austenite/ferrite interface energy at nucleation is considered to be $\sigma_{\gamma\alpha} = 0.025$ J m^{-2} [129]. Several authors [130, 131, 132, 133] have studied the effect of composition on the change in free energy on transformation from ferrite to austenite, but the change of free energy from a cementite and ferrite mixture to austenite has been determined in this work using a thermodynamic package, MTDATA [3].

7.3.1.1 Determination of the change in free energy between ferrite and cementite mixtures and austenite

The increase in free energy when a mixture of ferrite and cementite transforms into austenite can be determined using commercial software such as MTDATA [3]. MTDATA is capable of performing equilibrium and paraequilibrium state calculations for multicomponent systems containing a wide range of phases. It works by combining experimentally determined information for unary, binary and even ternary sub-systems and using thermodynamic theory to determine what happens in larger systems. Individual phases can be included or excluded at will in the calculations and the free energy of the system determined.

However, an analytical expression was desired in order to produce a stand-alone computer model which can be used without having to access to MTDATA. Therefore, a set of calculations was designed, to create a database to train a neural network. The analytical expression of the neural network has been used in the model. The selection of calculations has been such that the chemical composition of the steel has been varied about some standard alloy. Experiment design methods [134, 135] were used to determine the representative combinations, as detailed in section 7.3.1.2.

All the different alloys designed in section 7.3.1.2 were studied using MTDATA [3], using the database *ALL*, over the temperature range 373-1873 K, in steps of 25 K, assuming paraequilibrium. Only ferrite (BCC_A2) and cementite were allowed in a first set of calculations and only austenite (FCC_A1) in the second set. An automatised computer program was used to read the outputs from MTDATA, determine the free energy change between both cases and create a database including all the relevant data (composition, temperature of the calculation and free energy change).

The data obtained from MTDATA were used to train a neural network, using software developed by Sourmail [136], based on the work done by MacKay [137, 113]. The network has 8 input variables (7 elements and temperature) and 13 hidden units. The analytical function thus created can then be incorporated into a stand-alone computer model.

7.3.1.2 Factorial experiment design

In order to design an optimum set of compositions for the MTDATA calculations, a fractional factorial experiment design method has been used [134, 135]. A factorial experiment design gives the maximum efficiency in the estimation of effects when there are no interactions. In the case where interactions exist between the parameters studied, or factors, the precise intensity of the interaction can be determined even when the nature of such interaction is unknown and the conclusions obtained hold for a wide range of conditions [135].

The amount of experiments needed can be reduced using a fractional design, associating one or more of the highest interactions with one of the primary factors [134]. In this case the effect of molybdenum has been associated with the simultaneous interaction of all the other elements considered.

32 different compositions were considered, so that none of the 6 factors (element composition, excluding iron: C, Si, Mn, Cr, Ni, Mo) is confused with others or interactions lower than the 4th degree. The generator of the fractional matrix is Mo = C·Si·Mn·Cr·Ni. The design matrix is shown in Table 7.1.

The higher and lower level of each composition corresponds in most cases to twice and half the composition of a standard steel used in induction hardening. For the case of carbon a 0.77 wt.% has been used as the higher level. The standard composition was also added to the list of compositions used.

7.3.2 Diffusion-controlled growth of austenite in steel

Once the new grains of austenite have nucleated, their rate of growth, up to the equilibrium volume fraction, has been assumed to be determined by the diffusion of carbon in austenite, from the decomposing cementite, to the boundary between ferrite and austenite. The velocity of that interface can be determined from a mass balance and the relevant diffusion equation.

The flux of carbon atoms in austenite at the ferrite/austenite interface is:

Level	1	2	3	4	5	6	7	8	9	10	11	12	13	14	15	16
C	-	+	-	+	-	+	-	+	-	+	-	+	-	+	-	+
Si	-	-	+	+	-	-	+	+	-	-	+	+	-	-	+	+
Mn	-	-	-	-	+	+	+	+	-	-	-	-	+	+	+	+
Cr	-	-	-	-	-	-	-	-	+	+	+	+	+	+	+	+
Ni	-	-	-	-	-	-	-	-	-	-	-	-	-	-	-	-
Mo	-	+	+	-	+	-	-	+	-	+	+	-	+	-	-	+

Level	17	18	19	20	21	22	23	24	25	26	27	28	29	30	31	32
C	-	+	-	+	-	+	-	+	-	+	-	+	-	+	-	+
Si	-	-	+	+	-	-	+	+	-	-	+	+	-	-	+	+
Mn	-	-	-	-	+	+	+	+	-	-	-	-	+	+	+	+
Cr	-	-	-	-	-	-	-	-	+	+	+	+	+	+	+	+
Ni	+	+	+	+	+	+	+	+	+	+	+	+	+	+	+	+
Mo	-	+	+	-	+	-	-	+	-	+	+	-	+	-	-	+

Table 7.1: Design matrix for a fractional factorial experiment design considering 6 factors (C, Si,Mn, Cr, Ni, Mo) and a fractional design generated by Mo = C · Si · Mn · Cr · Ni. + and – represent the higher and lower levels of composition considered for each component (Level + and Level – in Table 7.2).

wt.%	C	Si	Mn	Cr	Ni	Mo
Standard	0.54	0.21	0.77	0.18	0.11	0.03
Level +	0.77	0.42	1.5	0.36	0.22	0.06
Level –	0.27	0.10	0.35	0.09	0.05	0.01

Table 7.2: Composition values used in the calculations. A representative steel composition has been used as the base, and then for each element, a level+ composition has been considered, which is in most cases twice the average one (with the exception of carbon, where the eutectoid composition for a carbon steel has been used), and a level– composition, half of that of the average.

$$D\left(\frac{\partial c}{\partial r}\right)_{r=r^{int}} dt \tag{7.9}$$

where $D = D\{c, T\}$ is the diffusion coefficient of carbon in austenite; c the carbon content of the steel; and r^{int} the position of the interface.

The number of atoms involved in the boundary advance is determined by:

$$(c^{\gamma\alpha} - c^{\alpha\gamma})\, dr \tag{7.10}$$

where $c^{\gamma\alpha}$ and $c^{\alpha\gamma}$ are the composition of austenite and ferrite in paraequilibrium with each other at the γ/α interface, and are calculated following Akbay *et al.* [61].

Equating Eq. 7.9 and Eq. 7.10 gives

$$D\left(\frac{\partial c}{\partial r}\right)_{r=r^{int}} dt = (c^{\gamma\alpha} - c^{\alpha\gamma})\, dr \tag{7.11}$$

so that the velocity of the interface v_{int} can be determined as follows

$$v^{int} = \frac{dr}{dt} = \frac{D}{(c^{\gamma\alpha} - c^{\alpha\gamma})}\left(\frac{\partial c}{\partial r}\right)_{r=r^{int}} \tag{7.12}$$

The determination of the concentration gradient in a situation with moving boundaries (Stefan problem Fig. 7.6) does not have a simple solution [138]. Using the following approximation,

$$\left(\frac{\partial c}{\partial r}\right)_{r=r^{int}} \approx \frac{c^{\gamma\theta} - c^{\gamma\alpha}}{r} \tag{7.13}$$

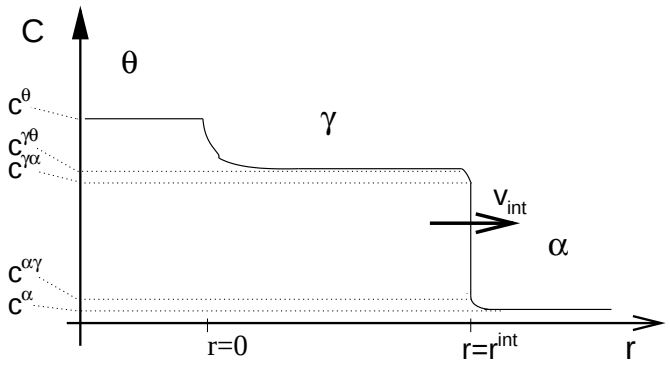

Figure 7.6: Schematic plot of the diffusion problem of a concentration gradient with moving boundaries, known as Stefan problem, needed to determine the carbon content and position of the interface.

the velocity of the interface can be calculated to be:

$$v^{int} \approx \frac{D}{r}\left(\frac{c^{\gamma\theta} - c^{\gamma\alpha}}{c^{\gamma\alpha} - c^{\alpha\gamma}}\right) \tag{7.14}$$

It is important to note that r in Eq. 7.14 is strictly, the diffusion distance of carbon in austenite. Unless the direction of that flux and the direction of advancement of the interface are coincident, the position of the interface will have to be determined as $v^{int}\,t$, where t is time.

7.3.3 Transformation of pearlite

The nucleation rate of austenite in a pearlite colony is I (Eq. 7.8). Each active nucleus develops in one of the layers or "slices" of ferrite surrounded by cementite. The newly nucleated grains grow as hemispheres until they reach a size of the order of l_e and a steady growth rate, and start growing into the colony. If the geometry of the pearlite colony is assumed spherical, each ferrite layer is then a flat disc of radius R_1. As the new austenite grains grow from the edges of these discs (Fig. 7.7), the area already transformed can be accounted as

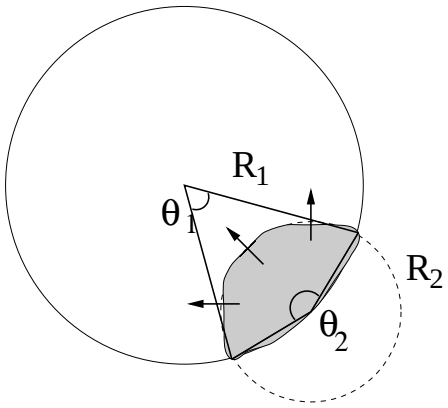

Figure 7.7: Transformation to austenite nucleates at the interface between pearlite colonies or between a pearlite colony and ferrite, and the newly formed phase grows into the grain dissolving simultaneously ferrite and cementite. The already transformed area in a single layer of ferrite and pearlite laminae is shown in grey.

$$A = \frac{1}{2}\left[R_1^2\ (\theta_1 - \sin\theta_1) + R_2^2\ (\theta_2 - \sin\theta_2)\right] \tag{7.15}$$

where A is the area that has already transformed (using the average velocity of advance of the interface, as described below). R_1 is the radius of the slice and R_2 the position of the interface from the edge of the colony. θ_1 and θ_2 are the angles containing the transformed area from the centre of each circle.

The advancement direction of the interface is perpendicular to the diffusion of carbon. The velocity of the interface determined in section 7.3.2 is a function of the diffusion distance r. That obviously means that the advancing front of austenite will show different velocities from the α/θ interface to the centre of the ferrite lamina (Fig. 7.8). As the velocity of the interface is a function of the inverse of the diffusion distance, the interface would not be flat, but presents instead a double hyperbolic contour. In order to avoid increasing the complexity of the model, an average advance velocity for a flat interface is used.

The average advance velocity can be determined as:

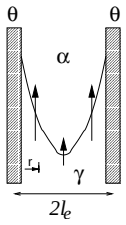

Figure 7.8: Diffusion distances r from cementite to the ferrite austenite interface vary across each *slice* of thickness l_e in the pearlite colony, producing a curved interface. This profile has been integrated and an averaged advance velocity for the equivalent flat interface has been considered instead.

$$\begin{aligned}
\bar{v}^{int} &= \frac{1}{r_f - r_0} \int_{r_0}^{r_f} v^{int}\, dr \\
&= \frac{1}{r_f - r_0} \int_{r_0}^{r_f} \frac{1}{r} D \left(\frac{c^{\gamma\theta} - c^{\gamma\alpha}}{c^{\gamma\alpha} - c^{\alpha\gamma}} \right) dr \\
&= \frac{1}{r_f - r_0} \int_{r_0}^{r_f} \frac{1}{r}\, dr\, D \left(\frac{c^{\gamma\theta} - c^{\gamma\alpha}}{c^{\gamma\alpha} - c^{\alpha\gamma}} \right) \\
&= \frac{1}{r_f - r_0} \left(\ln r_f - \ln r_0 \right) D \left(\frac{c^{\gamma\theta} - c^{\gamma\alpha}}{c^{\gamma\alpha} - c^{\alpha\gamma}} \right) \qquad (7.16)
\end{aligned}$$

where $\bar{v}^{int}$ is the averaged velocity of the interface. r_f and r_0 are the limits of integration, being in this case the distance to the centre of the slice (position that will correspond to the slowest movement of the interface), and the minimum distance from cementite in which we could consider to have steady growth of austenite (in the model, this value has been taken as a few cell parameters in thickness, 10^{-8}m). The other parameters have already been defined in Section 7.3.2. As the slices have a regular thickness, the conversion from area to volume is trivial.

Since many austenite nuclei start to grow, impingement must be taken into account using an extended volume method of Avrami [9, 10, 11]:

$$v_\gamma = 1 - \exp\left(-v_\gamma^e\right) \tag{7.17}$$

where v_γ is the real volume fraction and v_γ^e is the extended one.

7.3.4 Transformation of ferrite

Once all the pearlite has been transformed to austenite, the α/γ interface keeps advancing into the ferrite grains until all the material has been reaustenitised. This interface is considered to be flat. As the diffusion distances become larger, the velocity of the interface v^{int} (equation 7.14), becomes smaller.

Ferrite grains are assumed to be flat plates, with an average thickness of $2\,l_\alpha$, so that there is no need to consider impingement between growing particles.

7.4 Comparison with experimental results

7.4.1 Experimental procedure

A standard set of experiments has been designed in order to compare the predictions of the model with the transformation behaviour of steel. This set of experiments can then be used to compare the capability of the model to predict the effects of other parameters like composition and microstructure. Six experiments have been used, consisting of heating a steel sample into the intercritical range for a short to medium time (Fig 7.9), so that a partial transformation to austenite is expected, and using suitable time and temperature conditions so that the full range of partial transformation is covered, from barely no transformation to almost complete reaction.

Experimental data had been collected using a dilatometer (Thermecmastor Z), using hollow steel samples, following the thermal history described in these six experiments. The

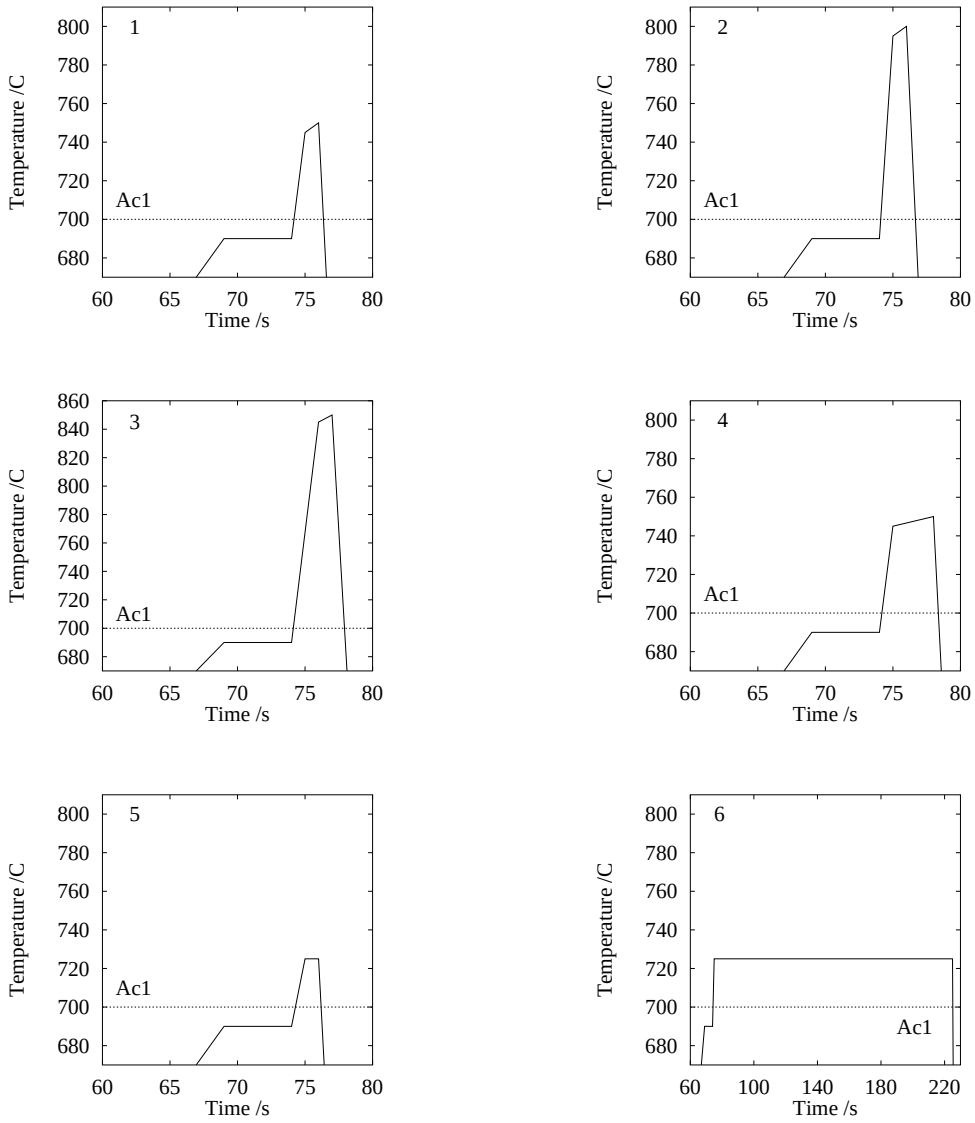

Figure 7.9: Standard experiments used: dilatometric samples were swiftly heated to a temperature below Ac_1, and then brought into the intercritical temperature range for a short period of time, at a heating rate of 50 °C s^{-1}, to achieve various degrees of partial transformation to austenite, and finally quenched with helium jets. Experiments 1, 2, 3 and 5 consider the effect of a short time above Ac_1 reaching different temperatures; experiment 4 considers the effect of an intermediate interval at an intermediate temperature, and finally experiment 6 maintains the sample at a low austenitisation temperature for a very long time, with the aim of reaching the equilibrium volume fraction of transformation. Programmed and actual heat cycles are very close. Differences are listed in table 7.5

samples had a outer diameter of 8 mm, inner diameter of 5 mm and a length of 12 mm. All the experiments were conducted in vacuum. The dilatometric samples were swiftly heated to a temperature below Ac_1, and then brought into the intercritical temperature range for a short period of time, to achieve various degrees of partial transformation to austenite, and finally quenched with helium jets. Due to the fast heating and cooling rates planned, designed to push the limit of the equipment used, some of the samples did not follow precisely the planned thermal cycle. The real thermal history was recorded during the experiments (table 7.5) and that information, together with composition and microstructural description of the samples, was fed into the model and its results compared with experimental data.

The microstructure of both steels used was characterised in terms of the parameters l_α, l_p, l_{col} and l_e, in the way described in Section 7.2.1. l_α and l_{col} were measured from optical micrographies, following Sellars [127]. l_p was determined from the previous information and the carbon content of the steel. l_e was measured using transmission electron microscopy, and stereologically corrected as in [128]. The starting and final microstructures for both steels are shown in figures 7.11 to 7.17.

wt.%	**C**	**Si**	**Mn**	**Cr**	**Ni**	**Mo**	**V**
Steel A	0.55	0.22	0.77	0.20	0.15	0.05	0.001
Steel B	0.54	0.20	0.74	0.20	0.17	0.05	0.001

Table 7.3: Composition of steels used. Both steels present typical compositions used in manufacturing processes involving induction hardening.

A first set of experiments was used to determine the combined value $C_0 N_0 = 1.5 \times 10^{-3} m^{-2}$, where N_0 is the number of nucleation sites per unit area of colony interface, and C_0 is a fitting parameter representing the likelihood of each of those sites to become active. The model was then tested using the standard set of experiments against two steels of different composition, and slightly different microstructure. As shown in figures 7.10, the predictions of the model give an excellent description of the experiments.

	$2l_\alpha \pm \sigma$ /m	$2l_p$ /m	$l_e \pm \sigma$ /m	$l_{col} \pm \sigma$ /m
Steel A	$(2.55 \pm 1.36) \times 10^{-6}$	6.38×10^{-6}	$(0.51 \pm 0.05) \times 10^{-6}$	$(19.73 \pm 0.95) \times 10^{-6}$
Steel B	$(1.85 \pm 0.97) \times 10^{-6}$	4.34×10^{-6}	$(0.25 \pm 0.05) \times 10^{-6}$	$(18.46 \pm 0.95) \times 10^{-6}$

Table 7.4: Microstructure of steels used, characterised in terms of the parameters l_α, l_p, l_{col} and l_e, as defined previously. l_α and l_{col} were measured from optical micrographies. l_p was determined from the previous information and the carbon content of the steel. l_e was measured using transmission electron microscopy and stereologically corrected. σ represents the standard deviation of the measurement.

Experiment	**Temp. reached / °C**	**Time above** Ac_1 / s
1	746	2.4
2	773	2.7
3	812	3.9
4	750	4.5
5	725	1.5
6	725	151

Table 7.5: The brief nature of the experiments designed to test the model imply that in some cases the equipment used was not able to follow precisely the thermal cycles desired. The precise temperature reached in each case, and the time that the sample spent above Ac_1 was measured and is summarised above.

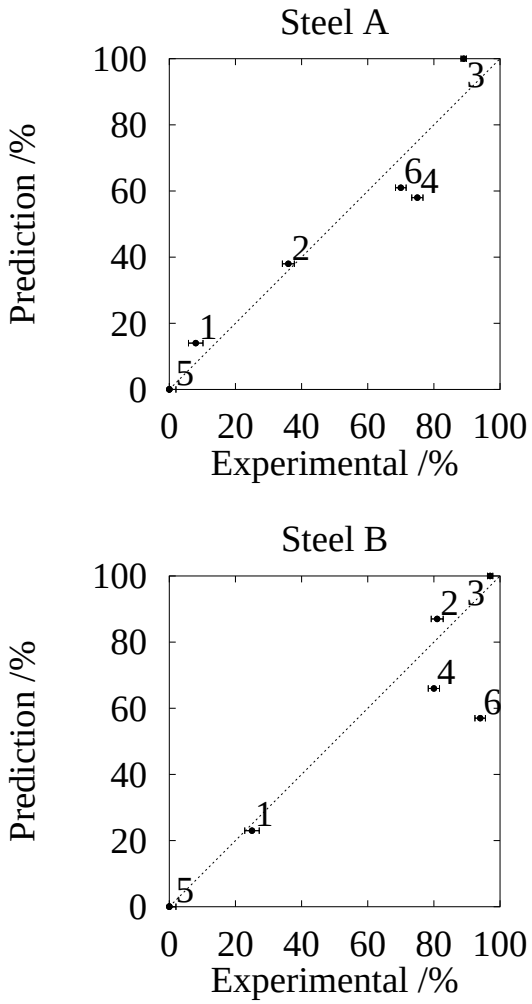

Figure 7.10: Prediction of volume fraction of austenite *vs*. experimental results for both the steels used. Numbers in each plot refer to experiment number. Error bars correspond to 1 standard deviation in the measurement of the volume fraction.

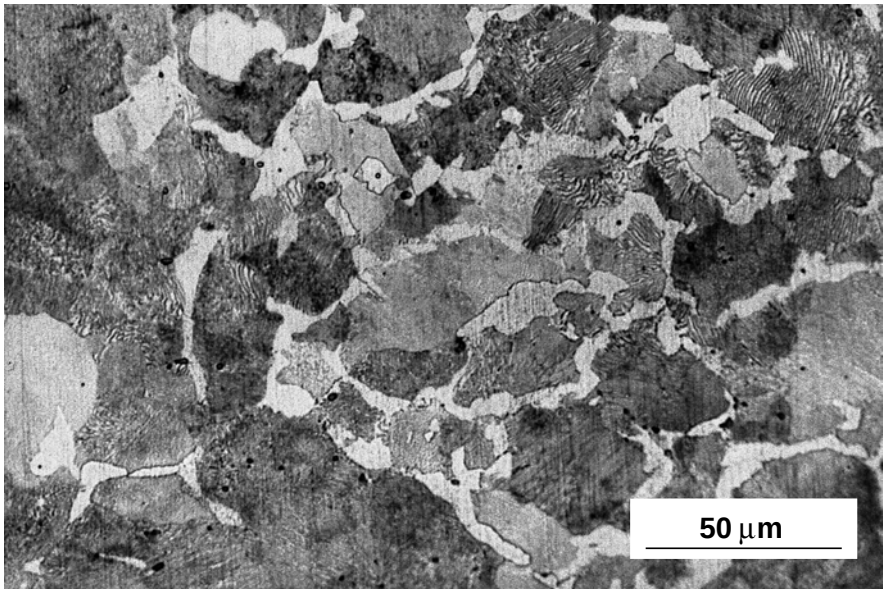

(a) Starting microstructure of steel A

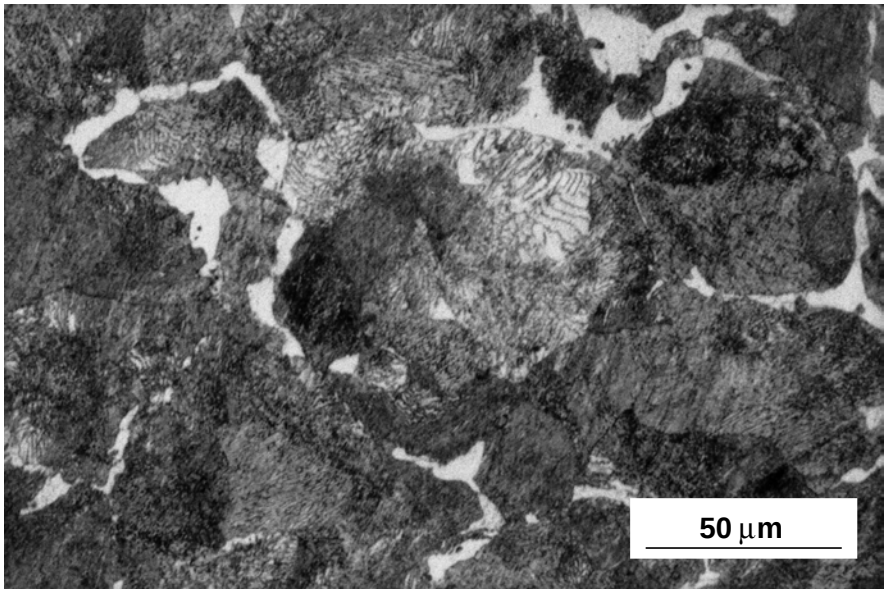

(b) Starting microstructure of steel B

Figure 7.11: Microstructures of steels A and B before austenitisation experiments

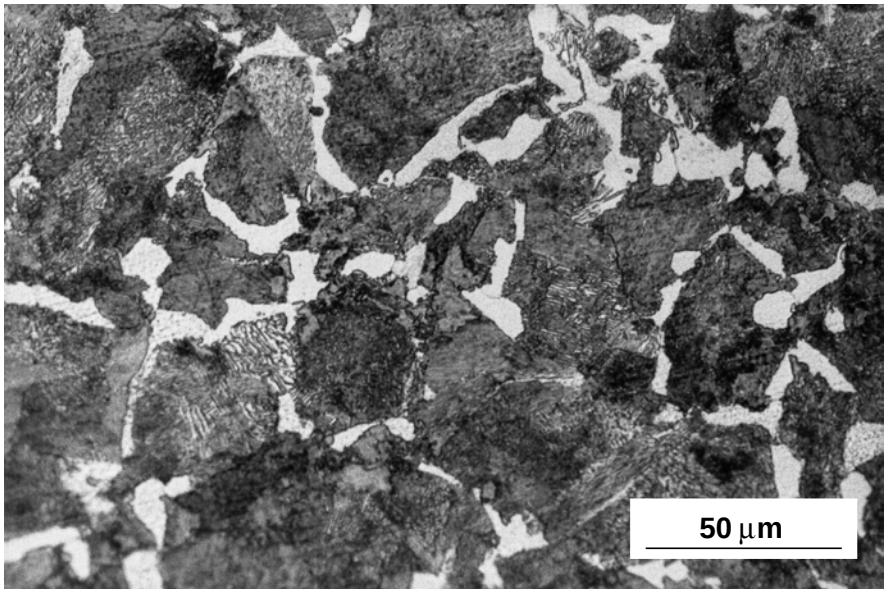

(a) Microstructure of steel A after experiment 1.

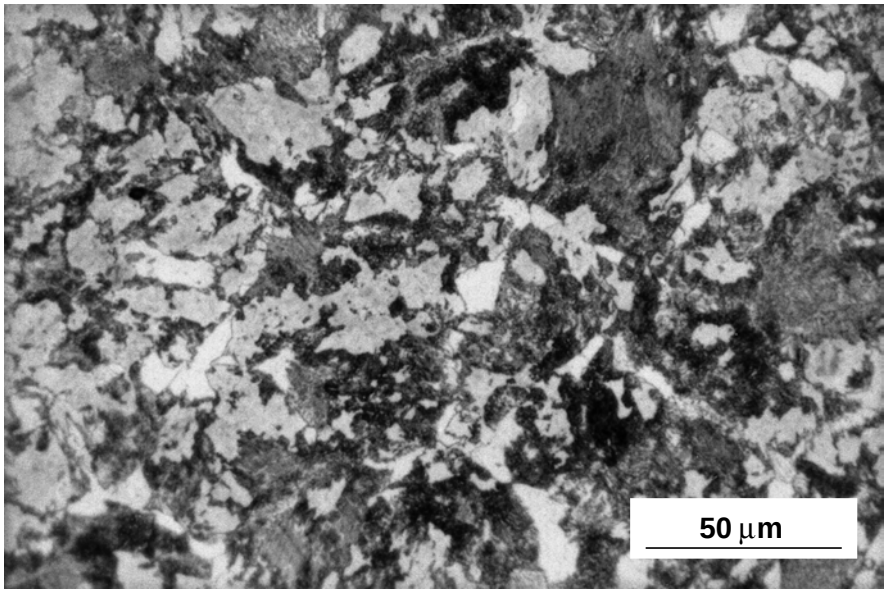

(b) Microstructure of steel B after experiment 1.

Figure 7.12: Effect of experiment 1 on steels A and B.

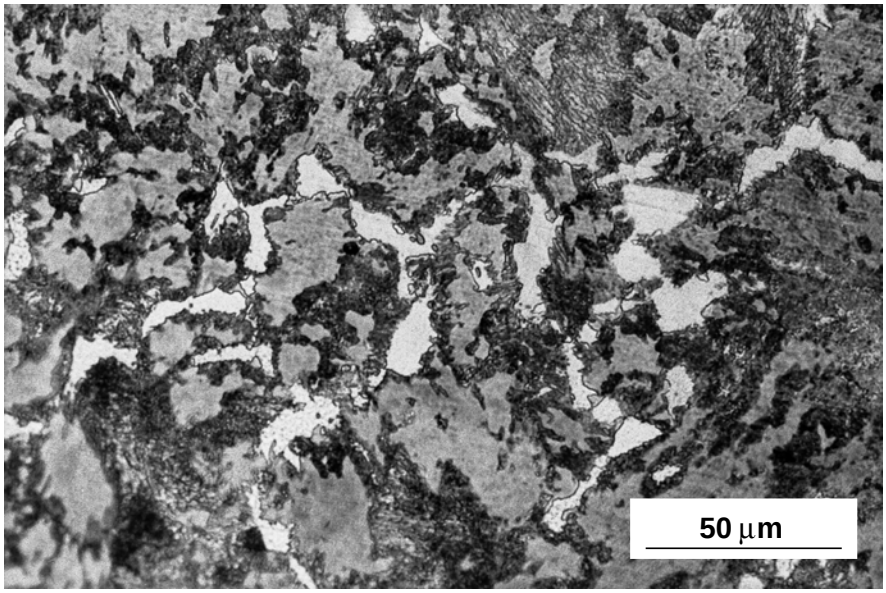

(a) Microstructure of steel A after experiment 2.

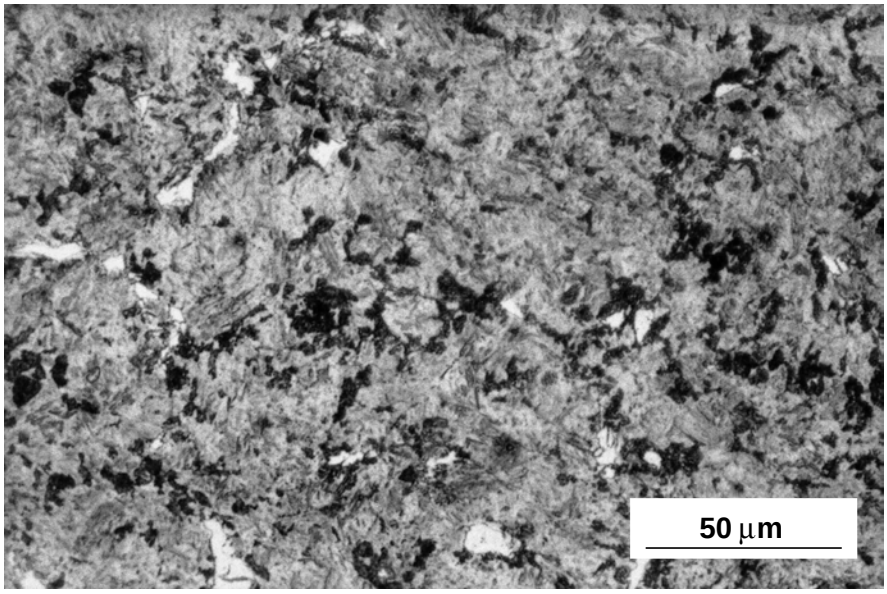

(b) Microstructure of steel B after experiment 2.

Figure 7.13: Effect of experiment 2 on steels A and B.

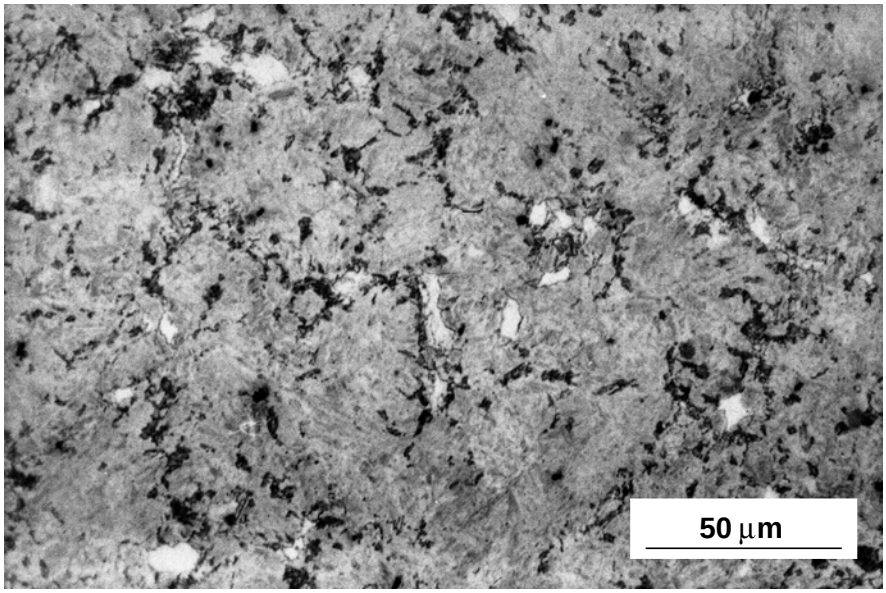

(a) Microstructure of steel A after experiment 3.

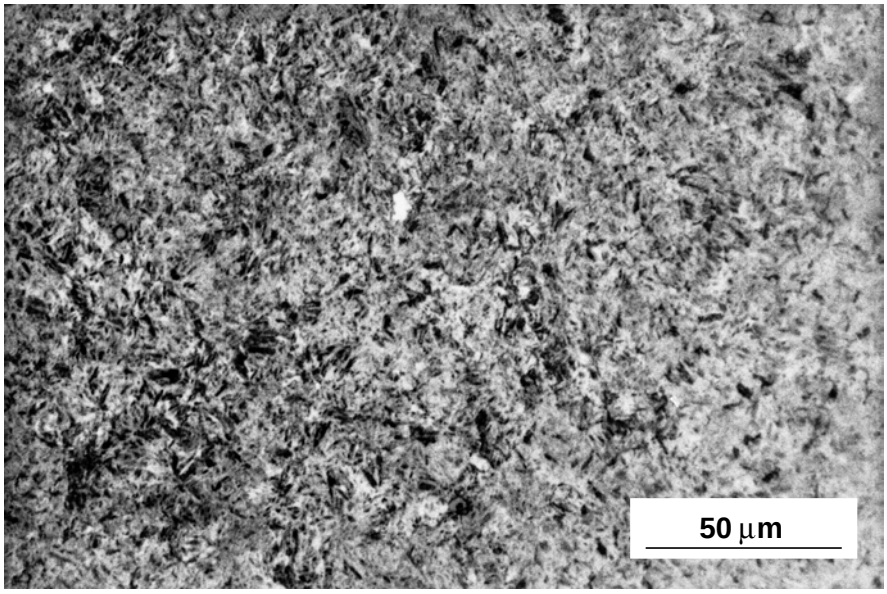

(b) Microstructure of steel B after experiment 3.

Figure 7.14: Effect of experiment 3 on steels A and B.

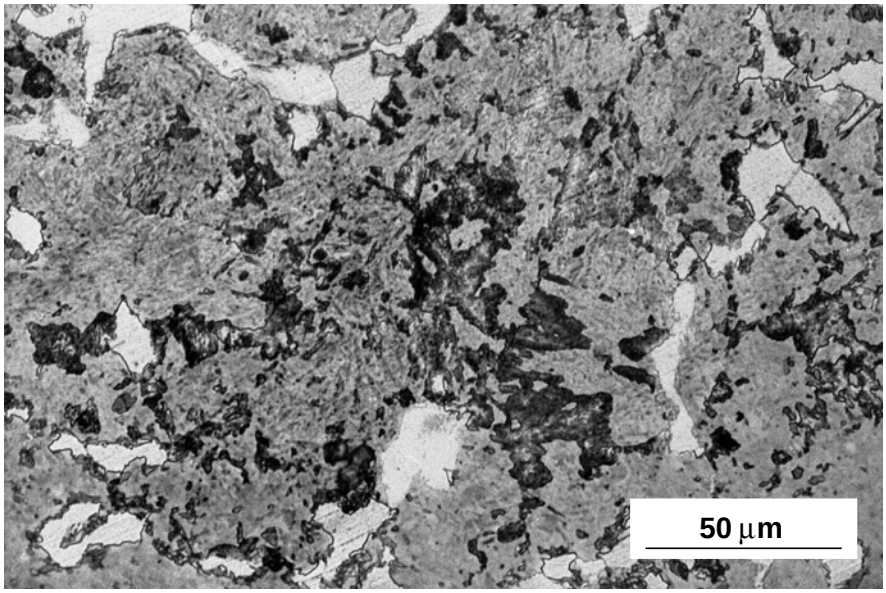

(a) Microstructure of steel A after experiment 4.

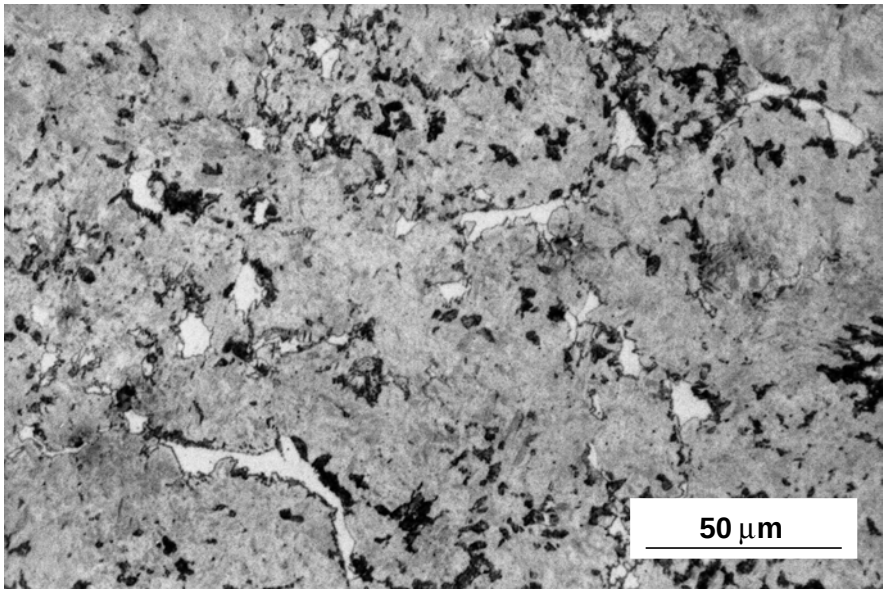

(b) Microstructure of steel B after experiment 4.

Figure 7.15: Effect of experiment 4 on steels A and B.

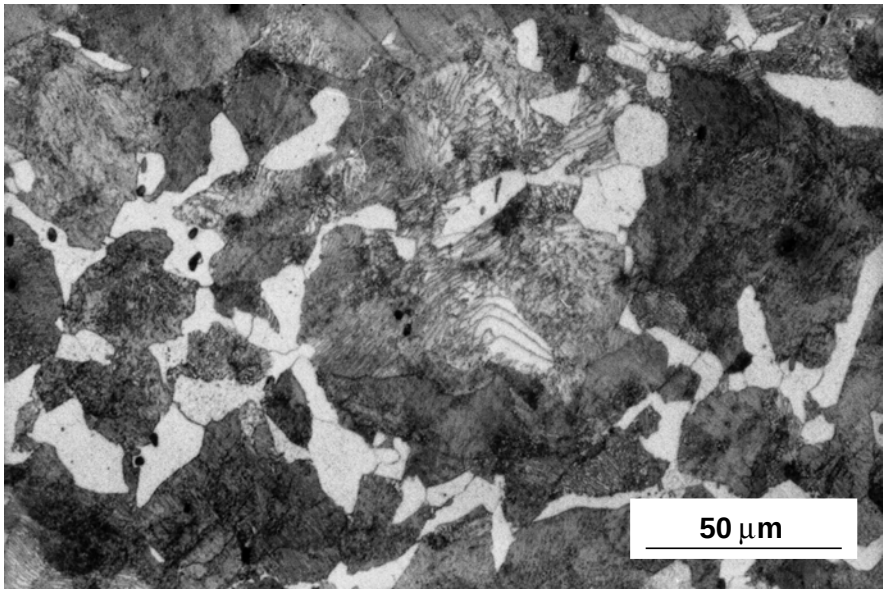

(a) Microstructure of steel A after experiment 5.

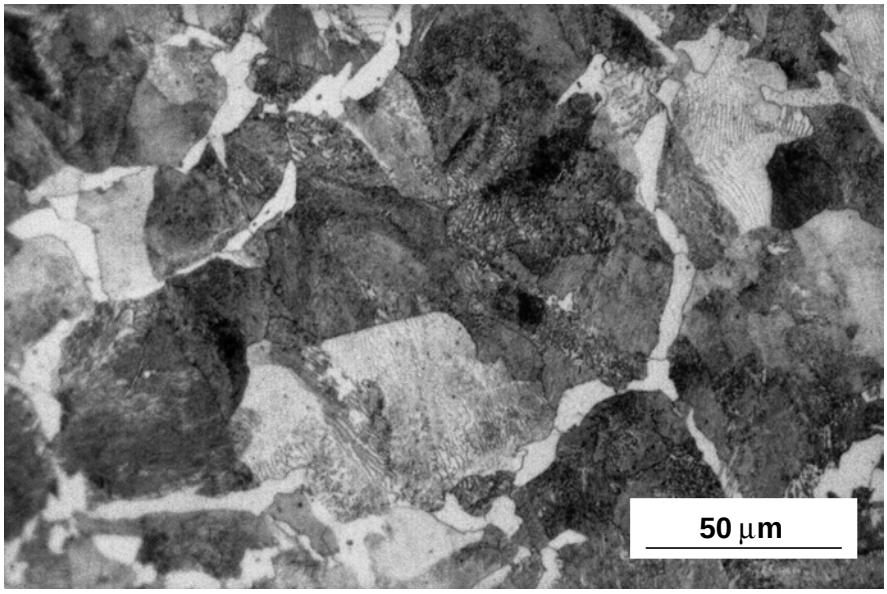

(b) Microstructure of steel B after experiment 5.

Figure 7.16: Effect of experiment 5 on steels A and B.

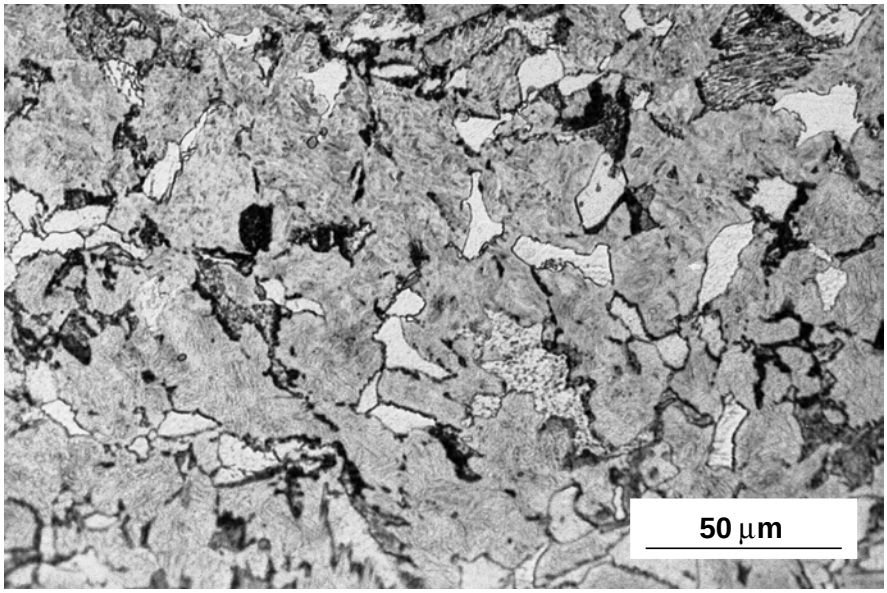

(a) Microstructure of steel A after experiment 6.

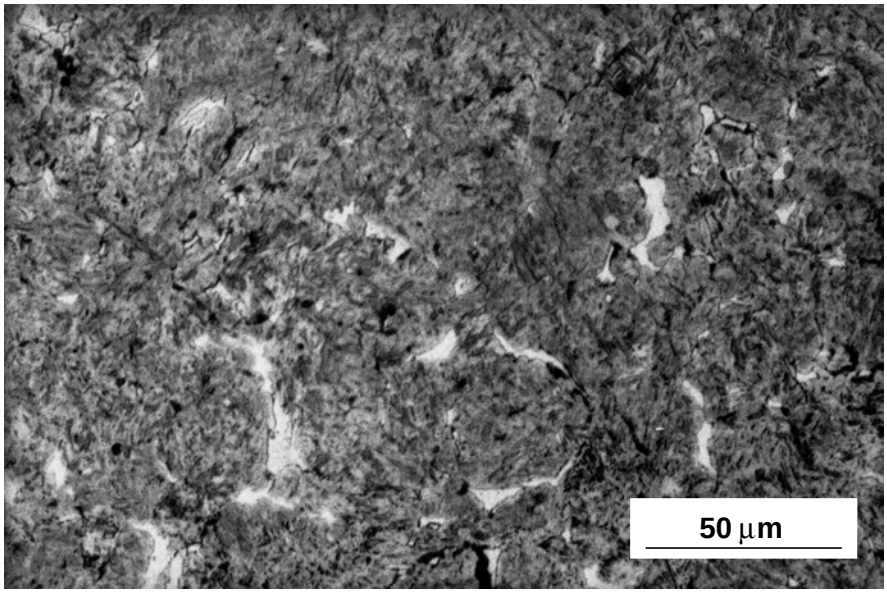

(b) Microstructure of steel B after experiment 6.

Figure 7.17: Effect of experiment 6 on steels A and B.

7.5 Applications

The model presented here can be used in a variety of applications, including the calculation of CHT (continuous heating transformation) diagrams for any hypoeutectoid steel, taking into account its composition and microstructure, as the one in Figure 7.20, calculated for steel B, or the final distribution of phases after a reaustenitisation heat treatment.

The CHT diagram shown in Figure 7.20 was determined by feeding the model with 8 different constant heating rates (0.1, 0.3, 1, 3, 10, 30, 100, and 300 °C s^{-1}) and the composition and microstructure of steel B.

The effect of small variations in composition and starting microstructure can also be studied in detail using this model. Experimental study of these factors is usually unpractical because of the impossibility to resolve the effect of different factors, without changing others simultaneously. A clear example of the substantial effect that compositional changes can have in the transformation behaviour is shown in figure 7.13.

The effect of pearlite spacing on the transformation behaviour of steel during austenitisation can be studied, leaving all other parameters unchanged. A steel of the same composition and microstructure as steel B has been considered. Two different values of pearlite spacing have been considered, $l_e = 0.125$ μm and $l_e = 2.0$ μm, and two heating rates 10 and 100 °C s^{-1}.

Results of these calculations are shown in Fig. 7.19. It can be seen how the transformation process starts at the same time for both microstructures, and even the transformation becomes complete at approximately the same time, but the evolution of the dissolution of pearlite follows a substantially different rate. In a finer pearlite transformation happens at a much faster rate, undoubtedly due to the shorter carbon diffusion distances.

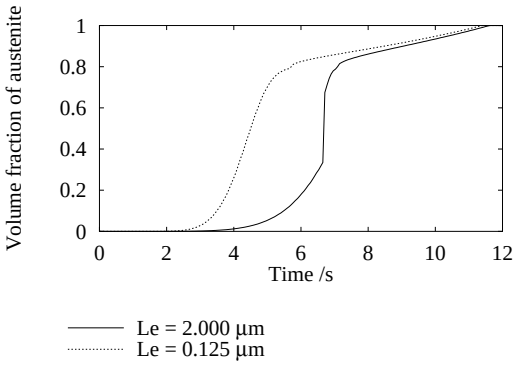

Figure 7.18: Austenitisation of steel B at a heating rate 10 $°Cs^{-1}$ and considering two different pearlite spacings.

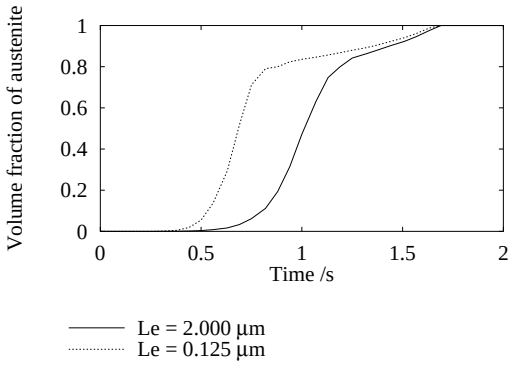

Figure 7.19: Austenitisation of steel B at a heating rate 100 $°Cs^{-1}$ and considering two different pearlite spacings.

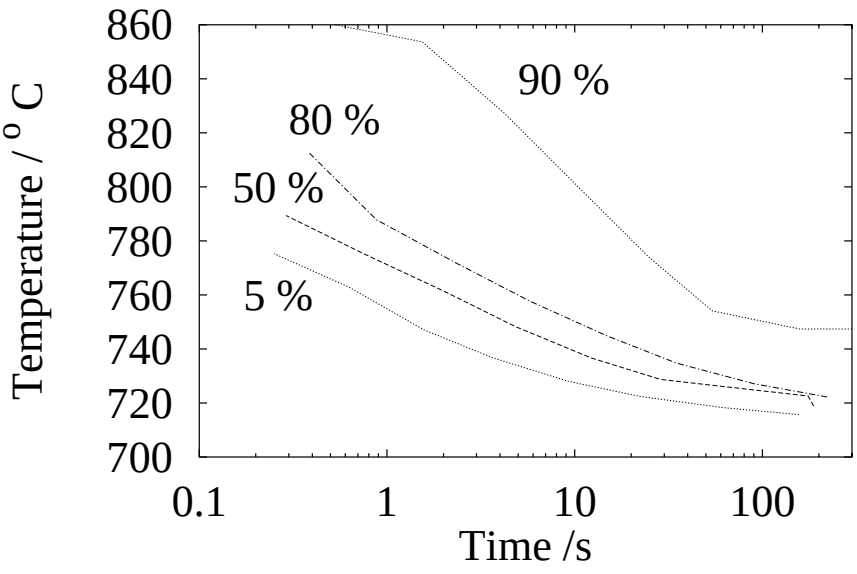

Figure 7.20: Continuous heating transformation diagram for steel B. To determine this diagram the model was fed with the composition and microstructural characteristics of steel B, and 8 different constant heating rates (0.1, 0.3, 1, 3, 10, 30, 100 and 300 °C s^{-1}). The diagram was then plotted using the transformation behaviour predicted.

7.6 Conclusions

A physical model describing the reaustenitisation of hypoeutectoid steel has been presented. The work can be used to determine the effects of parameters such as microstructure (grain size, pearlite spacing), composition and heating rate on the formation of austenite. It is possible to generate continuous heating transformation diagrams for specific steels, which may be of use in research, as well as in industry.

Chapter 8

Effect of deformation on austenitisation

8.1 Introduction

Common steel manufacturing processes involve several stages of hot or warm deformation, followed by cold sizing to bring the component to the final dimensions, and subsequent hardening and tempering heat treatments.

One of the main side effects of deformation in metals is the accumulation of residual stresses which can cause shape distortion when the component is annealed. Virtually all final shaping operations introduce some residual stresses [139]. Accurate modelling of the stresses and corresponding distortions is important in many engineering industries.

There is another consequence of deformation that often is overlooked. The energy and the structures of defects that deformation introduces in steel can change its phase transformation behaviour. Indeed, as most mechanical and structural components require a carefully designed microstructure for optimum mechanical properties, accounting for changes in the phase transformation behaviour can become of supreme importance.

Deformation at high temperatures produces a clear acceleration of the kinetics of transformation of austenite to its diverse ferritic transformation products [74]. Stored energy in the parent phase, an increased number density of nucleation sites, increased grain surface per unit volume, and serrated grain boundaries, are some of the factors that contribute to this enhanced transformation rate [74].

A model describing the austenitisation of a mixed microstructure of pearlite and ferrite was described in Chapter 7. That model does not include the effect of deformation prior to austenitisation. The aim of the work presented here was to see whether deformation accelerates austenitisation in a manner similar to all reconstructive transformations. As will be seen, the actual affects are quite complex functions of strain and the heating rate.

8.2 Experimental procedure

8.2.1 Sample material

The composition of the material used in this study is shown in Table 8.1 for the sake of completeness. The alloy used in the work presented in this Chapter is Steel B (Chapter 7). Bars of the alloy were deformed by swaging to a final diameter of 8 mm. The initial diameters were chosen to produce a range of final deformation levels. The calculation of strain assumes constant volume during homogeneous plastic deformation. The strain is given by [140]

$$\varepsilon = \ln \frac{l_f}{l_0} = \ln \frac{D_0^2}{D_f^2} \tag{8.1}$$

where ε is the true strain, l_0 and l_f are the lengths of the steel bar before and after the swaging process respectively, and D_0 and D_f are the corresponding diameters. The strains achieved are listed in Table 8.2. Dilatometric samples were made of the swagged bars. The samples are hollow cylinders which have an outer diameter of 8 mm, and inner diameter of 5 mm with a length of 12 mm. Up to four different levels of deformation have been studied, including undeformed material.

wt.%	**C**	**Si**	**Mn**	**Cr**	**Ni**	**Mo**
Steel B	0.54	0.2	0.74	0.20	0.17	0.05

Table 8.1: Chemical composition of steel used.

8.2.2 Dilatometric tests

Dilatometric tests were done using a Thermecmastor Z simulator, manufactured by Fuji Electronic Industrial Co. Ltd. All the experiments were done in vacuum ($\approx 10^{-2}$ Pa)

Sample	D_0 /mm	D_f /mm	$-\varepsilon$
UDF	8.0	8.0	0.0
DFN	10.0	8.0	0.45
DFD	12.5	8.0	0.89
DFX	15.0	8.0	1.26

Table 8.2: Samples with four levels of strain have been considered, including undeformed material.

to prevent oxidation. The specimens are heated in this equipment using a high frequency induction coil. Cooling can be induced by gas (He or N_2) or by water quenching. He is used in practice because of its high heat capacity. Temperature was measured using a platinum / platinum-10% rhodium thermocouple, with an accuracy of $\pm$ 3°C. The variation in temperature along the specimen length is less than $\pm$ 10°C [141]. The radial dilatation of the specimen is measured using a He-Ne laser beam that continuously scans the surface of the specimen at mid-length, measuring its diameter with a precision of $\pm$ 1 μm [141]. Data concerning temperature cycle and dilatation are registered on a computer for later analysis. Heating rates from 0.1°C s^{-1} to 50°C s^{-1} have been used.

Dilatometry is used to monitor the progress of phase transformations. Phases with different crystalline lattices have different thermal expansion coefficients. The expansion coefficient of a given phase is usually constant. Therefore a plot of dilatation against temperature during heating at a constant rate, for instance, gives a straight line. The slope of the line will be different for each phase, and therefore, deviations from the straight line indicate some phase transformation. Figure 8.1 shows an example of a typical dilatometric curve in which the start and finish of the transformation from ferrite/cementite to austenite have been highlighted. For this purpose, the actual value of dilatation is not relevant, and only its variation should be taken into account.

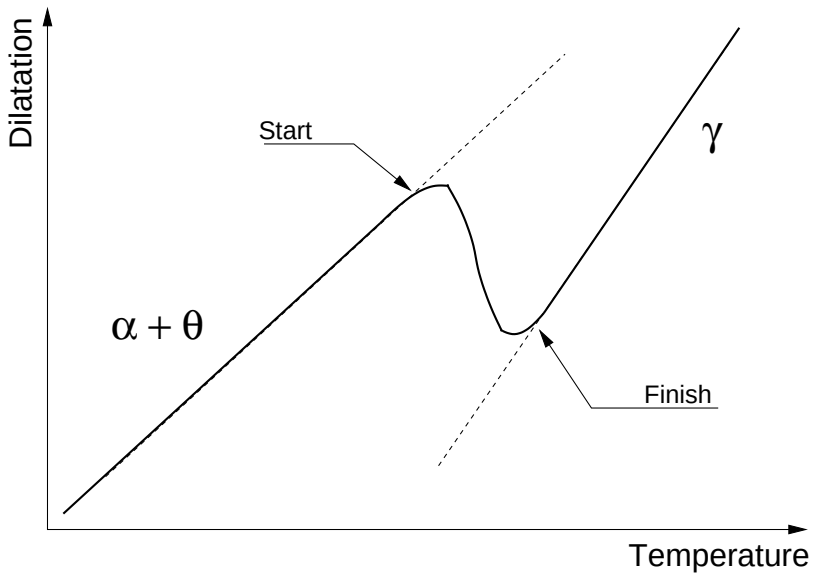

Figure 8.1: Schematic dilatometric curve showing the start and finish of transformation from ferrite and cementite ($\alpha + \theta$) to austenite (γ) during constant heating.

8.2.3 Microscopy and chemical analysis

Samples for scanning electron microscopy (SEM) were mounted in conductive Bakelite, ground on SiC paper to 1200 grit and polished with cloth soaked with 1 μm diamond paste. The samples were etched with 2% nital (2% concentrated nitric acid in methanol). A JEOL JSM-820 scanning electron microscope was used for medium to high magnification imaging using secondary electrons at 20 kV. Chemical analysis was done in a JEOL JSM 5800LV equipped with energy dispersive X-ray spectroscope (EDS) at 15 kV.

8.3 Results and discussion

8.3.1 Effect of deformation on austenitisation

Deformation of the parent phase tends to accelerate the rate of reconstructive transformation. Nucleation and growth rates of austenite are increased by deformation [77].

Figure 8.2 shows the dilatometric curves measured during the transformation from ferrite/pearlite to austenite whilst heating at 0.1°C s^{-1}, as a function of prior strain. The data were generated by raising the temperature to 700°C at a rate of 10°C s^{-1}, to avoid tempering effects, followed by heating at a reduced rate of 0.1°C s^{-1} until 800°C was reached. Transformation in the pre-deformed specimen proceeds at a faster rate, and is completed in a shorter time relative to the undeformed specimen.

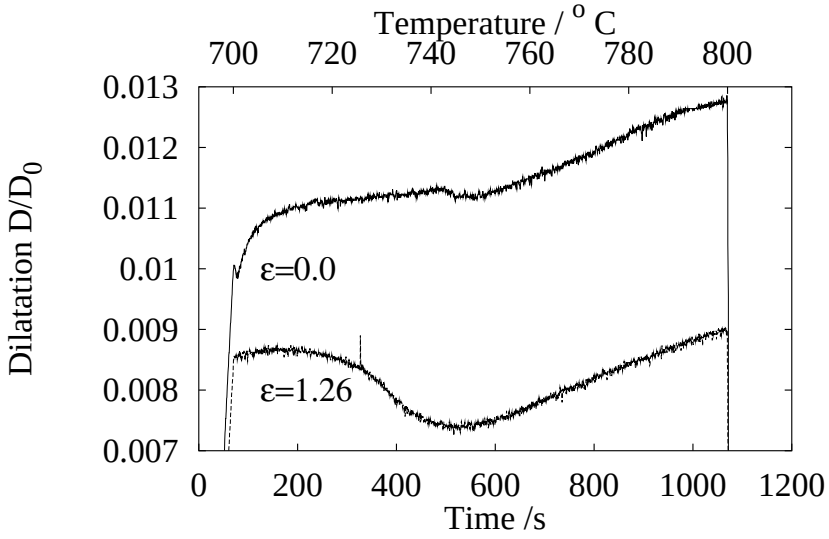

Figure 8.2: Comparison between the dilatometric curves registered during the transformation to austenite (heating rate of 0.1°C s^{-1}), for two levels of prior deformation.

Comparisons of transformation at different heating rates (0.1, 1 and 50°C s^{-1}) for three different deformation levels (ϵ=0.0, 0.45 and 1.26) are presented in figures 8.3–8.5. For each heating rate, an increase in the level of deformation leads to a decrease in the

transformation temperature.

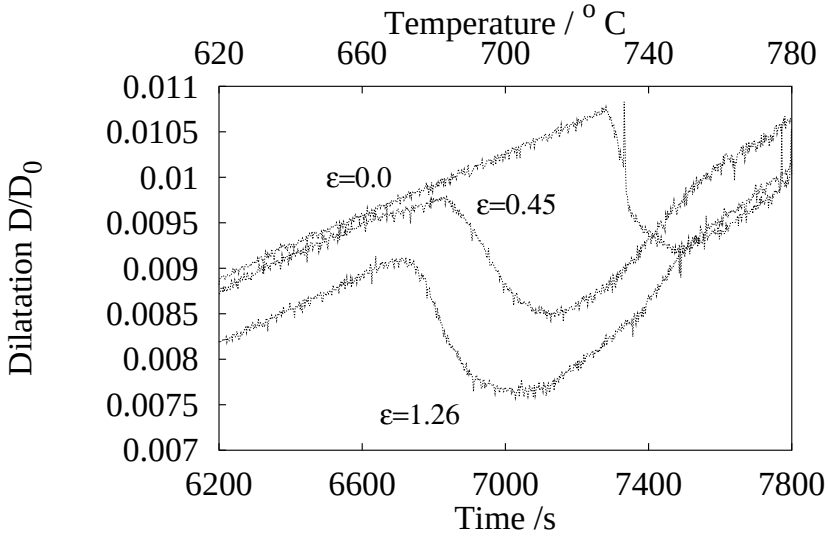

Figure 8.3: Comparison between the dilatometric curves registered during the transformation to austenite during a slow heating experiment (heating rate of $0.1°C\ s^{-1}$), for three different levels of deformation, $\varepsilon = 0.0$, $\varepsilon = 0.45$ and $\varepsilon = 1.26$.

8.3.2 Effect of deformation on spheroidisation

The reduction of transformation temperature is not the only effect of deformation on the austenitisation of a hypoeutectoid steel. Deformation also influences the overall kinetics of austenitisation. The original microstructure consists of ferrite and fine pearlite. In the right circumstances, for example during slow heating, this initial microstructure can undergo changes before the austenite begins to form. Such changes can be accelerated when the sample is deformed before heating. One of the possible changes involves the spheroidisation of the lamellar cementite. It is expected that spheroidisation is more rapid in deformed alloys [86, 85]. The extent of spheroidisation is in turn likely to influence the subsequent formation of austenite. Therefore short heat treatments close to the critical austenite formation temperature or even a slow heating rate can modify the starting microstructure [90, 87]. Consequently, a series of experiments was conducted to study the

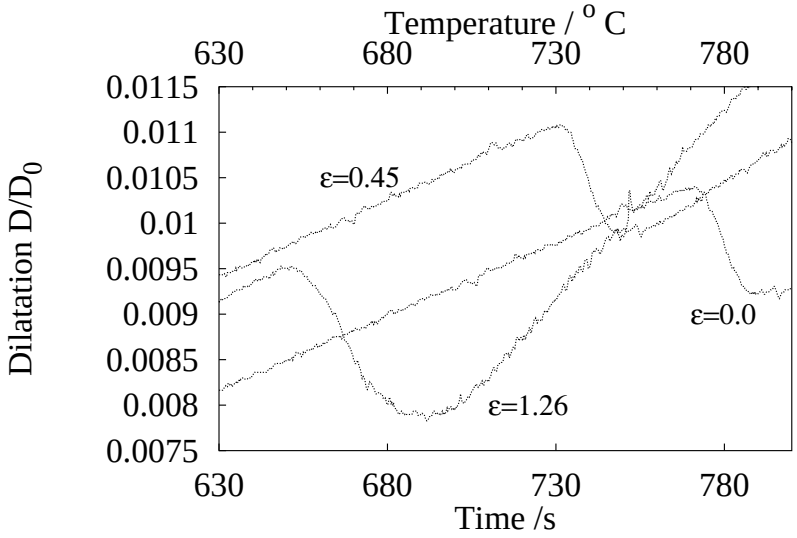

Figure 8.4: Comparison between the dilatometric curves registered during the transformation to austenite during a medium rate heating experiment (heating rate $1°C\ s^{-1}$), for three different levels of deformation, $\varepsilon = 0.0$, $\varepsilon = 0.45$ and $\varepsilon = 1.26$.

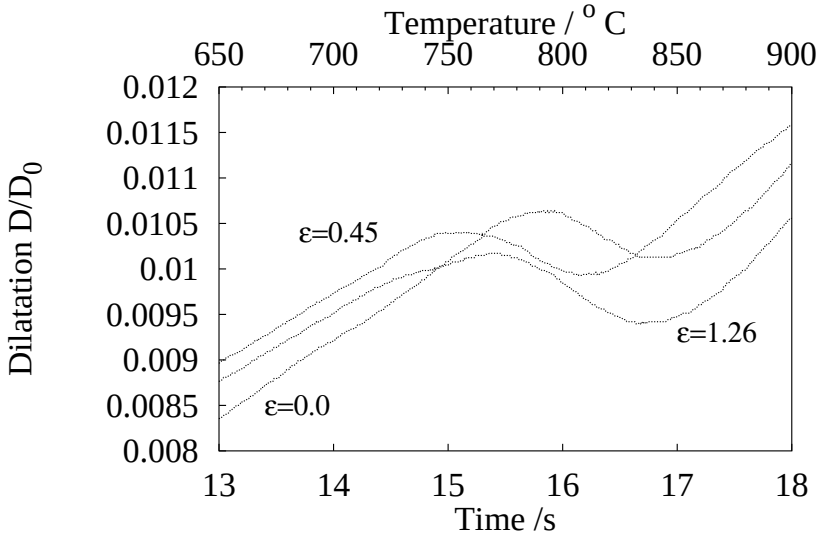

Figure 8.5: Comparison between the dilatometric curves registered during the transformation to austenite during a fast heating experiment (heating rate $50°C\ s^{-1}$), for three different levels of deformation, $\varepsilon = 0.0$, $\varepsilon = 0.45$ and $\varepsilon = 1.26$.

effects of slow heating and prior deformation on spheroidisation and austenite formation.

8.3.2.1 Annealing

Two samples, one undeformed and one severely deformed ($\varepsilon = 1.26$) were heated at 1°C s^{-1}, annealed at 600°C for 30 minutes and quenched. The resulting microstructures are shown in Figures 8.6 and 8.7. A comparison of the undeformed and annealed sample with the as-received state shows no perceptible difference between their microstructures, which consist of lamellar pearlite and ferrite. The sample of deformed and annealed steel is, on the other hand, in an advanced state of cementite spheroidisation.

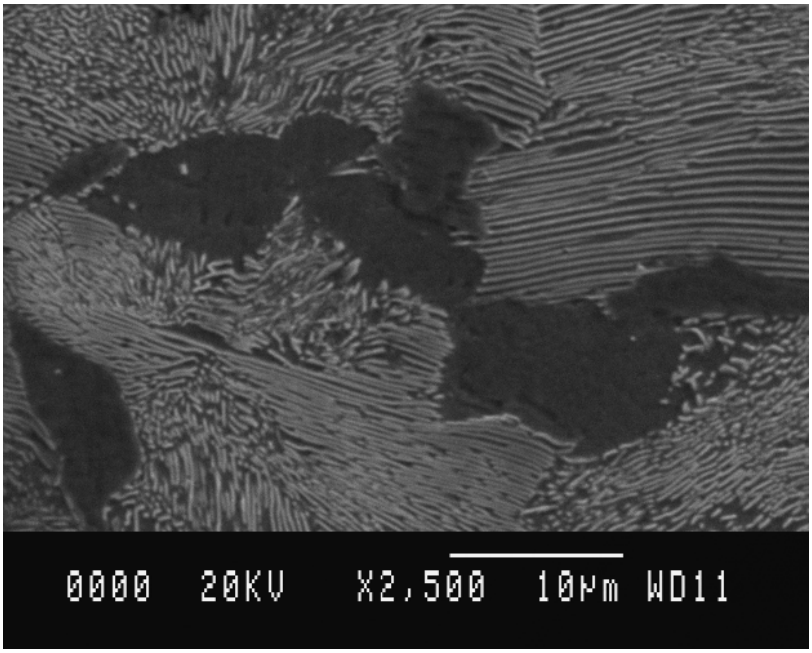

Figure 8.6: Microstructure of an undeformed sample annealed for 30 minutes at 600°C, showing negligible change relative to the as-received microstructure.

8.3.2.2 Slow heating rates

Three more samples were studied to compare the effect of slow heating rates on the evolution of microstructure following deformation. The specimens were heated at 0.1 and 10°C s^{-1} to 680°C followed by a quench to ambient temperature. Figure 8.8 shows

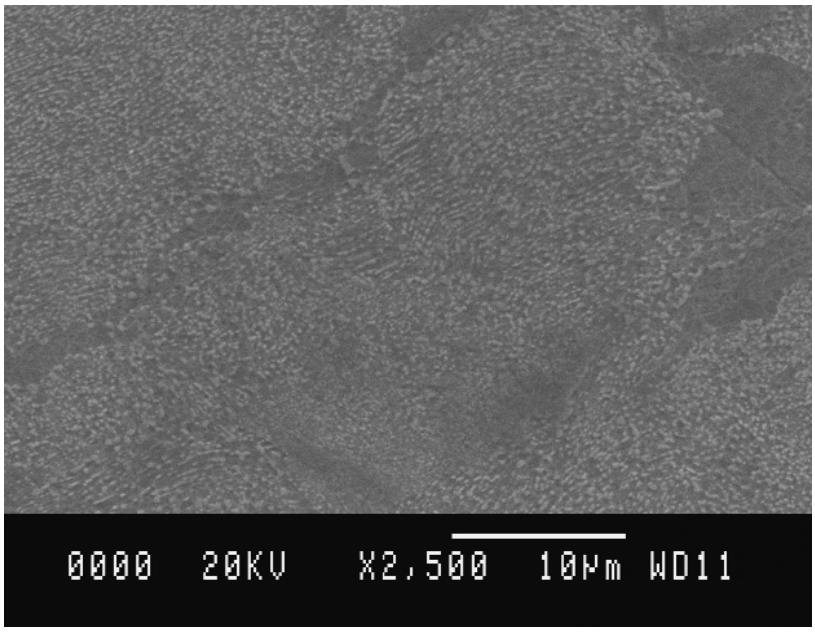

Figure 8.7: Microstructure of a deformed ($\varepsilon = 1.26$) sample annealed for 30 minutes at 600°C, showing the spheroidisation of cementite in pearlite.

the microstructure of a deformed ($\varepsilon = 1.26$) sample heated at 0.1°C s^{-1}. It is evident that there is extensive spheroidisation. Figure 8.9 shows the microstructure of another deformed ($\varepsilon = 1.26$) sample heated this time at 10°C s^{-1}, with only mild spheroidisation. Finally, an undeformed sample was heated at the fast heating rate; Figure 8.10 shows that the original microstructure is essentially retained.

These examples show that at slow heating rates, and especially when the initial microstructure has been deformed, subsequent changes occur which may influence the development of austenite. This latter aspect is examined in section 8.3.4.

8.3.3 Effect of heating rate

The curve describing the kinetics of transformation to austenite has an increasing slope with increasing heating rate. In contrast with what happens when austenite transforms during cooling, both the driving force and diffusivity increase during austenitisation [44,

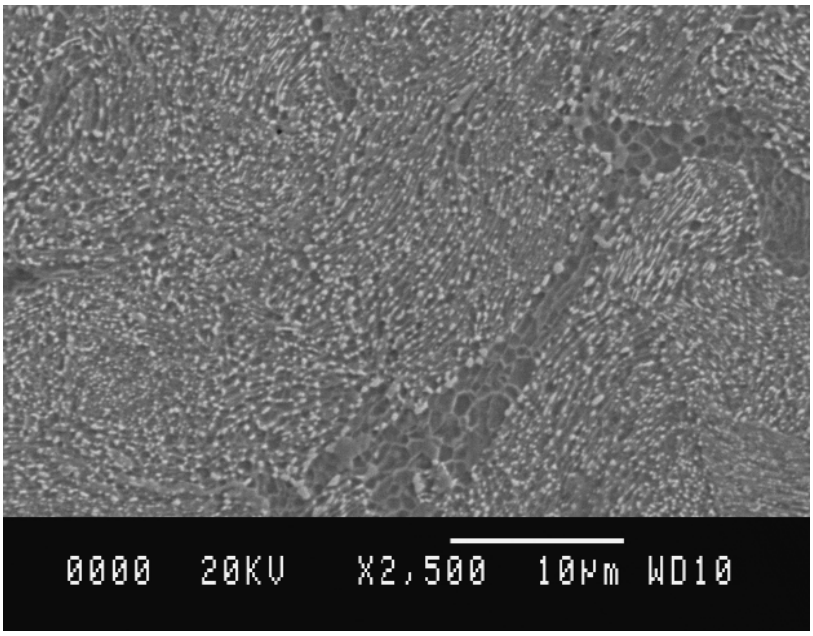

Figure 8.8: Microstructure of a deformed ($\varepsilon = 1.26$) sample heated at a slow heating rate ($0.1°C\ s^{-1}$) showing the spheroidisation of cementite in pearlite.

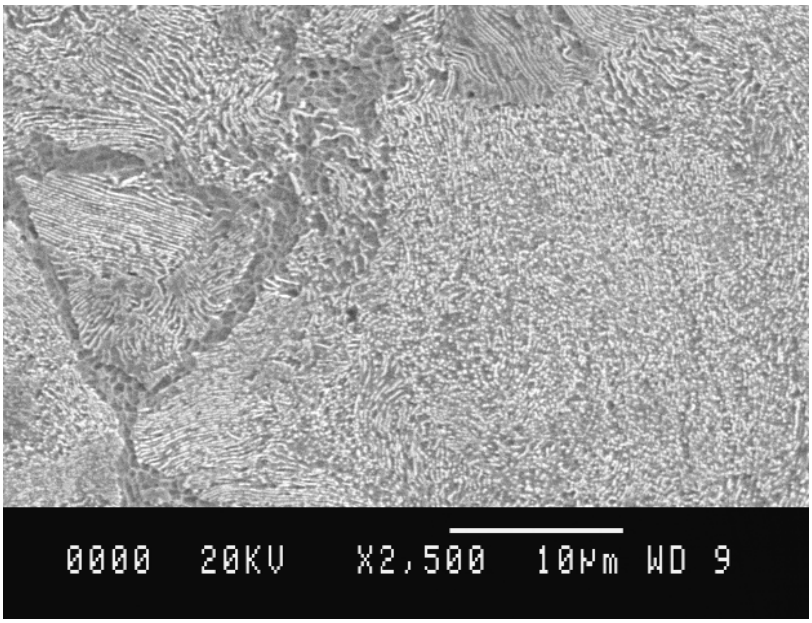

Figure 8.9: Microstructure of a deformed ($\varepsilon = 1.26$) sample heated at a fast heating rate ($10°C\ s^{-1}$) showing the partial spheroidisation of cementite in pearlite.

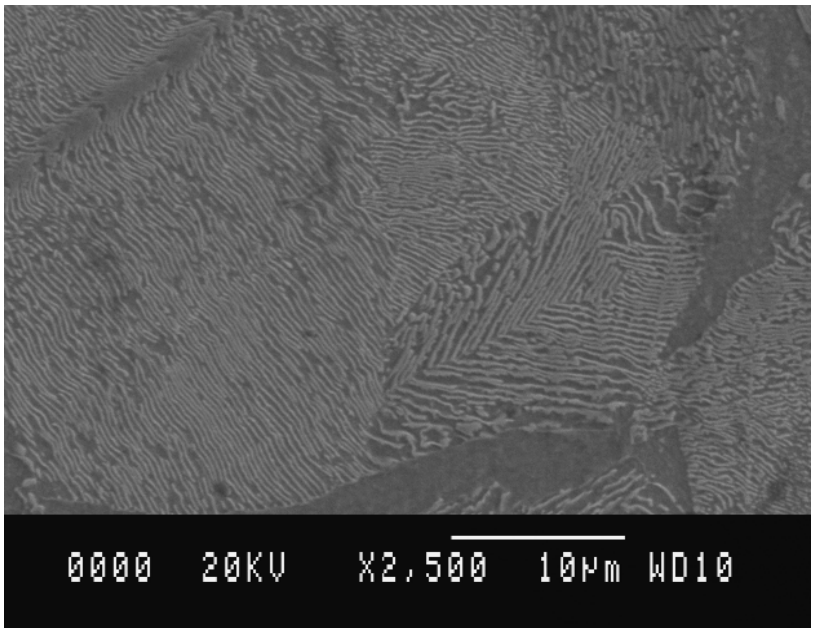

Figure 8.10: Microstructure of an undeformed sample heated at a fast heating rate ($10°C\ s^{-1}$) showing the absence of spheroidisation of cementite.

45, 53]. On the other hand, even with an increasing heating rate, austenitisation still needs some finite time to nucleate and grow so the degree of superheating increases with heating rate as shown in Figure 8.11 [45]. This trend is seen at high heating rates in Figures 8.17 and 8.19.

8.3.4 Effect of microstructure

The microstructure of an alloy influences the kinetics of transformation in several ways. Variations in the morphology and number density of cementite must influence the nucleation and growth of austenite. In pearlite colonies, austenite tends to nucleate at the ferrite/cementite interface on the edges of the colonies [46, 47]. In ferrite/spheroidised cementite, nucleation occurs preferentially at the ferrite/cementite interfaces that lay at ferrite/ferrite grain boundaries [46], which represents a reduction of suitable potential sites when compared with pearlite colony boundaries. The coarseness of the microstructure also defines the mean diffusion path for the atoms involved in reconstructive transforma-

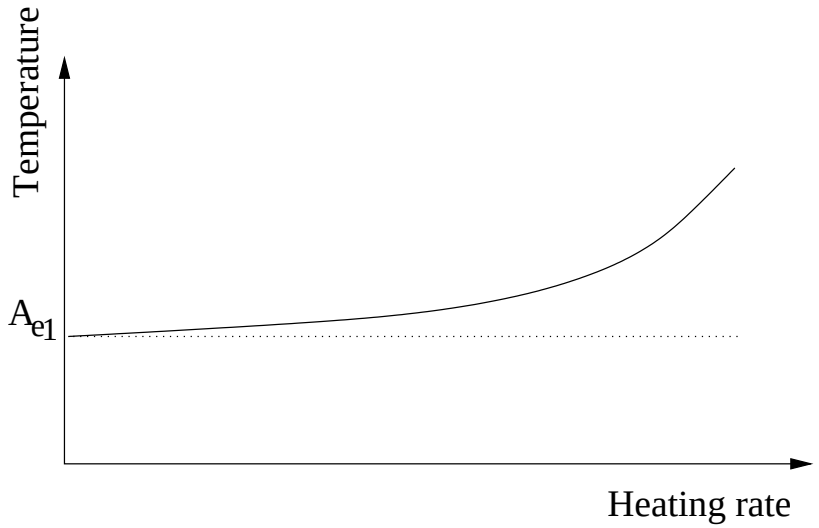

Figure 8.11: Schematic plot of the effect of heating rate on the temperature of start of austenitisation.

tions [44], and must therefore influence the transformation rate. The morphology of the phases involved partially defines their relative stability, via the ratio of surface energy to volume. Some phases may not have their equilibrium chemical compositions, which reduces their stability. The rate of transformation to austenite is influenced by the prior microstructure, including any of the aspects discussed above. The present section of the thesis illustrates some of these effects by comparison of an ideal lamellar pearlite structure with the ideal mixture of ferrite and spheroidised cementite.

8.3.4.1 Boundary surface area

Pearlite presents a larger ferrite/cementite surface area than is present in an equivalent mixture of ferrite and spheroidised cementite, for the same volume fraction of cementite. Assuming that ferrite and cementite have almost the same density, and that the carbon content in weight % of ferrite, cementite and eutectoid pearlite is, respectively 0.02, 6.72 and 0.77, the ratio of ferrite to cementite thicknesses can be determined as (Figure 8.13):

$$d_\alpha = 7.9 d_\theta \tag{8.2}$$

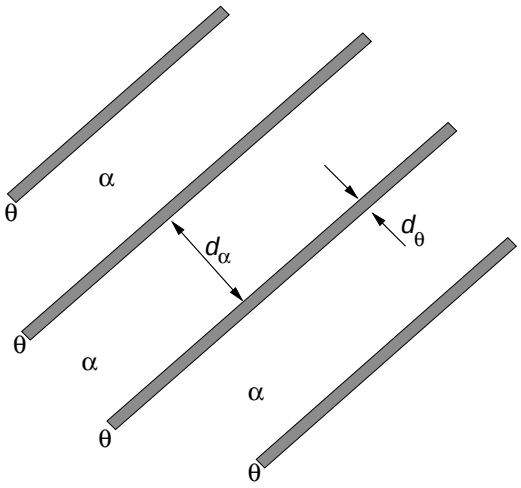

Figure 8.12: Relative thickness of ferrite and cementite lamellae in eutectoid pearlite. α represents ferrite, of thickness d_α and θ represents cementite, of thickness d_θ.

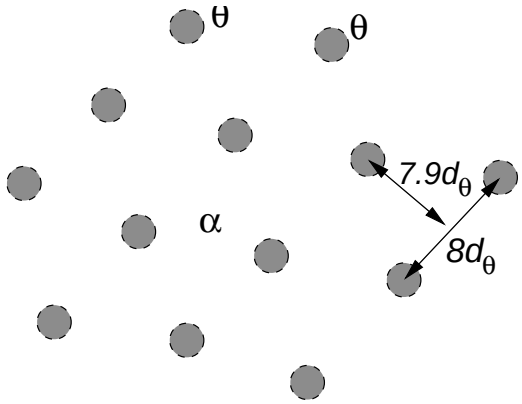

Figure 8.13: Microstructure formed after spheroidisation, containing the same volume fraction of cementite. α represents ferrite, θ represents cementite and r_θ is the radius of the cementite spheroids.

Annealing of pearlite produces spheroidisation of the cementite lamellae. Spheroids are formed by the growth of channels that divide the lamellae in platelets presenting an aspect ratio 8:1 [84, 86]. Such platelets spheroidise and eventually coarsen (Figure 8.13). The spheroids have the radius:

$$r_\theta = 1.7 d_\theta \tag{8.3}$$

A rough calculation of ratio of interface surface area between pearlite and the ferrite/spheroidised cementite mixture, assuming the same proportion of phases and an even distribution of cementite spheroids suggests that the area of the α/θ boundary in pearlite is 3.4 times that of cementite when spheroidised according to the mechanisms discussed.

This excess of boundary area represents a stored energy in pearlite, making it susceptible to spheroidisation.

8.3.4.2 Diffusion distances

A carbon atom in a microstructure composed by ferrite and spheroidised cementite has to diffuse across larger distances that one in pearlite, during the course of austenitisation.

As mentioned earlier, the spheroidisation of pearlitic cementite involves the division of cementite lamellae followed by spheroidisation [84, 86]. The distribution of cementite particles can then be idealised as spheres of radius r_θ located on a body-centred cubic lattice of parameter $17.8d_\theta$, as described in Figure 8.14.

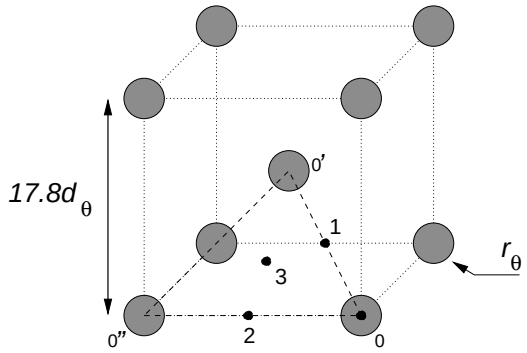

Figure 8.14: Idealised distribution in space of the cementite particles in a spheroidised microstructure, where d_θ is the thickness of the original cementite lamellae and r_θ is the radius of each spheroid.

Distances represented as $\overline{01}$, $\overline{02}$ and $\overline{03}$ in Figure 8.14 are representative of three special cases of soft impingement of the carbon diffusion field possible during austenitisation of a spheroidised microstructure. Consider the carbon diffusion field involved in the growth of austenite centred in 0. Point 1 is where the diffusion and transformation field of spheroids 0 and 0' start to overlap. At point 2, diffusion fields of spheroids centred in 0 and 0" get in contact, and 0 and 0' are already overlapping. Finally, at point 3 the diffusion fields of 0, 0' and 0" get in contact, already overlapping at points 1 and 2, and they reaching all the volume of the alloy.

By contrast, the average diffusion distance $\overline{\triangle d}$ of a carbon atom in a pearlite is simply a quarter of the interlamellar spacing:

$$\overline{\triangle d} = \frac{1}{d_{max}} \int_0^{d_{max}} r\, dr = \frac{d_{max}}{2} \tag{8.4}$$

where d_{max} is the longest distance a carbon atom would have to travel before it enters the diffusion field of another cementite lamellae, and r the distance from the centre of the cementite lamellae. To perform the same calculation for a spheroidised microstructure, spherical coordinates have been used, and the spherical volume around the spheroid considered. Instead of engaging in a complex calculation of the extended volume correction to deal with soft impingement, the three cases detailed above have been studied, using $\overline{01}$, $\overline{02}$ and $\overline{03}$ as d_{max}. Hence, $\overline{\triangle d}$ is determined as:

$$\begin{aligned} \overline{\triangle d} &= \frac{1}{V_{max}} \int_V r\, dV \\ &= \frac{1}{\frac{4}{3}\pi d_{max}^3} \int_0^{2\pi} \int_0^{\pi} \int_0^{d_{max}} r\,(r^2 \sin(\phi))\, dr d\phi d\varphi \\ &= \frac{3}{4} d_{max} \end{aligned} \tag{8.5}$$

where V is the volume of integration, r, ϕ, and φ are the coordinate axis in spherical symmetry. The maximum diffusion distance d_{max} for pearlite and for each of the three cases described earlier for a spheroidised microstructure, the average diffusion distance for each case and the ratio between each of them and pearlite are shown in Table 8.3. In all cases, the average diffusion distance is several times larger in ferrite/spheroidised cementite than in pearlite. Therefore, it is to be expected that the rate of transformation to austenite will be slower in a spheroidised microstructure.

8.3.4.3 Composition changes

Many of carbides that form during the decomposition of austenite, for example pearlitic cementite and carbides in bainite, precipitate with a substitutional solute content which is

Microstructure	d_{max}	$\overline{\triangle d}$	$\frac{\overline{\triangle d}}{\triangle d_{pearl}}$
Pearlite	$4.45 d_\theta$	$2.23 d_\theta$	1.0
Spheroidised			
$(\overline{01})$	$7.7 d_\theta$	$5.8 d_\theta$	2.6
$(\overline{02})$	$8.9 d_\theta$	$6.7 d_\theta$	3.0
$(\overline{03})$	$9.4 d_\theta$	$7.1 d_\theta$	4.2

Table 8.3: Calculation of the average diffusion distance for carbon in pearlite microstructure and in ferrite/spheroidised cementite. For the latter case, the three cases mentioned above have been calculated. The last column shows the ratio of average diffusion distance to the one for pearlite. d_θ is the original thickness of cementite lamellae in pearlite, and it is used as reference value.

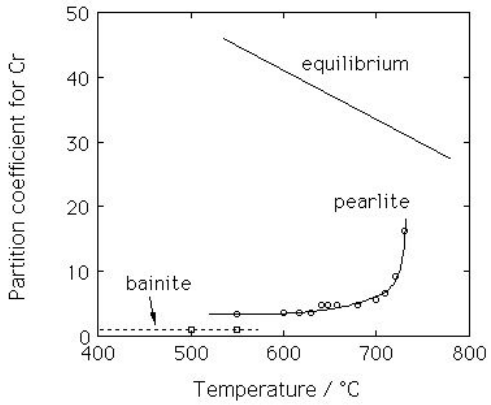

Figure 8.15: Partition coefficient of chromium between cementite and ferrite as a function of transformation temperature. Reproduced from Chance and Ridley [144].

far removed from equilibrium [142, 143, 144] (Figure 8.15). The deviation from equilibrium becomes greater as the transformation temperature is reduced.

Diffusion after initial transformation then occurs as the cementite tends towards its equilibrium composition [143]. Even ferrite sometimes forms without the equilibrium partitioning of substitutional elements [145, 146].

The composition of cementite was determined using MTDATA [3] for the alloy (Table 8.4, and database ALL) for both the equilibrium and paraequilibrium conditions. Energy dispersive X-ray microanalysis was then used on an as-received ferrite/pearlite sample, and on another with a partially spheroidised microstructure to characterise the approximate manganese and chromium contents in cementite. The spheroidised sample had been deformed ($\varepsilon = 1.26$) and then heated at 1°C s^{-1} to 600°C where it was held for 30 minutes.

The results of the calculations and of the analysis are compared in Table 8.4 for manganese and chromium which are present at sufficient concentration. The calculated equilibrium composition of cementite as a function of temperature is illustrated in Figure 8.16. The results in Table 8.4 indicate that the cementite in the as-received sample does not have an equilibrium composition, and that slow heating or annealing is likely to allow it to approach equilibrium. This may in turn influence the subsequent formation of austenite.

Comp. / wt. %	**Bulk alloy**	**MTDATA Paraequilibrium**	**MTDATA Equilibrium**	**Pearlitic cementite**	**Spheroidised cementite**
C	0.54	25.0	25.0	-	-
Mn	0.74	0.57	3.6	1.03 ±0.12	1.43 ±0.14
Cr	0.20	0.16	1.6	0.16 ±0.06	0.30 ±0.07

Table 8.4: Comparison between average composition, calculations performed using MTDATA of the composition of cementite in equilibrium conditions (at 700°C) and paraequilibrium conditions, and experimentally determined compositions of cementite in pearlite and in the spheroidised microstructure.

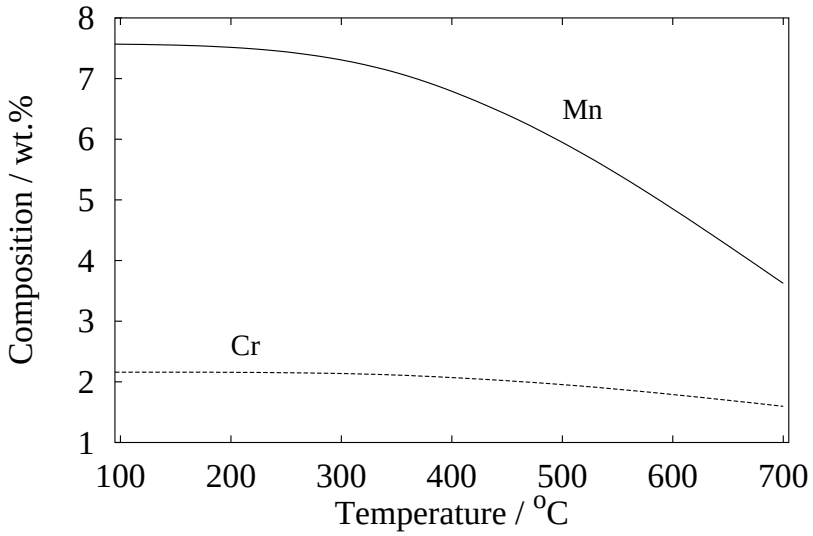

Figure 8.16: Calculated equilibrium composition of cementite as a function of temperature.

8.3.5 Combined effect

In the previous sections, several of the factors that influence the kinetics of transformation to austenite from a mixture of ferrite and pearlite have been discussed. The superposition of the factors can, as will be seen later, produce complex effects.

Figure 8.17 shows the transformation-start during heating for undeformed and deformed ($\varepsilon = 1.26$) samples. The two curves have similar shape, but the A_{c1} temperature is in all cases lower for the deformed samples. Deformation has accelerated transformation kinetics. It is not surprising that the difference between the two curves becomes smaller at high heating rates, since the transformation becomes promoted to higher temperatures, making the effect of initial differences in microstructure less important.

There is nevertheless, a peculiar minimum at $10^{\circ}\mathrm{C\,s^{-1}}$ in both the curves as a function of heating rate. At the slowest of heating rates, the initial mixed microstructure of ferrite and pearlite becomes stabilised during heating prior to the formation of austenite. As already described, the stabilisation takes the form of the spheroidisation of the cementite

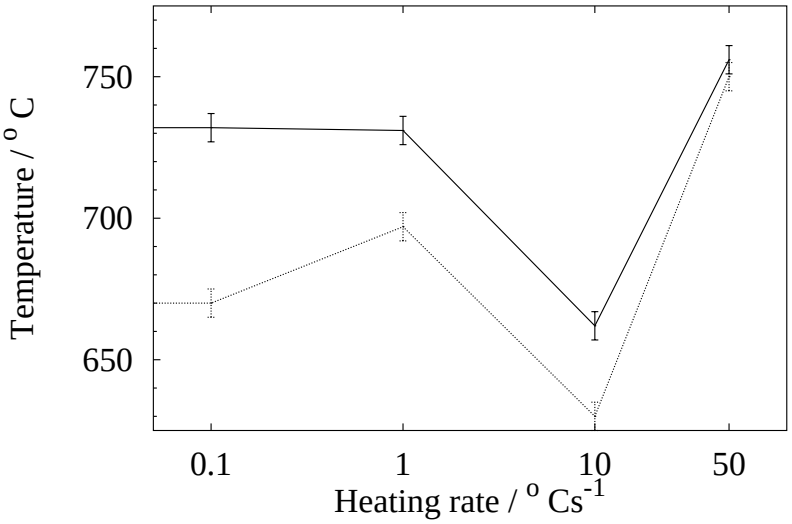

Figure 8.17: The A_{c1} temperature as a function of heating rate and deformation [$\varepsilon = 0.0$ (solid line) and $\varepsilon = 1.26$ (dotted line)]. Lines are printed only as a guide.

lamellae in the pearlite, together with a shift in the chemical composition of the cementite towards equilibrium.

These effects are reduced at intermediate heating rates, leading to a decrease in A_{c1} since the austenite then forms from an initial microstructure which has a higher free energy due to the greater interfacial area per unit volume and the non-equilibrium composition of cementite.

A further increase in the heating rate increases A_{c1} because the process of austenite formation is thermally activated. These phenomena are illustrated schematically in Figure 8.18.

Deformation has a second effect besides of that increasing the kinetics of reaction to austenite. Deformation reduces the temperature at which cementite spheroidises. As described in Section 8.3.2, an alloy than has been cold worked, spheroidises earlier than one which is undeformed. In some cases, the same annealing heat treatment applied to alloys having different levels of cold work, will produce different transformation behaviours.

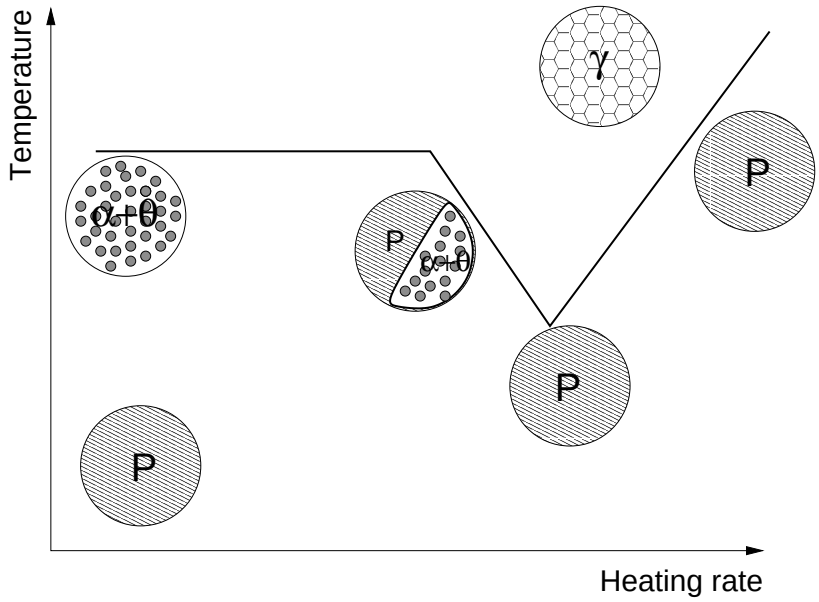

Figure 8.18: Schematic representation of the effect of heating rate on austenitisation of an alloy presenting a eutectoid starting microstructure. The initial, prior to austenitisation and final microstructure are also shown. P represents pearlite, α ferrite, θ spheroidised cementite and γ austenite.

Figure 8.19 presents the start temperature for austenitisation for four alloys with different levels of deformation. The difference with Figure 8.17 is that in this case all the alloys had been annealed for 30 minutes at 600°C. As shown in Figure 8.17, the alloys with lower level of deformation present a transformation behaviour similar to the one shown previously in Figure 8.19. The two alloys with higher levels of deformation do not present the minima in transformation start temperature around 10°C s^{-1}. The reason for this is that for these two alloys the annealing heat treatment has already produced the spheroidisation of pearlite, and therefore they transform at a higher temperature that lamellar pearlite would transform. They behave as is expected of a spheroidised microstructure. The two alloys with less deformation, do not spheroidise during the annealing heat treatment, and therefore they still present the minima due to the early transformation of lamellar pearlite.

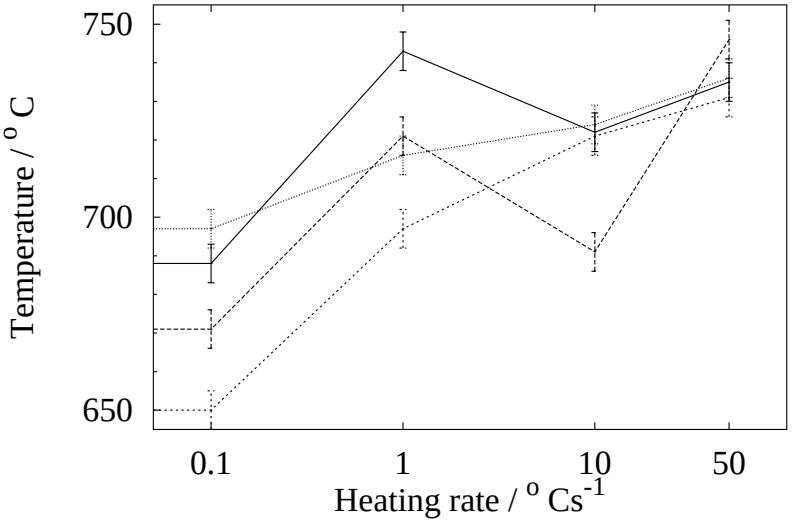

Figure 8.19: The A_{c1} temperature as a function of heating rate and deformation on annealed samples [$\varepsilon = 0.0$ (solid line), $\varepsilon = 0.45$ (long dashed line), $\varepsilon = 0.89$ (short dashed line), and $\varepsilon = 1.26$ (dotted line)]. Lines are printed only as a guide.

To prove this hypothesis, several specimens with different levels of cold work, were annealed for 30 minutes at 600°C and then heated at 1 °C s^{-1} to 750°C, the temperature at which the transformation to austenite has already started, and then quenched. The

final microstructures were characterised using scanning electronic microscopy.

Figures 8.20 to 8.22 show the microstructure of an undeformed sample, in which pearlite has partially transformed into austenite. Comparing the amount of transformation with the samples that had previously been deformed shows how different their transformation rates are.

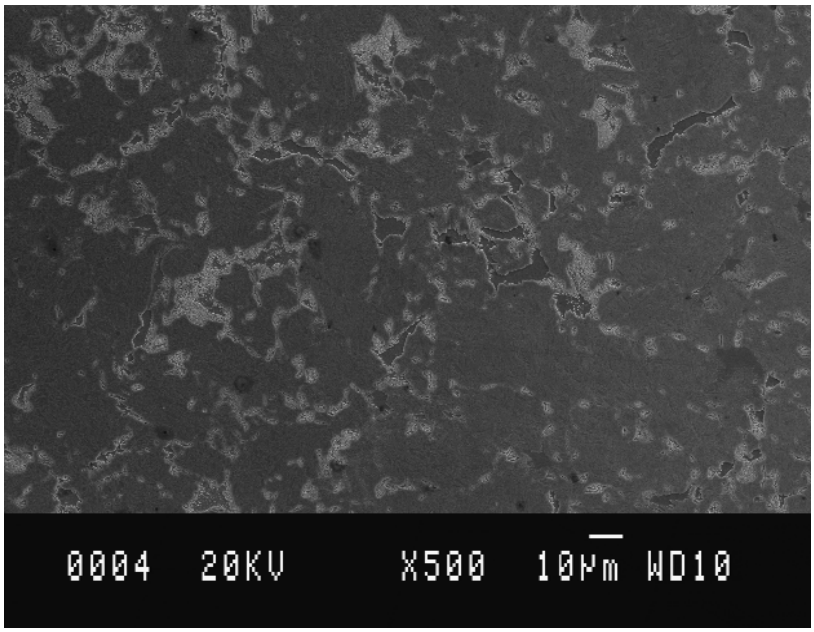

Figure 8.20: Microstructure of an undeformed sample partially transformed to austenite and quenched.

Figures 8.23 to 8.25 show the microstructure obtained on lightly deformed samples ($\varepsilon = 0.45$). The microstructure shows an advanced degree of spheroidisation, and the volume fraction of transformation to austenite is much smaller than in the case of undeformed material.

Finally Figures 8.26 to 8.27 show the microstructure obtained on severely deformed samples ($\varepsilon = 1.26$). It is interesting to see how in the micrograph shown in Figure 8.27, the region in which austenite has developed to a general extent, corresponds to a region were the spheroidisation is lower.

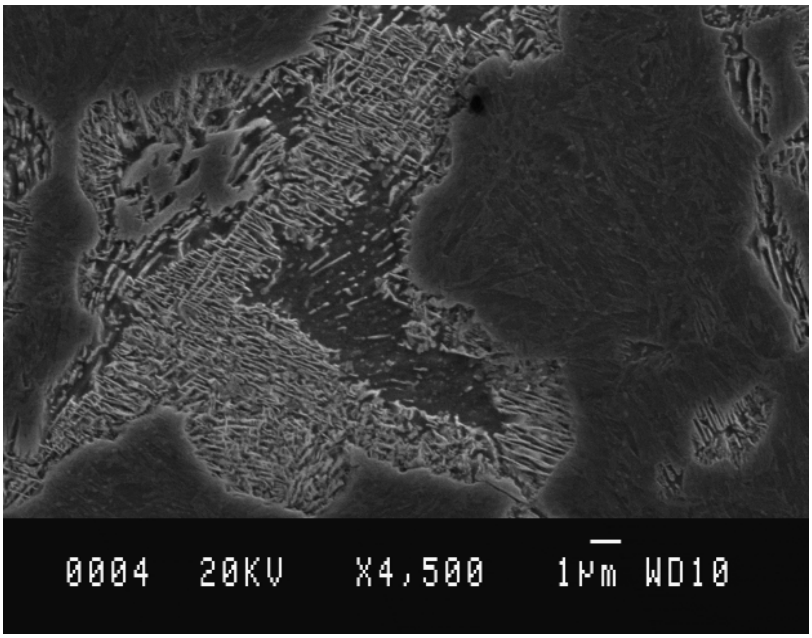

Figure 8.21: Detail of a microstructure of an undeformed sample partially transformed to austenite and quenched.

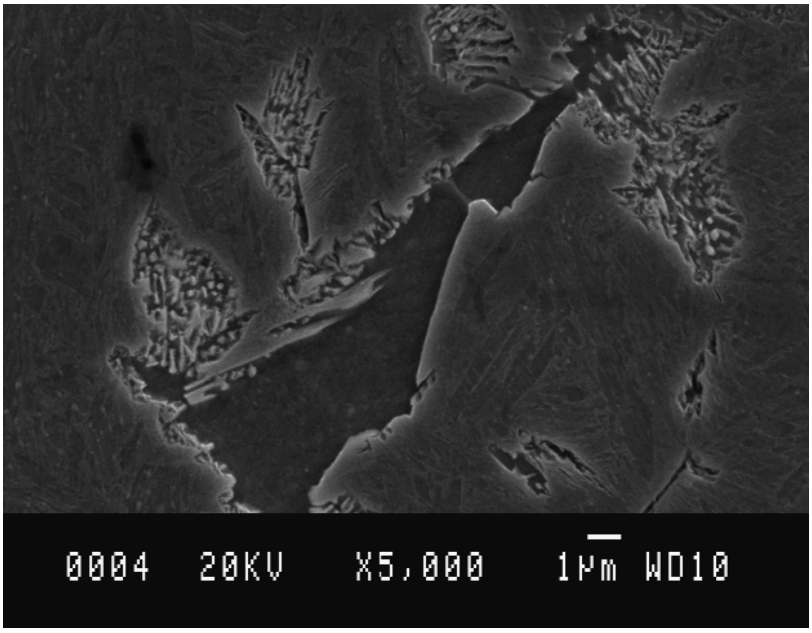

Figure 8.22: Detail of a microstructure of an undeformed sample partially transformed to austenite and quenched.

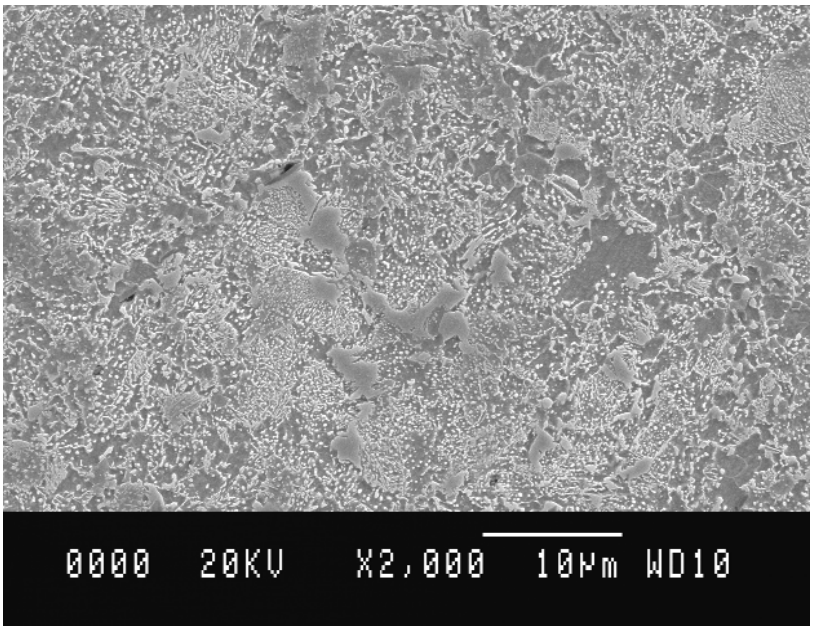

Figure 8.23: Microstructure of a deformed sample ($\varepsilon = 0.45$) partially transformed to austenite and quenched.

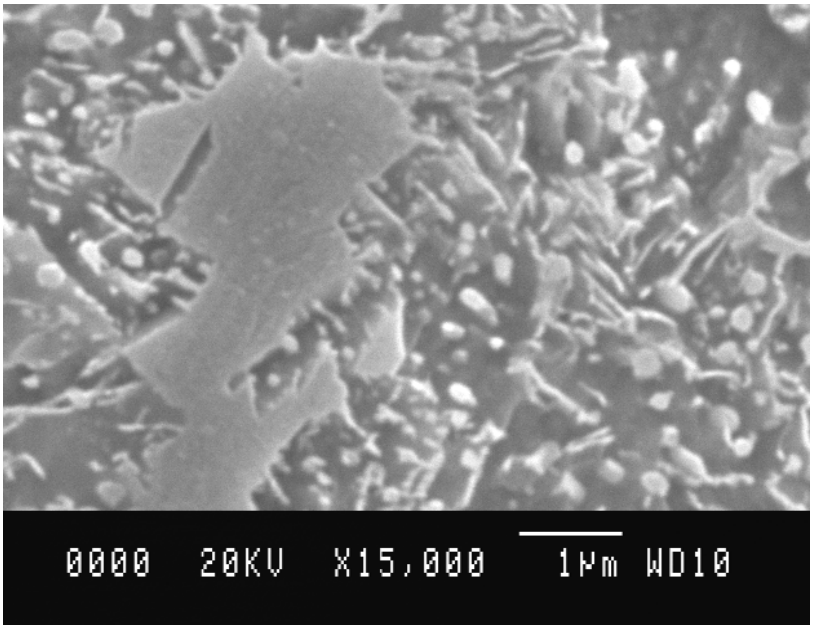

Figure 8.24: Detail of a microstructure of an undeformed sample ($\varepsilon = 0.45$) partially transformed to austenite and quenched.

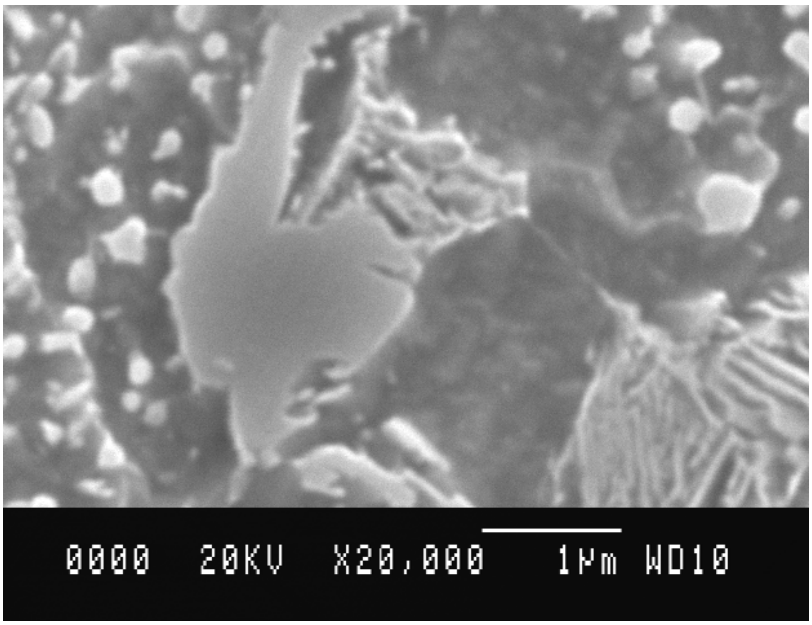

Figure 8.25: Detail of a microstructure of an undeformed sample ($\varepsilon = 0.45$) partially transformed to austenite and quenched.

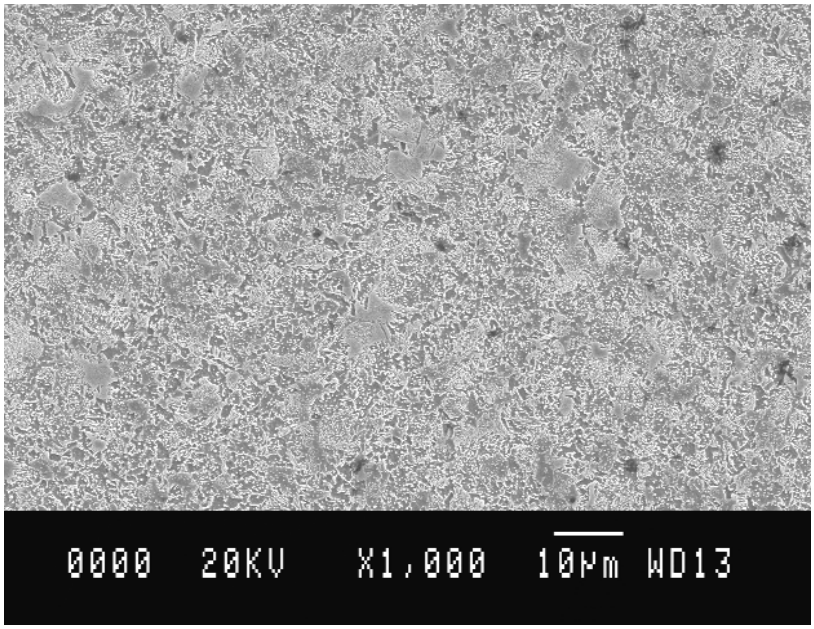

Figure 8.26: Microstructure of a deformed sample ($\varepsilon = 1.26$) partially transformed to austenite and quenched.

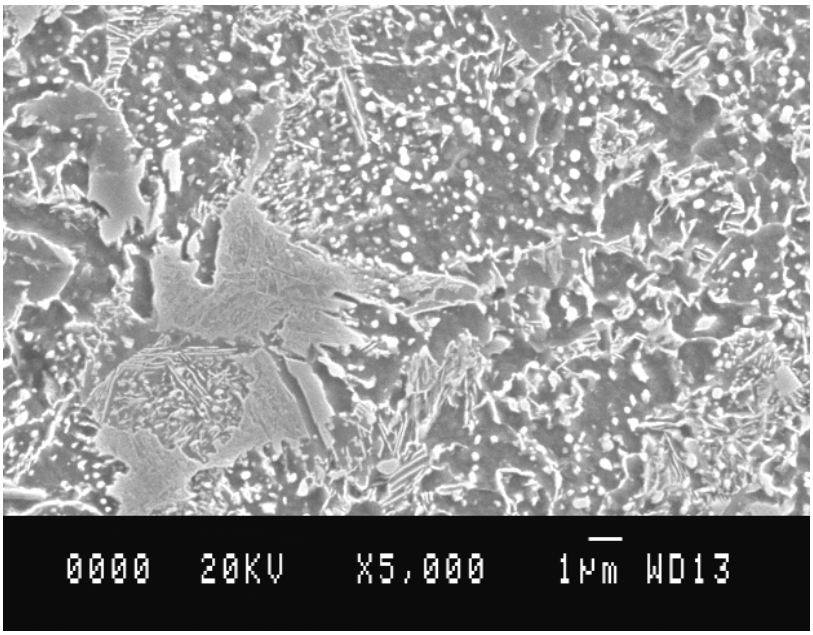

Figure 8.27: Detail of a microstructure of a deformed sample ($\varepsilon = 1.26$) partially transformed to austenite and quenched.

These observations confirm that a short anneal spheroidises pearlitic cementite in alloys that have been deformed by cold work and that this change in the morphology of the phases modifies the alloy's austenitisation behaviour.

8.4 Conclusions

The effect of deformation on the kinetics of austenitisation from a mixture of ferrite and pearlite in a hypoeutectic steel have been characterised. It is found that deformation in general accelerates the transformation rate, and at the same time it reduces the temperature at which spheroidisation of cementite happens and accelerates its kinetics.

Spheroidised cementite is more stable than lamellar pearlite, and thus transformation to austenite from the later proceeds at a faster rate than from the former.

At slow heating rates in deformed materials, spheroidisation occurs and stabilises the microstructure against transformation to austenite. An annealing heat treatment performed at sufficient temperature, given the level of deformation of the alloy, can produce the same spheroidisation effect. At faster heating rates, in which spheroidisation does not have time to occur, austenite grows directly from pearlite. At very fast heating rates, the temperature at which austenitisation starts becomes higher, and the effect of deformation in the kinetics of phase transformation becomes less important compared to overheating.

Chapter 9

Modelling the decomposition of austenite

9.1 Introduction and structure of the model

In almost every process involving the transformation of steel, there is one or more stage in which the alloy has been totally or partially austenitised and is allowed to cool again to ambient temperature, forcing the decomposition of austenite in a myriad of different phases. As the mechanical and physical properties of the component after that process will clearly depend on the distribution of phases generated, it is important to be able to monitor and predict the evolution of the microstructure towards a well-defined target.

The process of decomposition of austenite starts when the temperature of the alloy descends below the upper critical temperature of austenite stability, A_{e3}. If temperatures close to melting are ignored, then above A_{e3} only austenite is thermodynamically stable in low alloy steels. Ferrite formation becomes possible below A_{e3}. The kinetics of transformation below A_{e3} into a variety of transformation products can be qualitatively described by two *C-curves*, as shown in Fig. 9.1.

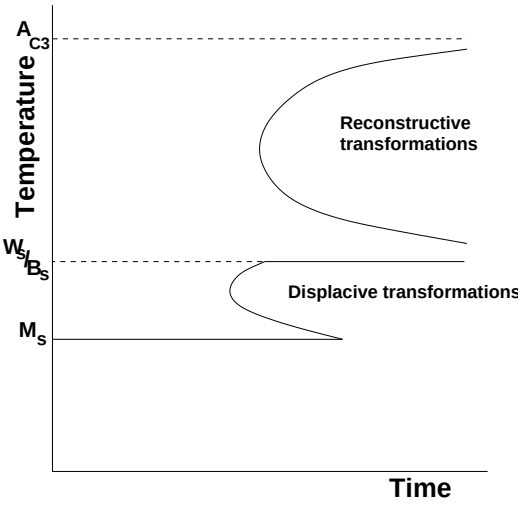

Figure 9.1: Schematic diagram displaying the onset of decomposition of austenite into several transformation products by reconstructive and displacive reactions. A_{c3} is the upper critical temperature of transformation to austenite, W_s is the Widmanstätten-start temperature, B_s is the bainite-start temperature, and M_s is the martensite-start temperature.

These C-curves are defined by the locus of points representing the time to nucleate a detectable degree of transformation. Additional curves can be defined for various amounts of transformation. As described in a previous chapter (Section 2.4), depending on several process parameters, austenite may decompose into variety of transformation products. The reactions that will be considered in this work are the reconstructive formation of allotriomorphic ferrite and pearlite, and the displacive reactions which lead to Widmanstätten ferrite, bainite and martensite, with the possibility of some austenite remaining untransformed (*i.e.* retained austenite). One of the difficulties of modelling this process is that some of these reactions occur simultaneously [6, 129, 14].

Several models exist to describe the diverse transformation products of austenite [129, 14, 147, 16]. These models are briefly reviewed. In the present work these have been modified to create a comprehensive model for the complete set of transformations from austenite during continuous cooling.

9.2 Prediction of decomposition of austenite

The decomposition of austenite in allotriomorphic ferrite, pearlite and Widmanstätten ferrite can sometimes happen simultaneously. A suitable kinetic theory has to be developed to accommodate the fact that the different products influence each other. Classic transformation kinetic theory developed by Kolmogorov [7], Johnson and Mehl [8] and Avrami [9, 10, 11] as adapted by Cahn [148], has been previously modified by Robson and Bhadeshia [12] and Jones and Bhadeshia [129, 14] to permit the treatment of simultaneous transformations.

When different phase transformations overlap, it is necessary to take account of a variety of interactions. When particles nucleated at different locations come into physical contact, hard-impingement is said to have occurred. However, particles at different locations can nevertheless feel each other's presence, via the impingement of their diffusional or thermal fields, a process known as soft-impingement. Both situations lead to interactions

between the developing phases that influence the final microstructure.

9.2.1 Classical overall transformation kinetics for isolated reactions

The evolution of solid state phase transformations is commonly described using the classical Johnson-Mehl-Avrami theory [6]. The formation of a single particle of phase β from a parent phase γ is considered to start after an incubation period τ. assuming that the particle grows isotropically with a growth rate G, then the volume $\tilde{v}_\beta^\tau$ of such a particle is,

$$\tilde{v}_\beta^\tau = \begin{cases} 0 & \text{if } t < \tau \\ \left(\frac{4\pi}{3}\right) G^3 (t-\tau)^3 & \text{if } t > \tau \end{cases} \tag{9.1}$$

where t is time defined as zero at the instant when the alloy reaches the isothermal transformation temperature.

The problem of hard-impingement of growing particles is dealt with using the concept of real and extended volume. The possibility of impingement is at first ignored, allowing particles to grow into and through each other and for nucleation to happen everywhere, including in regions that have already transformed.

The increase in extended volume due to new particles nucleating in a time interval $d\tau$ starting at time τ is,

$$dV_\beta^e = \tilde{v}_\beta^\tau \, I \, V \, d\tau \tag{9.2}$$

$$V_\beta^e = \left(\frac{4\,\pi\,V}{3}\right) \int_0^t G^3 \, I \, (t-\tau)^3 \, d\tau \tag{9.3}$$

where I is the nucleation rate per unit volume and V is the total volume.

However, not all this increase in transformed volume is real. All the contributions to the extended volume that have formed in already transformed regions have to be excluded. If it is assumed that nucleation occurs randomly, the extended volume that nucleates in

untransformed regions at any single instant is proportional to the untransformed volume fraction remaining:

$$dV_\beta = \left(1 - \frac{V_\beta}{V}\right) dV_\beta^e \tag{9.4}$$

$$V_\beta^e = -V \ln\left(1 - \frac{V_\beta}{V}\right) \tag{9.5}$$

so that finally,

$$-\ln\left(\frac{1 - V_\beta}{V}\right) = \left(\frac{4\,\pi}{3}\right) \int_0^t G^3\, I\, (t - \tau)^3 d\tau \tag{9.6}$$

In the special case of constant nucleation and growth rates, equation 9.6 can be integrated easily to give:

$$v_\beta = \frac{V_\beta}{V} = 1 - \exp\left(-\frac{1}{3}\,\pi\, G^3\, I\, t^4\right) \tag{9.7}$$

where v_β is the volume fraction of phase β.

9.2.2 Randomly nucleated simultaneous reactions

The development introduced in the previous section is only viable for individual reactions. A first improvement can be introduced over that case if randomly nucleated simultaneous reactions are considered. Consider the case in which two phases α and β precipitate simultaneously from a parent phase γ. Let I_α, I_β, G_α, G_β be the nucleation and growth rates for phases α and β, which will be considered constant functions of time, with growth being isotropic in each case.

The increase in extended volume of each of the product phases during the interval t to $t + d\tau$ is given by,

$$dV_\alpha^e = \frac{4}{3}\,\pi\, G_\alpha^3\, (t - \tau)^3\, I_\alpha\, V\, d\tau \tag{9.8}$$

and

$$dV_\beta^e = \frac{4}{3}\pi\, G_\beta^3\, (t-\tau)^3\, I_\beta\, V\, d\tau \tag{9.9}$$

The relationship between the extended and real volumes is still defined as before, as the amount or extended volume that has been created on untransformed parent phase γ, but as in this case there are two different product phases, so equation 9.3 becomes

$$dV_\alpha = \left(1 - \frac{V_\alpha + V_\beta}{V}\right) dV_\alpha^e \tag{9.10}$$

and similarly

$$dV_\beta = \left(1 - \frac{V_\alpha + V_\beta}{V}\right) dV_\beta^e \tag{9.11}$$

This development of Avrami's theory can be generalised to any number of product phases. In the most general case the relationship between V_α and V_β will not be a simple. The equations cannot in general be integrated analytically, but numerical integration is necessary. Numerical integration is less transparent but more versatile when there are changing boundary conditions for nucleation and growth.

Considering the general case of n product phases precipitating simultaneously with different nucleation and growth rates, the numerical expression for the increase in extended volume of phase j in the time interval m from t to $t + \Delta t$,

$$\Delta V_j^e = \sum_{k=0}^{m} (V\, I_{j,k}\, \Delta\tau)\, (\tilde{v}_{j,k}\, \Delta t) \tag{9.12}$$

where ΔV_j^e has contributions from particles of phase j nucleated in each of the time intervals k from $t = 0$ to the current time, or $t = m\Delta t$, and the equivalent real volume of phase j,

$$\Delta V_j = \left(1 - \frac{\sum_{i=1}^{n} V_i}{V}\right) \Delta V_j^e \tag{9.13}$$

where $\tilde{v}_{j,k}$ is the rate of volume change of a particle of phase j nucleated during the time interval k (comprising the time from $k\Delta\tau$ to $(k+1)\Delta\tau$) during the current time interval (from $t = m\Delta t$ to $t = (m+1)\Delta t$). $V\,I_{j,k}\,\Delta\tau$ represents the number of extended particles of j nucleated in this time interval. The index i represents each of the n product phases present. The terms $\Delta\tau$ and Δt are taken to be identical.

The instantaneous value of volume fraction of the product phase j at time $t + \Delta t$, $v_j^{t+\Delta t}$, is updated, alongside with that of the other phases, at each numerical time interval by determining,

$$v_j^{t+\Delta t} = \frac{1}{V}\left(V_{j,t} + \Delta V_j\right) \quad \text{for } j = 1 \ldots n \tag{9.14}$$

Other parameters like the nucleation and growth rates can also be updated at this point as appropriate. The composition of the matrix can also be modified to account for solute depletion or enrichment due to transformation.

9.2.3 Boundary nucleated simultaneous reactions

The following analysis is an adaptation of the general theory on phase transformations [6], presented by Jones and Bhadeshia [129, 14]. In this method, the concept of extended space is used twice, first to account for the gradual elimination of untransformed boundary area, and the second to determine the real transformed volume from the extended one.

O_B is defined as planar boundary with the area of the total grain boundary area per unit volume in the alloy, and the precipitation of n product phases is considered. $O_{i,y}$ is the total real area intersected by the ith product phase on a surface at a plane parallel to O_B at a normal distance y from it, at time t. For the jth phase,

$$\Delta O_{j,y} = \left(1 - \frac{\sum_{i=1}^{n} O_{i,y}}{O_B}\right) \Delta O_{j,y}^{e} \tag{9.15}$$

where $\Delta O_{j,y}$ is the change in the real area intersected with the plane at y by phase j, during the time interval from t to $t + \Delta t$. $\Delta O^e_{j,y}$ is the increment in extended area intersected in the same conditions, accounting from all particles nucleated from $t = 0$ to $t = m\,\Delta t$, or actual instant. If that is so,

$$\Delta O^e_{j,y} = \sum_{k=0}^{m} (O_B\, I_{j,k}\, \Delta\tau)\, (A_{j,k,y}\, \Delta t) \tag{9.16}$$

where $A_{j,k,y}$ is the rate of increase of the extended intersection area of a particle of phase j on a plane at distance y, nucleated in the time interval $k\tau$ to $(k+1)\tau$, during the current time interval $t = m\Delta t$ to $t = (m+1)\Delta t$. $I_{j,k}$ is the nucleation rate per unit area of phase j in the time interval $k\tau$ to $(k+1)\tau$. $O_B\, I_{j,k}\, \Delta\tau$ is the number of nucleated particles of phase j during such interval. $\Delta\tau$ and Δt are taken to be identical. Then $\Delta O_{j,y}$ is used to update the total area of intersection of phase j with the same plane at y at time $t + \Delta t$ as follows,

$$O^{t+\Delta t}_{j,y} = O^t_{j,y} + \Delta O_{j,y} \quad \text{for } j = 1 \ldots n \tag{9.17}$$

The change in extended volume of phase j on one side of the boundary can be calculated by integrating,

$$dV^e_j = \int_{y=0}^{y=q^{max}_j} dO_{j,y}\, dy \tag{9.18}$$

where $dO_{j,y}$ is analogous to $\Delta O_{j,y}$, and q^{max}_j is the maximum extended size of a particle of phase j on one side of the boundary in the direction normal to the boundary plane. Alternatively, the change in extended volume of phase j on one side of the boundary in the time interval t to $t + \Delta t$ can be calculated numerically as well as,

$$\Delta V^e_j = \Delta y \sum_{y=0}^{y=q^{max}_j} \Delta O_{j,y} \tag{9.19}$$

where Δy is a small interval in y. The change in real volume after allowing for impingement with other particles originating from other boundaries is,

$$\Delta V_j = \left(1 - \frac{\sum_{i=1}^{n} V_i}{V}\right) \Delta V_j^e \tag{9.20}$$

with V_i being the real volume of the ith phase at time t. The instantaneous value of ΔV_j, together with the corresponding changes in the volumes of the other $n-1$ phases can be used to calculate the total real volume of each phase at time $t + \Delta t$ in a numerical implementation on this method by doing,

$$V_j^{t+\Delta t} = V_j^t + \Delta V_j \quad \text{for } j = 1 \ldots n \tag{9.21}$$

In the following sections these equations will be applied to the prediction of allotriomorphic ferrite, pearlite and Widmanstätten ferrite precipitation. These phases will be referred by the subindices 1, 2 and 3 respectively.

9.2.4 Formation of allotriomorphic ferrite

The nucleation of allotriomorphic ferrite can be modelled using classical nucleation theory, being the grain boundary nucleation rate per unit area given by,

$$I_1 = C_a \frac{k\,T}{h} \exp\left(-\frac{G^* + Q}{R\,T}\right) \exp\left(-\frac{\tau^*}{t}\right) \tag{9.22}$$

where h is the Planck constant, k is the Boltzmann constant, $C_a = 1.214 \times 10^{12}\mathrm{m}^{-2}$ is a fitting constant [14], R is the universal gas constant, $Q = 200\,\mathrm{kJ\,mol}^{-1}$ is a constant activation energy representing the barrier to the transfer of atoms across the interface [129, 89], G^* is the activation energy for nucleation, and it can be determined by,

$$G^* = \frac{C_b \sigma^3}{\Delta G^2} \tag{9.23}$$

where $\sigma = 0.025\,\mathrm{J\,m^{-2}}$ is the interfacial energy per unit area [129], $C_b = 12.83$ is another fitting parameter which has been adjusted experimentally and ΔG is the maximum chemical free energy change per unit volume available for nucleation.

The second exponential term in equation 9.22 refers to the time needed to achieve a steady-state nucleation rate,

$$\tau^* = n_c^2\, h(4\, a_c\, k\, T)^{-1}\, \exp\left(\frac{Q}{RT}\right) \tag{9.24}$$

where n_c is the number of atoms in the critical nucleus and a_c is the number of atoms in the critical nucleus which are at the interface.

Allotriomorphic ferrite is assumed to be in the form of discs with faces parallel to the boundary plane, growing into both the adjacent austenite grains, under paraequilibrium conditions. The half thickness q_1 of each disc can be expressed by a parabolic law,

$$q_1 = \psi_1 (t - \tau)^{1/2} \tag{9.25}$$

where ψ_1 is the one-dimensional parabolic thickening rate constant and τ is the nucleation time. The growth is expected to slow down as the concentration gradient ahead of the moving interface decreases to accommodate the carbon that is partitioned into austenite. The growth rate parallel to the parent boundary is considered to be proportional to q_1, keeping an aspect ratio $\eta_1 = 3.0$ [14].

In the case of a non-isothermal reaction, the change in thickness can be accounted as

$$dq_1 = \frac{1}{2}\psi_1 (t - \tau)^{-1/2}\, dt \tag{9.26}$$

Then, for a particle nucleated at time $\tau = k\Delta\tau$, the half thickness at time $(m+1)t$ can be determined numerically as,

$$q_1^{(m+1)\Delta t} = q_1^{m\Delta t} + \frac{1}{2}\psi_1 (m\Delta t - k\Delta\tau)^{-1/2}\, \Delta t \tag{9.27}$$

The rate of change in area of intersection on a plane y (parallel to the boundary) of a disc of allotriomorphic ferrite nucleated at $\tau = k\Delta\tau$ at the time $m\Delta t$ is:

$$A^k_{1,y} = \begin{cases} \pi\eta_1^2\psi_1^2 & \text{for } q_1^{(m+1)\Delta t} > y \\ \frac{\pi\eta_1^2(q_1^{(m+1)\Delta t})^2}{\Delta t} & \text{for } q_1^{(m+1)\Delta t} = y \\ 0 & \text{for } q_1^{(m+1)\Delta t} < y \end{cases} \tag{9.28}$$

As allotriomorphic ferrite grows on both sides of the interface between austenite grains, it follows from equation 9.19 that

$$\Delta V_1^e = 2\,\Delta y \sum_{y=0}^{y=q_1^{max}} \Delta A_{1,y} \tag{9.29}$$

The parabolic rate constant ψ_1 can be determined by solving [6]

$$2\left(\frac{D}{\pi}\right)^{1/2}\Omega = \psi_1 \exp\left(\frac{\psi_1^2}{4\overline{D}}\right)\operatorname{erfc}\left(\frac{\psi_1}{2\overline{D}^{1/2}}\right) \tag{9.30}$$

with

$$\Omega = \frac{x^{\gamma\alpha} - \overline{x}}{x^{\gamma\alpha} - x^{\alpha\gamma}} \tag{9.31}$$

where $x^{\gamma\alpha}$ and $x^{\alpha\gamma}$ are the paraequilibrium carbon concentrations in austenite and ferrite, respectively, at the interface, $\overline{x}$ is the average carbon concentration in the alloy, and $\overline{D}$ is a weighted average diffusivity of carbon in austenite, given by:

$$\overline{D} = \int_{x^{\gamma\alpha}}^{\overline{x}} \frac{D(x)}{\overline{x} - x^{\gamma\alpha}}\,dx \tag{9.32}$$

9.2.5 Formation of pearlite

The nucleation of pearlite is treated in a very similar way to that of allotriomorphic ferrite but with a lower density of nucleation sites resulting in a nucleation rate about two orders of magnitude smaller than that for allotriomorphic ferrite.

The growth of pearlite is approximated to occur by a paraequilibrium mechanism, although this is seldom the case. It is assumed that growth is controlled by the diffusion of carbon in the austenite ahead of the transformation front. The pearlite growth rate can then be estimated as [149],

$$\psi_2 = \frac{D}{g}\frac{s^2}{d_\alpha d_\theta}\frac{x^{\gamma\alpha} - x^{\gamma\theta}}{x^{\theta\gamma} - x^{\alpha\gamma}}\frac{1}{s}\left[1 - \frac{s_c}{s}\right] \tag{9.33}$$

where θ represents cementite, α represents pearlitic ferrite, and γ austenite. The geometric factor g equals 0.72 in plain carbon steels [149], s is the interlamellar spacing of pearlite and its critical value at which growth stops is s_c, d_α and d_θ are respectively the thickness of ferrite and cementite lamellae. s and s_c are estimated empirically [150] and it is assumed that s takes a value consistent with the maximum rate of growth.

The shape of each pearlite colony is assumed to be that of a disc, with an aspect ratio $\eta_2 = 1.0$. The half thickness of the disc is

$$q_2 = \psi_2 (t - \tau) \tag{9.34}$$

with

$$q_2^{(m+1)\Delta t} = q_2^{m\Delta t} + \psi_2 \Delta t \tag{9.35}$$

The rate of change of area of intersection on a test-plane located at a distance y is given by

$$A_{2,y}^k = \begin{cases} 2\pi\eta_2^2\psi_2^2 (m\Delta t - k\Delta\tau) & \text{for } q_2^{(m+1)\Delta t} > y \\ \frac{\pi\eta_2^2 (q_2^{(m+1)\Delta t})^2}{\Delta t} & \text{for } q_2^{(m+1)\Delta t} = y \\ 0 & \text{for } q_2^{(m+1)\Delta t} < y \end{cases} \tag{9.36}$$

Pearlite, like allotriomorphic ferrite, grows on both sides of the interface (reconstructive reaction), so the increment of extended volume of pearlite is given by

$$\Delta V_2^e = 2\,\Delta y \sum_{y=0}^{y=q_2^{max}} \Delta A_{2,y} \tag{9.37}$$

9.2.6 Formation of Widmanstätten ferrite

As mentioned earlier, Widmanstätten ferrite is formed by a displacive mechanism, below a certain temperature threshold, W_s, as illustrated in figure 9.1. The driving force for its formation has to exceed a stored energy term, estimated into be 50 $\mathrm{J\,mol^{-1}}$ [151]. Nucleation of displacively formed ferrite below W_s (or B_s in the case of bainite), means that the free energy for nucleation ΔG has to be lower than G_N, a function that gives the minimum free energy change necessary to nucleate Widmanstätten ferrite or bainite in any steel, determined to be [151],

$$G_N = 3.637\,(T - 273.18) - 2540 \quad (\mathrm{J\,mol^{-1}}) \tag{9.38}$$

where T is the absolute temperature.

If the conditions for nucleation of Widmanstätten ferrite are met, the nucleation rate can be calculated as

$$I_3 = \frac{1}{2C_c} \exp\left(-\frac{C_d}{RT} - \frac{C_d\,\Delta G}{C_e\,RT}\right) \tag{9.39}$$

where $C_c = 6.78 \cdot 10^{-10}\mathrm{m}^2$, $C_d = 2.065 \cdot 10^4\,\mathrm{J\,mol^{-1}}$ and $C_e = 2540 \cdot 10^{-10}\,\mathrm{J\,mol^{-1}}$ are fitting constants determined from experimental data [152, 153].

The diffusion-controlled growth of plates has been studied by Trivedi [154], and an analytical solution presented. The plates are modelled as parabolic cylinders, and constant growth throughout is assumed. The plate lengthening rate ψ_3 at a temperature T for steady-state growth is obtained by solving the equation,

$$\Omega = (\pi p)^{1/2} \exp(p)\,\mathrm{erfc}\left(p^{1/2}\right)\left[1 + \frac{r_c}{r}\Omega\,S_3(p)\right] \tag{9.40}$$

where the Péclet number p, which is a dimensionless velocity, is defined as,

$$p = \frac{\psi_3 \, r}{2\overline{D}} \tag{9.41}$$

The weighed average diffusion coefficient is determined using equation 9.32 but due to capillarity effects [6], the integration range is $\overline{x}$ to x_r, where the later is the carbon concentration at the tip of the plate, which can be substantially different from $x^{\gamma\alpha}$ [6]:

$$x_r = x^{\gamma\alpha}\left[1 + \frac{\Gamma}{r}\right] \tag{9.42}$$

where r is the radius of curvature of the tip of the plate, and Γ is the capillarity constant

$$\Gamma = \frac{\sigma \, V_m}{RT} \frac{\frac{1-x^{\gamma\alpha}}{x^{\alpha\gamma}-x^{\gamma\alpha}}}{1 + \frac{d(\ln \Gamma_C)}{d(\ln x^{\gamma\alpha})}} \tag{9.43}$$

where the interface energy per unit area is taken to be $\sigma = 0.2\,\mathrm{J\,mol^{-2}}$, Γ_C is the activity coefficient of carbon in austenite, V_m is the molar volume of ferrite, and all the paraequilibrium concentrations are calculated after allowing for the $50\,\mathrm{J\,mol^{-1}}$ of stored energy.

The plate grows as long as the tip radius does not achieve a critical value r_c, at which moment the carbon concentration in front of the tip of the plate becomes $x_r = \overline{x}$, because of the Gibbs-Thompson capillarity effect, and growth stops [6].

It is assumed that the composition of ferrite is not affected by capillarity, as $x^{\alpha\gamma}$ is always very small. r_c can be determined by setting $x_r = \overline{x}$. The function of the Péclet number, $S_3(p)$, introduces a correction for variations in composition due to changing curvature along the interface and has been numerically evaluated by Trivedi [154]. The hypothesis that the plate tip adopts a radius that is consistent with the maximum rate of growth [155] is also assumed.

To calculate the volume, the plates of Widmanstätten ferrite are approximated as tetragonal prisms, with the longest dimension given by

$$q_3 = \psi_3 \left(t - \tau\right) \tag{9.44}$$

during isothermal growth, or by

$$q_3^{(m+1)\Delta t} = q_3^{m\Delta t} + \psi_3 \, \Delta t \tag{9.45}$$

for non-isothermal processes. The approximation arises because Trivaldi's solution is for a parabolic cylinder whereas the volume considered here is a tetragonal prism.

The rate of change in area of intersection on a plane y from the austenite grain boundary is therefore,

$$A_{3,y}^k = \begin{cases} 2\eta_3^2\psi_3^2(m\Delta t - k\Delta\tau) & \text{for } q_3^{(m+1)\Delta t} > y \\ \frac{\eta_3^2(q_3^{(m+1)\Delta t})^2}{\Delta t} & \text{for } q_3^{(m+1)\Delta t} = y \\ 0 & \text{for } q_3^{(m+1)\Delta t} < y \end{cases} \tag{9.46}$$

As Widmanstätten ferrite grows only on one side of the boundary between austenite grains, it follows that,

$$\Delta V_3^e = \Delta y \sum_{y=0}^{y=q_3^{max}} \Delta A_{3,y} \tag{9.47}$$

The model by Jones and Bhadeshia does not include the formation of bainite. To that end, a model by Takahashi and Bhadeshia has been used, which is reviewed in the following section.

9.2.7 Formation of bainite

The study of the transformation to bainite involves a greater complexity than the other reactions reviewed thus far. It has been found experimentally that in steels in which other transformation reactions do not interfere with the formation of bainitic ferrite, the maximum volume fraction of bainitic ferrite after long isothermal holding times is lower

than would be expected, if only equilibrium or paraequilibrium conditions are taken into account. When the substitutional lattice is configurationally frozen, the transformation must stop when austenite achieves its paraequilibrium carbon concentration, as defined by the $A_{e'3}$ curve on the phase diagram. The bainite reaction, in fact stops short of that, when the carbon concentration of austenite approaches the T_0 curve, which is defined by the locus of points on the phase diagram where ferrite and austenite of the same composition have the same free energy, as shown in Fig. 9.2. As the growth of bainite leads to an invariant-plane strain shape deformation, there is a strain energy term of about 400 J mol^{-1} [151] which must be accounted for. The inclusion of this term modifies the T_0 to the T_0' [147].

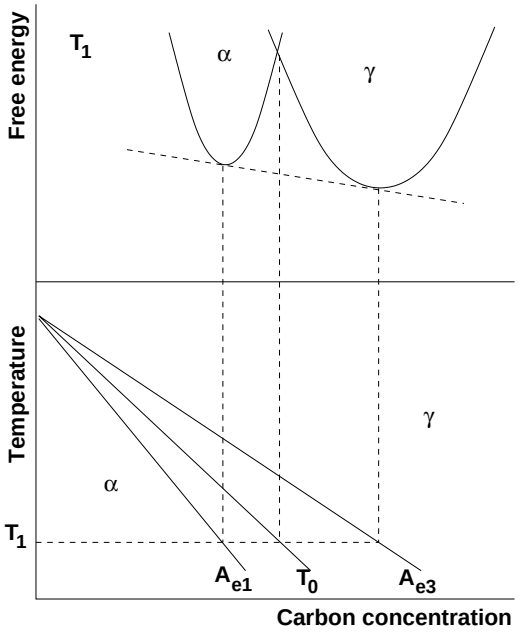

Figure 9.2: Schematic diagram showing the origin of T_0 line construction in carbon steels

In these circumstances, and ignoring the small density difference between austenite and ferrite, the maximum volume fraction of bainitic ferrite can be determined by applying the lever rule to A_{e1}' and T_0.

$$V_b = \frac{(x_{T_0} - \bar{x})}{(x_{T_0} - x^{\alpha\gamma} - x_C)} \tag{9.48}$$

where x_{T_0} is the carbon concentration of austenite when it reaches the T_0 curve, $x^{\alpha\gamma}$ is the paraequilibrium carbon concentration of bainitic ferrite, $\bar{x}$ is the average carbon concentration of the steel, and x_C is the amount of carbon precipitated to form carbides within bainitic ferrite.

Most industrial processes, involve continuous cooling transformations. It is then necessary to estimate the appropriate temperature time transformation (TTT) and continuous cooling transformation (CCT) diagrams for bainite. This can be done using a method based on Russell's expression for incubation times during nucleation [156, 26, 25]. That incubation period, which represents the start of transformation, follows a C-curve behaviour as a function of temperature. Takahashi and Bhadeshia [147] adapted that method to predict a series of C-curves representing different volume fractions of transformation.

The incubation time τ_s for the beginning of transformation is determined by [147],

$$\ln\left[\tau_s G_{max}^{p} T^{-z}\right] = \left(\frac{Q'}{RT}\right) + C_f \tag{9.49}$$

where p, z, Q', and C_f are constants obtained by fitting to experimental data on a large variety of steels, and G_{max}^{p} is the maximum driving force available for nucleation. To determine the progress of the bainite reaction, a mass balance is used to determine the enrichment of austenite with carbon. G_{max}^{p} is determined for the new composition of austenite and equation 9.49 applied again to generate a new curve. This method is repeated to find curves for different fractions of transformation.

Once a bainite TTT diagram has been calculated in this way, and assuming that the additivity principle applies to all the curves in the diagram, Scheil's rule [18] is used to determine the CCT diagram. For each subsequent temperature interval, a new set of curves is calculated and the amount of bainite precipitated is determined.

In alloys with a high silicon content (≈2 wt.%), the carbide precipitation from austenite is highly retarded, so that excess carbon partitioned from the newly formed bainitic ferrite contributes to the enrichment of the residual austenite [157, 93]. In alloys with a low silicon content, some of the carbon precipitates, reducing the enrichment of austenite. The threshold from one behaviour to the other has been set at about 1 wt.% of silicon.

9.2.8 Formation of martensite

The amount of austenite that does not decompose to martensite on cooling below the martensite-start (M_s) temperature is given by the Koistinen and Marburger equation [16],

$$v_\gamma = \exp[-1.1 \cdot 10^{-2}(M_s - T_q)] \tag{9.50}$$

where T_q is the temperature below M_s in °C.

9.2.9 Determination of critical temperatures for transformation

There are three critical temperatures mentioned in previous sections, whose accurate prediction is important in describing the decomposition of austenite.

A_{e3} is the temperature below which austenite becomes unstable with respect to ferrite. The maximum temperature at which ferrite can form by a displacive mechanism during an isothermal heat treatment is designated T_h; it defines the "flat top" of the displacive C-curve on the isothermal transformation diagram (figure 9.1). Depending on the circumstances, T_h represents the Widmanstätten ferrite-start temperature W_s or the bainite-start temperature B_s. Finally the martensite-start temperature M_s is the point at which the driving force for transformation is large enough to sustain completely diffusionless nucleation and growth.

9.2.9.1 A'_{e3} temperature

A'_{e3}, or the no-substitutional element partitioning curve is determined using a quasi-chemical thermodynamic model [158, 159].

9.2.9.2 B_s temperature

If $W_s > B_s$, then the bainite-start temperature is calculated on the growth condition alone. It is defined by the point where the driving force for diffusionless transformation $\Delta G^{\gamma-\alpha}$ exceeds the stored energy of bainite G_{SB} [160].

$$\Delta G^{\gamma\rightarrow\alpha} < -G_{SB} \tag{9.51}$$

The stored energy G_{SB} is about 400 J/mol when the shape deformation is elastically accommodated [160].

9.2.9.3 M_s temperature

The martensite-start temperature for a steel of any composition can be determined by balancing a critical driving force for nucleation against the available chemical free energy change involved in the transformation from austenite to martensite [161]. The determination of the later involves extrapolating the free energy surfaces between austenite and ferrite to conditions where they would not be in thermodynamic equilibrium. Aaronson *et al.* [133] adapted previous method to perform this calculation, method which has been subsequently improved first by Shiflet *et al.* [159], and finally by Bhadeshia [162]. M_s is determined from the equation of the free energy change accompanying the transformation from austenite to martensite $\Delta G^{\gamma\rightarrow\alpha'}$ [162, 155, 163].

9.3 Implementation of the model

In previous sections the models used to determine the decomposition of austenite into several product phases have been reviewed. Figure 9.3 shows how all these individual submodels have been integrated into a package able to predict the complete process of decomposition of austenite into allotriomorphic ferrite, pearlite, Widmanstätten ferrite, bainite and martensite.

The calculations start with the determination of the critical temperatures of transformation, as a function of the alloy composition, and the conversion of the temperature cycle in two *equivalent* constant cooling rates that will be applied respectively to the temperature ranges A_{C3} to B_s and B_s to M_s.

The simultaneous decomposition of austenite into allotriomorphic ferrite, pearlite, Widmanstätten ferrite is dealt with following the model by Jones and Bhadeshia [14]. A simple mass balance is used to determine the changes in the carbon composition of austenite as other phases precipitate. When the driving force for transformation is enough to allow the formation of bainite, the model presented by Takahashi and Bhadeshia [147] is used to determine the progress of this phase transformation. During the precipitation of bainite, the carbon composition of austenite can evolve in different ways, for different alloys. Austenite in high silicon steels ($\approx$2 wt.%) become enriched in carbon as other phases precipitate. In steels with a lower silicon content, some of that carbon precipitates in the form of carbides, reducing the amount of carbon dissolved in austenite [157, 93].

When the temperature of the alloy becomes lower than the martensite-start temperature of the remaining austenite, some of the austenite transforms to martensite, whilst some remain as retained austenite. The volume fraction of retained austenite in determined from Koistinen and Marburger [16]

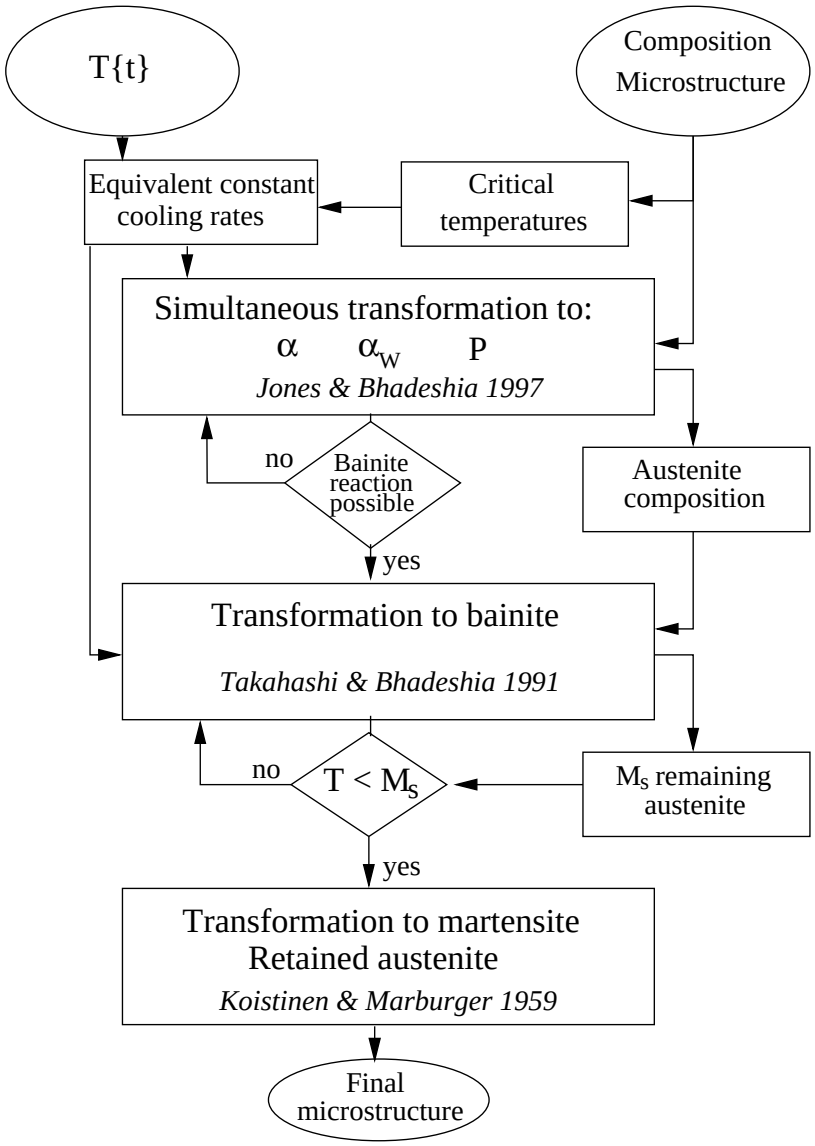

Figure 9.3: Diagram summarising the structure of the model. α represents allotriomorphic ferrite, α_W Widmanstätten ferrite and P pearlite. Ellipses represent input or output data, boxes represent modules of the model, diamonds show conditional clauses and arrows show the flow of data.

9.4 Analysis of model predictions

The discussion in the previous sections (9.1 – 9.3) describes a model to estimate the resulting microstructure from the decomposition of austenite during continuous cooling of a steel as a function of the chemical composition, austenite grain size and cooling cycle.

To check its capability, a series of predictions have been performed for comparison against well established metallurgical trends. As a starting point, the continuous cooling diagram (CCT) of a steel commonly used in forging and induction hardening manufacturing processes (Table 9.1, Steel A), has been determined for three different austenite grain sizes: 2, 10 and 50 μm. The effect of carbon and substitutional solutes has been calculated by determining the CCT diagrams for compositions around that of the base alloy (Table 9.1).

	C wt.%	**Si wt.%**	**Mn wt.%**	**Cr wt.%**	**Ni wt.%**	**Mo wt.%**	**V wt.%**
Steel A	0.55	0.22	0.77	0.20	0.15	0.05	0.001
Steel B	0.30						
Steel C	0.77						
Steel D		1.22					
Steel E						1.05	
Steel F			0.0				
Steel G			1.77				
Steel H				1.20			
Steel I					1.15		

Table 9.1: Composition of base steel and variations used to check the validity of the model presented. Only the composition in one element has been changed in each case. A grain size of 10 μm has been considered in all the cases unless specified otherwise. For the sake of clarity only the variations from the reference composition, Steel A, are shown.

The following constant cooling rates were used in the calculations: 0.01, 0.1, 1, 10, 20, 50 $^{\circ}\mathrm{C\,s^{-1}}$. Constant cooling rates higher than 50 $^{\circ}\mathrm{C\,s^{-1}}$ were considered but this rate

is usually enough to obtain martensite structure in the type of alloy studied here. The calculated CCT diagram for Steel A is shown in Fig. 9.4.

At slow cooling rates, ferrite starts forming at a higher temperature than pearlite, but only at the slowest rates does it reach any appreciable amount (1 %) before pearlite does. Pearlite forms rapidly, transforming 50 % of the austenite shortly after the start of reaction. At a constant cooling rate of 50 $^{\circ}\mathrm{C\,s^{-1}}$, only 1 % of pearlite is formed, transforming most of the austenite to martensite.

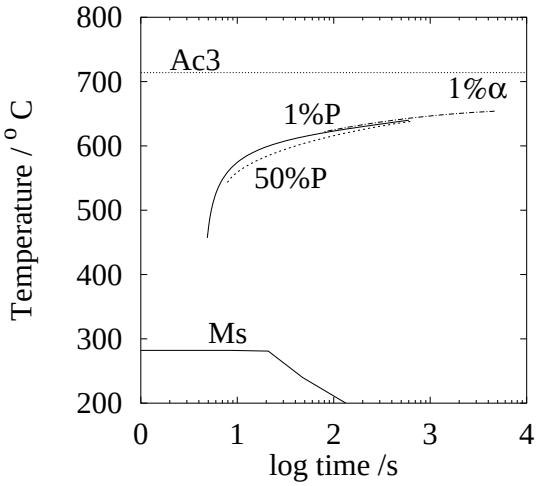

Figure 9.4: Constant cooling transformation diagram for Steel A, considering a grain diameter of 10 μm. α stands for ferrite, P for pearlite, A_{c3} is the upper critical temperature of transformation to austenite, and M_s is the martensite start temperature.

9.4.1 Effect of austenite grain size

Austenite grain size has an important effect on hardenability and hence on the final microstructure of steel. Ferrite and pearlite nucleate mostly at the austenite grain boundaries. A finer grain size provides larger number density of nucleation sites, and therefore leads to more rapid transformation [99].

The CCT diagrams predicted for Steel A for three different grain sizes show that in the case of an microstructure with small grain size (2 μm, Figure 9.5) the reactions are,

as expected, accelerated relative to a larger grain size (10 μm, Figure 9.4). In reality, the reaction starts at the same temperature, but the enhanced nucleation makes that the transformed phase reaches 1 % of transformation earlier. This is still more evident when comparing with the data for 50 μm (Figure 9.6).

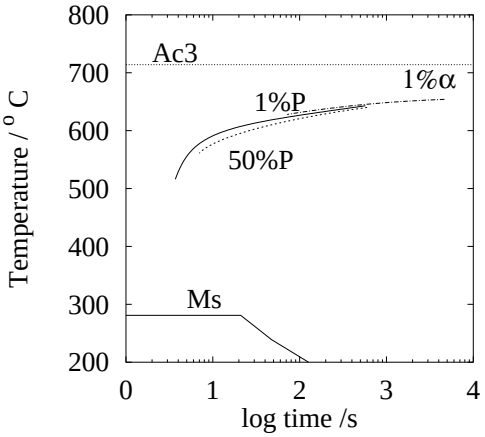

Figure 9.5: Constant cooling transformation diagram calculated for an alloy of composition Steel A, with a grain diameter of 2 μm. α stands for ferrite, P for pearlite, A_{c3} is the upper critical temperature of transformation to austenite, and M_s is the martensite start temperature.

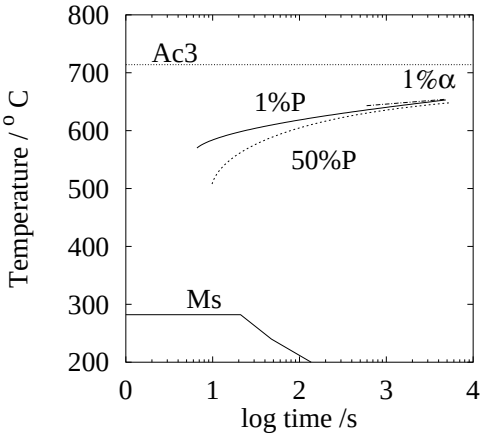

Figure 9.6: Constant cooling transformation diagram calculated for an alloy of composition Steel A, with a grain diameter of 50 μm. α stands for ferrite, P for pearlite, A_{c3} is the upper critical temperature of transformation to austenite, and M_s is the martensite start temperature.

9.4.2 Effect of carbon content

Carbon has a large influence in hardenability [164, 102, 99]. The calculated effect of the progressive addition of carbon to a low-alloy steel is shown in Figure 9.7 9.4 and 9.8, for alloys Steels B, A and C respectively. The martensite-start temperature is clearly reduced by increasing carbon. In the alloy with only 0.30 wt.% C the driving force for pearlite formation is low; it is not until ferrite has precipitated and enriched the austenite that pearlite begins to form. At higher carbon contents, Steel A (Figure 9.4) and Steel C (Figure 9.8), the pearlite reaction curves are shifted to higher temperatures and longer times.

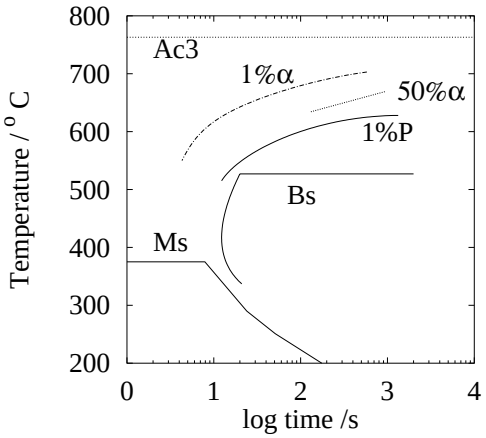

Figure 9.7: Constant cooling transformation diagram for Steel B (0.30 wt.% C), considering a grain diameter of 10 μm. α stands for ferrite, P for pearlite, A_{c3} is the upper critical temperature of transformation to austenite, B_s is the bainite start temperature and M_s is the martensite start temperature. *Note: The bainite curve is only approximate.*

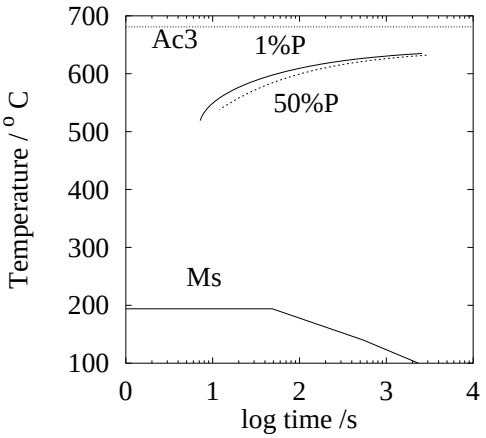

Figure 9.8: Constant cooling transformation diagram for Steel C (0.77 wt.% C), considering a grain diameter of 10 μm. P stands for pearlite, A_{c3} is the upper critical temperature of transformation to austenite and M_s is the martensite start temperature. *Note: The range in the temperature axis has been shifted to include the depressed M_s temperature.*

9.4.3 Effect of substitutional solutes

Most alloying elements tend to displace the transformation curves towards longer times and lower temperatures, hence increasing hardenability [99]. Carbon is the most potent hardenability enhancer and is used as a reference in describing the effect of other solutes [22, 23, 120]. It is thus concluded that carbon is about five times as effective at improving hardenability than chromium, manganese, molybdenum or vanadium, about fifteen times more effective than copper or nickel, and almost twenty-five times more powerful than silicon [22, 23].

The use of these substitutional solutes has benefits other than hardenability. Some of the alloying elements form carbides (Cr, Mo, Ti, V), strengthen the alloy by solid solution hardening (Cr, Mo), reduce the precipitation of carbides (Si), or increase toughness (Ni, Mo) [164].

Elements like silicon and molybdenum shift the position of the eutectoid to lower carbon concentration, thus increasing the volume fraction of pearlite on slow cooling. γ stabilising elements like nickel and manganese shift the eutectoid to lower temperatures, thus slowing the transformation reaction due to the lower diffusion rates. α stabiliser elements like chromium, molybdenum, silicon, titanium and tungsten shift that point to higher temperatures, with the consequence of increasing atom mobility.

In the present model, ferrite and pearlite have been considered to grow by a paraequilibrium mechanism (Section 9.2.4), so the main effects are thermodynamic in origin.

The calculated CCT diagrams for Steel F (Figure 9.9), Steel A (Figure 9.4), and Steel G (Figure 9.10), show the effect of increasing manganese content on the kinetics of transformation. Ferrite and pearlite formation is retarded at high manganese contents and the martensite-start temperature is reduced.

Nickel is also a γ stabilising element, and tends to retard the precipitation of ferrite. This effect is clearly predicted in the CCT diagram for Steel I, shown in Figure 9.11. In the base steel, Steel A, at slow cooling rates ferrite can still achieve 1 % of transformation

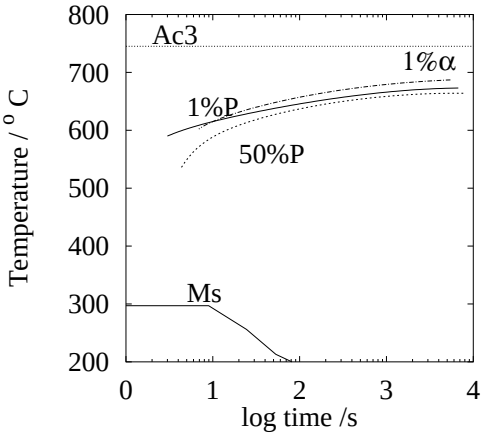

Figure 9.9: Constant cooling transformation diagram for Steel F (0.0 wt.% Mn), considering a grain diameter of 10 μm. P stands for pearlite, A_{c3} is the upper critical temperature of transformation to austenite and M_s is the martensite start temperature.

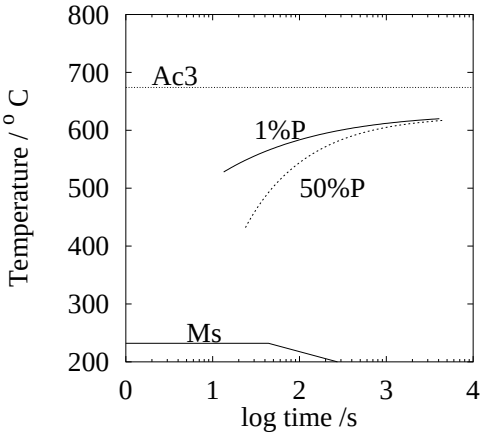

Figure 9.10: Constant cooling transformation diagram for Steel G (1.77 wt.% Mn), considering a grain diameter of 10 μm. α stands for ferrite, P for pearlite, A_{c3} is the upper critical temperature of transformation to austenite and M_s is the martensite start temperature.

before the pearlite reaction reaches the same amount, but with the increased content in nickel of Steel I, this is no longer possible for the range of cooling rates studied. As with all γ stabilising elements, the pearlite reaction is shifted to a lower temperature.

Chromium, molybdenum and silicon are all α stabilising elements. In calculations concerning the alloys enriched with silicon and molybdenum (Steel D and Steel E, Figure 9.13 and Figure 9.14 respectively, the calculated curve for 1 % of transformation to pearlite is not much displaced with respect to the one of the reference alloy, Steel A (Figure 9.4). In the predictions for Steel D and Steel H (enriched with chromium, Figure 9.12), the kinetics of transformation to pearlite are very fast, being the curves for 50 % of transformation almost indistinguishable from the one corresponding to 1 %. The CCT diagrams for these three alloys present a 1 % ferrite curve, opposed to the case of Steel F or Steel I, enriched with γ stabiliser elements, that do not present it.

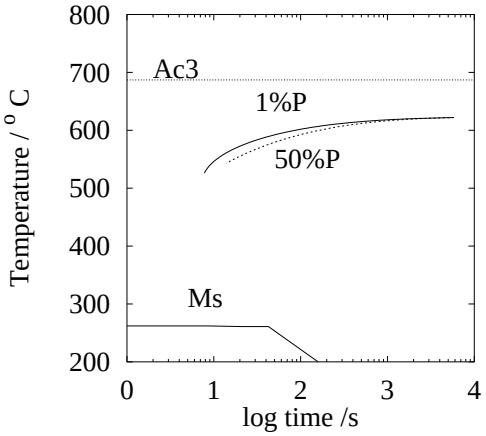

Figure 9.11: Constant cooling transformation diagram for Steel I (1.15 wt.% Ni), considering a grain diameter of 10 μm. P stands for pearlite, A_{c3} is the upper critical temperature of transformation to austenite and M_s is the martensite start temperature.

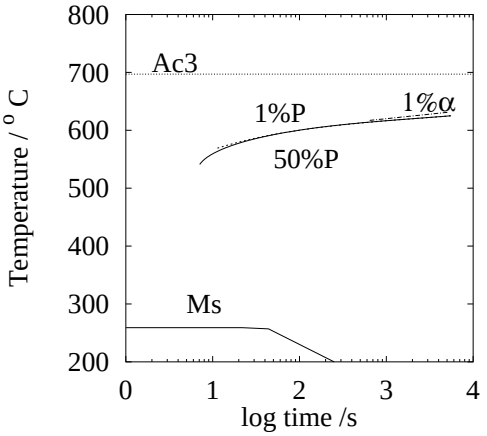

Figure 9.12: Constant cooling transformation diagram for Steel H (1.20 wt.% Cr), considering a grain diameter of 10 μm. α stands for ferrite, P for pearlite, A_{c3} is the upper critical temperature of transformation to austenite and M_s is the martensite start temperature.

9.5 Conclusions

Various existing models on phase transformation of the various product phases of the decomposition of austenite have been modified and combined to produce a comprehensive model of phase transformation in steel during cooling and quenching from austenite. The validity of the model has been satisfactorily assessed by calculating a number of CCT diagrams and checking that they predict correct metallurgical trends.

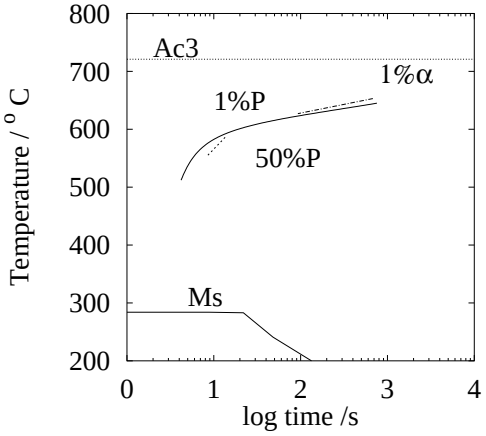

Figure 9.13: Constant cooling transformation diagram for Steel D (1.22 wt.% Si), considering a grain diameter of 10 μm. α stands for ferrite, P for pearlite, A_{c3} is the upper critical temperature of transformation to austenite and M_s is the martensite start temperature.

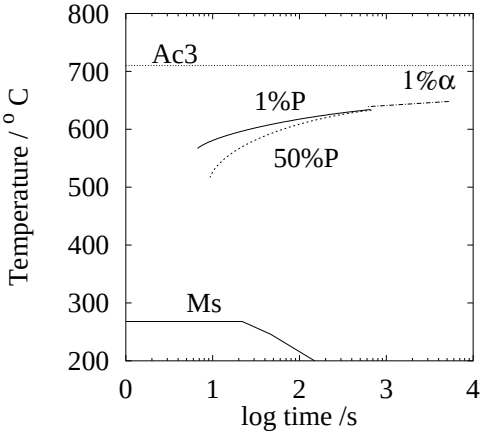

Figure 9.14: Constant cooling transformation diagram for Steel G (1.05 wt.% Mo), considering a grain diameter of 10 μm. α stands for ferrite, P for pearlite, A_{c3} is the upper critical temperature of transformation to austenite and M_s is the martensite start temperature.

Chapter 10

Model of low temperature tempering

10.1 Introduction

The ability to predict the hardness of a component would be useful in many circumstances, for example during quality control. Hardness is sometimes a design target. For the present work on constant velocity joints it is particularly important to model tempering at low temperatures.

The term *low temperature* implies here that there is unlikely to be any substantial recovery or recrystallisation during the time scale of the experiments, the focus instead being on the redistribution of carbon, including the early stages in the precipitation of carbides.

We have seen that an Avrami type approach is useful in modelling the evolution of hardness. As emphasised earlier, the use of hardness instead of transformation fraction is empirical. The relation between these two variables need not to be linear. Therefore, the approach adopted here was to avoid any assumption about the structure-property relation by using a neural network which has as its inputs the Avrami variables. The analysis is based on new and carefully controlled experimental data.

10.2 Experimental procedure

The steel used for the tempering experiments has the chemical composition given in Table 10.1. All samples were austenitised for 10 minutes at 1000 °C. After austenitisation, they were quenched in cold brine. The temperature of the brine was at all times lower than 5°C, and it was thoroughly stirred to avoid the creation of a steam layer at the hot surface of the specimens, that could reduce the rate of heat extraction. The specimens used were cylinders 12 mm in length and 8 mm in diameter. After quenching, they were dried and their flat surfaces ground to remove any oxidised layer. Hardness was measured on a Vickers hardness test machine, with an equivalent load of 30 kg and a pyramid-shaped

diamond indentator. At least three measures of hardness were taken in each case, and six if the variability presented was large.

wt.%	C	Si	Mn	Cr	Ni	Mo	V
Steel A	0.55	0.22	0.77	0.20	0.15	0.05	0.001

Table 10.1: Composition of steel used for the tempering experiments. This alloy is used in the manufacture of induction hardened and tempered steel components for automobiles.

Tempering was performed in a Carbolite fan-oven in which the temperature of the chamber was monitored not only by the built-in thermocouple and control system, but by an independent reading of temperature using a second thermocouple situated close to the sample. The measurements were logged using a data acquisition system on a computer. In order to study whether the method used to perform the temper had any influence in the results, some of the heat treatments have been performed by induction heating in a Thermecmastor Z Thermomechanical Simulator, using specimens of identical geometry.

The tempering conditions were designed to be able to create an evenly distributed database. The temperatures considered range from 50 to 300°C in increments of 50°C. The tempering time ranged from a few seconds to 144 ks. The precise conditions used are shown in Table 10.2.

One sample was tempered for 20 hours (72 ks) at 400°C to determine the hardness that the alloy would present once all carbon had been precipitated from martensite, but before any substantial recovery or recrystallisation occurred. The hardness after the heat treatment is $H_F = 473\,\mathrm{HV}$, with a standard deviation $\sigma \pm 3\,\mathrm{HV}$.

10.3 Training the neural network

The neural network has been trained using the methodologies due to MacKay [137, 113], section 5.1, implemented under an interface developed by Sourmail [136].

Temperature /K	Time /s	Oven	Temperature /K	Time /s	Oven
323	15857	1	473	11777	1
373	194	1	473	11777	1
373	4337	1	473	23400	1
373	9000	1	473	46800	1
373	18000	1	523	43	1
373	36000	1	523	393	1
373	72000	1	523	4807	1
373	144000	1	573	31	0
423	104	0	573	200	1
423	1612	1	573	233	1
473	64	1	573	2294	1
473	738	1	573	2520	1
473	738	1	573	4500	1

Table 10.2: Tempering experiments realised to create the database. The third column of the table, *Oven*, shows the tempering method, 0 means induction tempering and 1 oven tempering.

10.3.1 Database and variables

The database includes the temper parameters time t and temperature T and the tempering method used (oven or induction). Composition was not included because only one alloy has been used. The neural network trained has four input variables: T^{-1}, $\ln(t)$, t and $Oven$, the last input taking the value $Oven = 1$ if the specimen had been oven tempered and $Oven = 0$ if it had been tempered by induction in the thermomechanical simulator. The output variable was defined as:

$$\xi\{T,t\} = \frac{H_{\alpha\prime} - H\{T,t\}}{H_{\alpha\prime} - H_F} \tag{10.1}$$

where $H_{\alpha\prime}$ is the as-quenched hardness of the specimen, $H\{T,t\}$ is the hardness of the specimen after t seconds at absolute temperature T and H_F the hardness of a fully tempered sample. $\xi\{T,t\}$ has been determined with the as-quenched hardness of each specific specimen but using the same measurement of H_F for all data points. The maximum, minimum and average values of each of these inputs are summarised in Table 10.3.

Input variable (unit)	**Minimum**	**Maximum**	**Average**	**Std. deviation**
T^{-1}/K^{-1}	0.0017	0.0031	0.0022	0.0004
$\ln(t/\mathrm{s})$	3.43	11.88	7.74	2.43
t/s	31	144000	15823.81	31276.32
$Oven$	0	1	0.92	0.27

Table 10.3: Inputs included in the database used to train the neural network.

10.3.2 The model

A database containing 26 points has been used to train 100 submodels. Models using up to 20 submodels in committee have been built. The optimum committee has been selected using a criterion of minimal combined the error in its predictions [112, 137, 113]. Figures 10.1, 10.2 and 10.3 show respectively the perceived level of noise in the models,

the test error and the log predictive test error with an increasing number of hidden units. Figure 10.4 shows the combined test error of the best committee built with an increasing number of submodels. The optimum committee in this case contains only one model.

Figures 10.5 and 10.6 show the performance of the best model on the training dataset and testing dataset. As it was expected, due to the small size of the database used to train the model, the errorbars in both plots are large. Notice that, the error estimations that correspond to the predictions done on unseen data are not substantially larger than those associated with the training set.

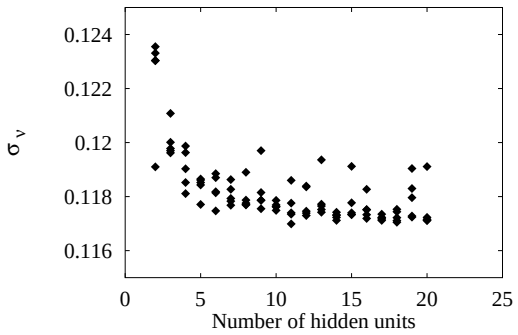

Figure 10.1: Perceived level of noise σ_ν with increasing number of hidden units.

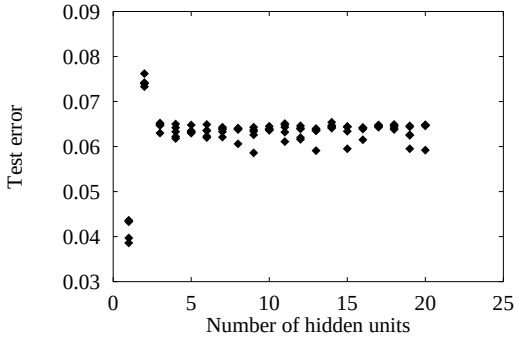

Figure 10.2: Test error with increasing number of hidden units.

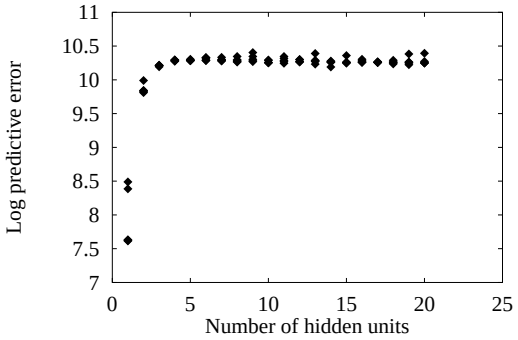

Figure 10.3: Log predictive error with increasing number of hidden units.

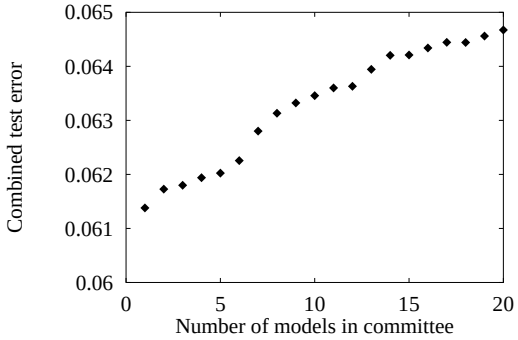

Figure 10.4: Combined test error for an increasing number of models in committee.

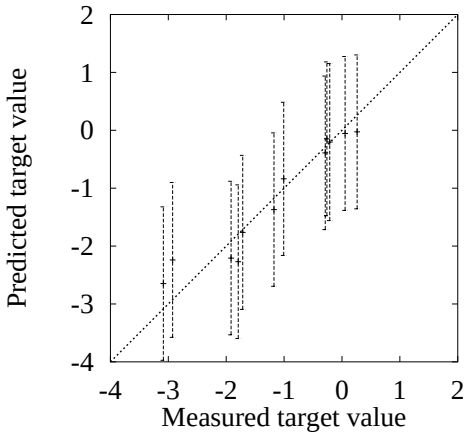

Figure 10.5: Performance of best model on already seen data (training set).

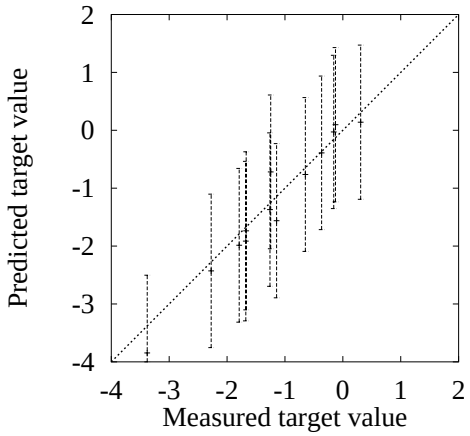

Figure 10.6: Performance of best model on unseen data (test set).

10.3.3 Significance of the input variables

During the training process of the neural network, the significance of each input parameter is inferred (Figure 10.7). In this case is clearly shown how the main contribution to the output is $1/T$, together with $\ln(t)$ and $Oven$. This is important, and it emphasises some of the strengths of a model based on an artificial neural network. Although the number of data used in the analysis is small, the model is able to differentiate between the oven and simulator tests. Finally, the input t is found not to be significant since $\ln(t)$ captures all of the effect of time, as expected from the Avrami equation.

10.4 Using the model to make predictions

The model trained on low tempering data has been interrogated to see if it is able to display the expected trends. Predictions to check the capability of the model to extrapolate beyond the area covered by the database have also been performed.

Predictions of the evolution of hardness with time at different temperatures are shown

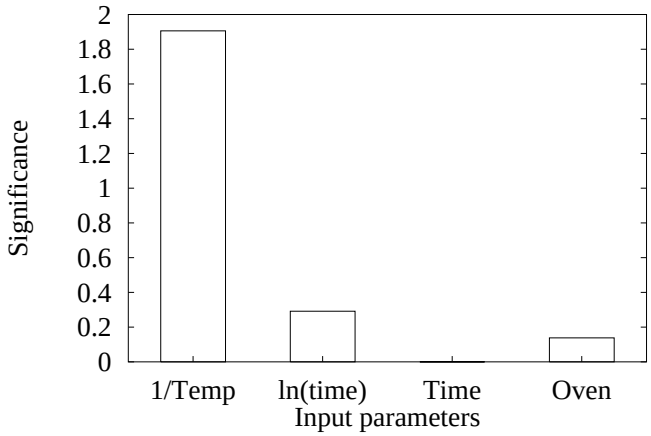

Figure 10.7: Perceived significance of each input parameter of the model on low temperature tempering

in Figures 10.8 to 10.17. The calculations of the evolution of tempering at low temperatures, up to 150°C present sensible results, and according to the error estimators (errorbars) the level of confidence is high. This confidence is reduced for the calculations for higher tempering temperature, but the model still shows the right trends and sensible values even when extrapolating to temperatures beyond the scope of the database. Only for very short tempering times and especially at low temperatures the predictions present surprising values, but the model correctly detects this and shows large uncertainties. This problem is expected because the experimental data from experiments with very short tempering time is not as accurate as the rest, because the time to achieve the steady tempering conditions is more that half of the total tempering time.

10.5 Determination of activation energy for tempering

It is reasonable to assume that during the first stages of tempering recovery or recrystallisation effects can be neglected, diffusion and precipitation of carbon dominating the evolution of hardness. Avrami type equations (equation 4.4) have previously been

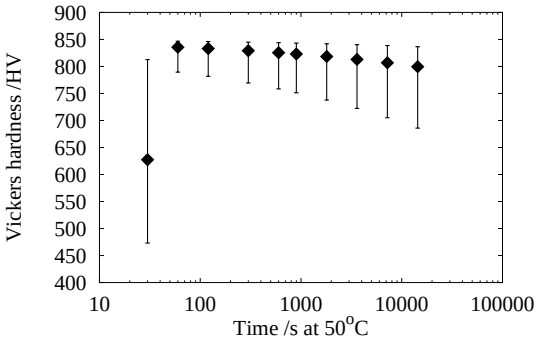

Figure 10.8: Prediction of evolution of hardness with time at 50°C.

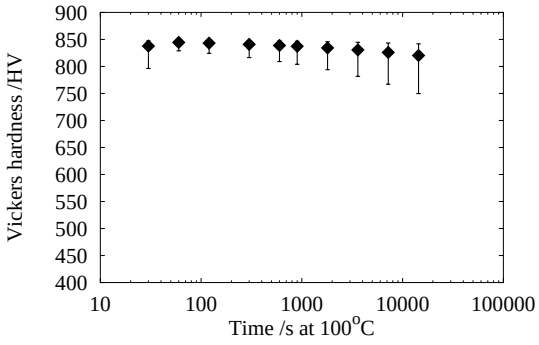

Figure 10.9: Prediction of evolution of hardness with time at 100°C.

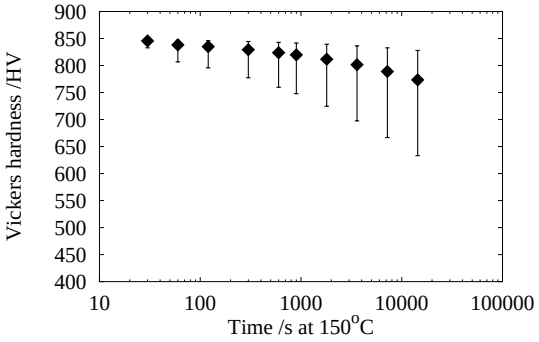

Figure 10.10: Prediction of evolution of hardness with time at 150°C.

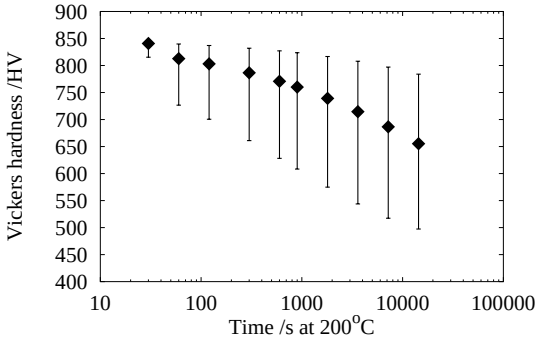

Figure 10.11: Prediction of evolution of hardness with time at 200°C.

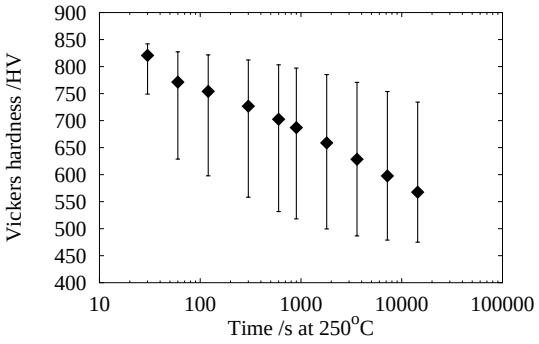

Figure 10.12: Prediction of evolution of hardness with time at 250°C.

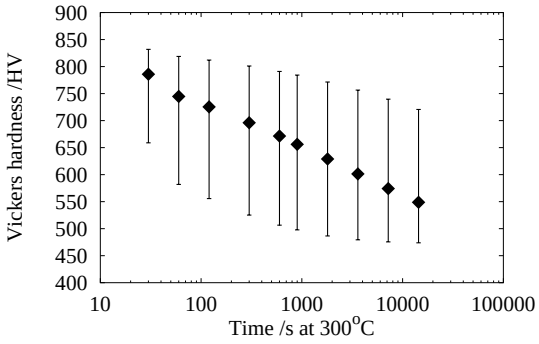

Figure 10.13: Prediction of evolution of hardness with time at 300°C.

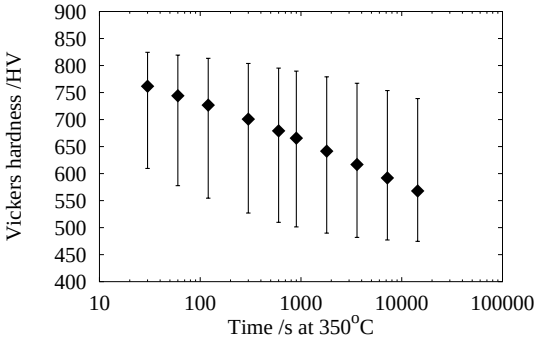

Figure 10.14: Prediction of evolution of hardness with time at 350°C.

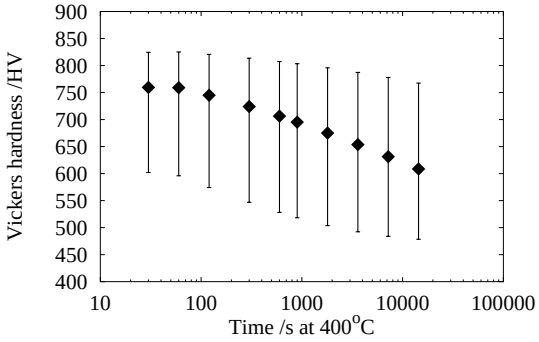

Figure 10.15: Prediction of evolution of hardness with time at 400°C.

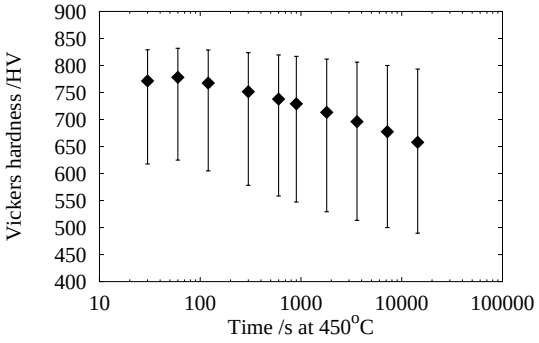

Figure 10.16: Prediction of evolution of hardness with time at 450°C.

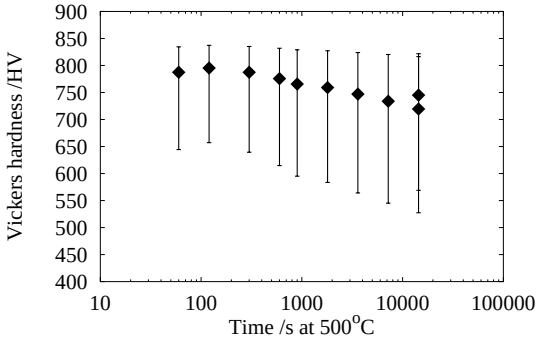

Figure 10.17: Prediction of evolution of hardness with time at 500°C.

applied to represent the evolution of some physical property like the electrical resistivity of martensite [101], or its hardness [108].

During the present study, the normalised hardness has been considered directly related to the volume fraction of carbide normalised to its equilibrium volume fraction. Classic kinetic theory [6] can be used to determine the volume fraction of carbide precipitated by using:

$$\xi\{T,t\} = 1 - \exp\left(-f\{T\}\, t^n\right) \tag{10.2}$$

where n is a rate constant and $f\{T\}$ is a function of temperature, including information of the nucleation and growth rates, and a geometric constant factor g characteristic of the shape of the precipitate.

$$f\{T\} = g\, I\, G^m \tag{10.3}$$

where m is a constant that, in a similar way as n, depends on the type of nucleation site and shape of the precipitates. I and G are the nucleation and growth rates respectively. Each one of them can be assumed to follow a function like:

$$F = F_0 \exp\left(-\frac{Q_F}{RT}\right) \tag{10.4}$$

where F is the nucleation (I) or growth (G) rate, F_0 is the respective pre-exponential constant, and Q_F is the activation energy for either nucleation (Q_I), or growth (Q_G). R is the gas constant and T the absolute temperature. If the nucleation rate were not a function of temperature, but adopt a constant value, $Q_I = 0$. Otherwise, as only carbon diffusion related phenomena are considered in this model, $Q_I \approx Q_G \approx Q_C$, with Q_C the activation energy for diffusion of carbon.

From equations 10.2 to 10.4 the following general equation yields:

$$\xi\{T,t\} = 1 - \exp\left(-gI_0G_0^{m'}\left(\exp(-\frac{m'Q}{RT})\right)t^n\right) \tag{10.5}$$

where $m' = m+1$ if the nucleation rate is thermally activated and $m' = m$ otherwise. If a function k of the type of equation 10.4 is defined, the previous equation can be rewritten as:

$$\xi\{T,t\} = 1 - \exp\left(-k^{m'}t^n\right) \tag{10.6}$$

in such case, k_0 would be:

$$k_0 = \sqrt[m']{gI_0G_0^m} \tag{10.7}$$

To fit the model presented above to experimental data, a tentative assumption about the value of n and m' has to be done. n can be determined from the experimental data, and for simplicity, $m' = n$ has been used.

Using the predictions calculated using the model shown in Section 10.4, the following linear regression can be determined for each temperature:

$$\ln\left(-\ln\left(1-\xi\{T,t\}\right)\right) = n\ln k + n\ln t \tag{10.8}$$

If $\ln k$ for each temperature is plotted against $\frac{1}{T}$ Figure 10.18 (Figure 10.19 shows $\ln k$ plotted against T, which might be easier to read) is obtained. The use of the point corresponding to 50°C should be considered with caution, because is based in only one point in the database, and the prediction presents large uncertainty. If this point is overlooked, two distinct regions can be identified, which meet at 300°C. Below that temperature all the phenomena occurring during tempering probably involve exclusively the diffusion of carbon and formation of carbides. Above that temperature phenomena such as carbide coarsening, grain growth, recovery of the structures of defects like dislocations and recrystallisation. Besides, the database used to train the database contains only information

from the first stage of tempering. A straight line has been fitted by linear least squares regression to the points of Figure 10.18 between 50 and 300°C and from the slope of the line obtained (10.4), the activation energy for tempering can be determined to be $Q = 8.8 \cdot 10^4\,\mathrm{J\,mol^{-1}}$.

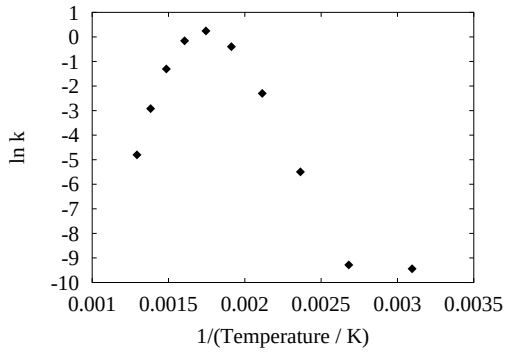

Figure 10.18: Regression to determine the activation energy for tempering of martensite

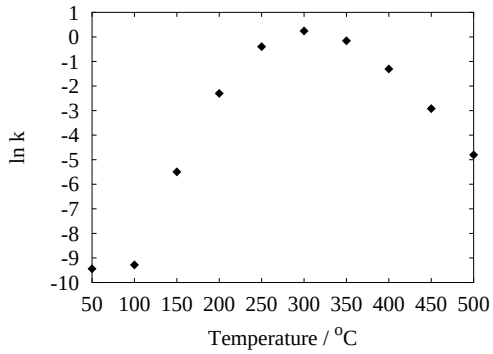

Figure 10.19: Regression to determine the activation energy for tempering of martensite

10.6 Activation energy for diffusion of carbon in α'

All the phenomena taking place in the stages of tempering occurring at lowest temperatures involve the diffusion of carbon atoms from their martensite octahedral sites to defects and towards the precipitation of carbides. It is expected therefore that the activation energy measured experimentally should relate to that for the diffusion of carbon in martensite.

Diffusion of carbon in ferrite involves elementary jumps of carbon atoms from one to another of several types of available sites. On the transformation to martensite the basal octahedral sites and the tetragonal sites become too small to accommodate a carbon atom and only the remaining octahedral sites can be used. Non-basal octahedral interstices are actually expanded, but a carbon atom jumping from one of these octahedral sites to a neighbouring one needs to perform an intermediate step into one of the contracted

tetragonal sites [165]. As that implies a larger energy barrier, diffusion of carbon in martensite is slower that in ferrite [165]. The actual diffusion coefficient of carbon in martensite $D_{\alpha\prime}$ can be determined relative to that in ferrite D_α following Hillert [165], as:

$$D_{\alpha\prime} = D_\alpha \exp\left(-\frac{N_a U_c}{2RT}\right) \tag{10.9}$$

where N_a is the Avogadro number, U_c is the the energy in Joules needed to move a carbon atom to one of its neighbouring site in martensite, that can be determined as a function of the atomic carbon composition x_C as follows [166]:

$$U_c = 9.9 \cdot 10^{-19} x_C \tag{10.10}$$

Iijima has determined the diffusion coefficient of carbon in $\mathrm{m\,s^{-2}}$ in ferrite as [167]:

$$D_\alpha = 2.72 \cdot 10^{-7} \exp\left(-5.96 \cdot 10^{-4} \frac{1 + 0.337 s^2}{RT}\right) \tag{10.11}$$

where s is the ratio of the spontaneous magnetisation in iron at T K to that at 0 K. At the range of temperatures considered s is very close to unity [168].

By using equations 10.9 to 10.11, $s = 0.96$ [168] and assuming that the diffusion coefficient of carbon in martensite takes the form of an Avrami equation (10.4), the activation energy for diffusion of carbon in martensite at 200°C is determined to be $Q_C = 8.6 \cdot 10^4 \mathrm{J\,mol^{-1}}$.

In a previous section 10.5, the activation energy for tempering has been determined as $Q = 8.8 \cdot 10^4\,\mathrm{J\,mol^{-1}}$ from predictions done using a neural network model trained on experimental data. The value of the activation energy for tempering determined in that section is almost the same as the activation energy for diffusion of carbon in martensite.

10.7 Conclusions

A small set of experimental data has been used to create a model on low temperature tempering. Low temperature tempering is considered to include only the range of temperatures in which only diffusion and precipitation related phenomena occur, excluding recovery and recrystallisation. The model is based on an Avrami reaction rate equation implemented by training an artificial neural network on the experimental data. The activation energy for tempering has been determined from predictions calculated using the model and the value found is very close to the activation energy for diffusion of carbon in martensite. This result is taken to prove that an advanced neural network can be used to implement a physically sound model.

Chapter 11

Summary and suggestions for future work

11.1 Application to a process

The aim of this section is to show how the work presented in previous chapters could be applied to the constant velocity joint manufacturing process. Specifically, it is the shaft of the outer race bell of a constant velocity joint that is considered. This shaft is basically a cylinder of radius $R = 12$ mm. A section of the manufactured shaft is shown later in figure 11.6.

The general manufacturing process has been described in Chapter 1. The determining features of the final microstructure are induction hardening and tempering. After warm forging the component is normalised, producing a starting microstructure composed of ferrite and pearlite. The composition of the steel and details of its microstructure are listed in Tables 11.1 and 11.2 respectively. The component is cold forged prior to induction hardening, but this is neglected for reasons described in Chapter 8.

wt.%	**C**	**Si**	**Mn**	**Cr**	**Ni**	**Mo**	**V**
Steel C	0.55	0.23	0.79	0.19	0.13	0.03	0.002

Table 11.1: Composition of steel used in the calculations, presenting typical composition used in manufacturing processes involving induction hardening.

	$2l_\alpha$ /m	$2l_p$ /m	l_e /m	l_{col} /m
Steel C	1.8×10^{-6}	6.19×10^{-6}	0.4×10^{-6}	18×10^{-6}

Table 11.2: Microstructure of steel used for the calculations, characterised in terms of the parameters l_α, l_p, l_{col} and l_e, as defined previously.

The aim of induction hardening is to create an outer case which is essentially martensite, encasing a ferrite and pearlite core. The intended thickness of the martensite layer is 3-4 mm [2]. Induction hardening takes only about 5 s. The austenite grain size is assumed to be 20 μm. After hardening, the component is tempered to increase the toughness of the martensite case, heating to 175°C for 90 min [2]. The required surface hardness is

650-750 HV [2].

11.1.0.1 Temperature evolution during induction hardening

The temperature cycle during induction hardening has been calculated using the finite difference integration of the heat equation presented in Chapter 6. The input parameters used for these calculations are summarised in Table 11.3.

Density	$7.8 \cdot 10^3\,\mathrm{kg\,m^3}$
Specific heat	$600\,\mathrm{J\,kg^{-1}\,K^{-1}}$
Start temperature	18°C
Water temperature	18°C
Maximum temperature	1400°C
Target temperature	1050°C
Induction input heat flux	$5 \cdot 10^5\,\mathrm{W\,m^{-1}}$
Heat transfer: Air	$6\,\mathrm{W\,m^{-1}}$
Heat transfer: Water sprays	$35 \cdot 10^3\,\mathrm{W\,m^{-2}\,K^{-1}}$
Dead time	0.25 s

Table 11.3: Input parameters used by the temperature cycle model

The results of these calculations showing the temperature profiles at four different positions in the shaft are presented in figure 11.1. Positions are measured from the centre of the cylinder, that is, $R = 0$ mm is the centre and $R = 12$ mm corresponds to the surface. Two other positions are shown, $R = 8$ mm and $R = 10$ mm. The transition between the hardened layer and the core, containing mostly ferrite and pearlite, should lie between these two positions.

11.1.0.2 Phase transformations during induction hardening

The models presented in Chapters 7 and 9 have been used to determine the transformations occurring at various positions in the component during induction hardening. The

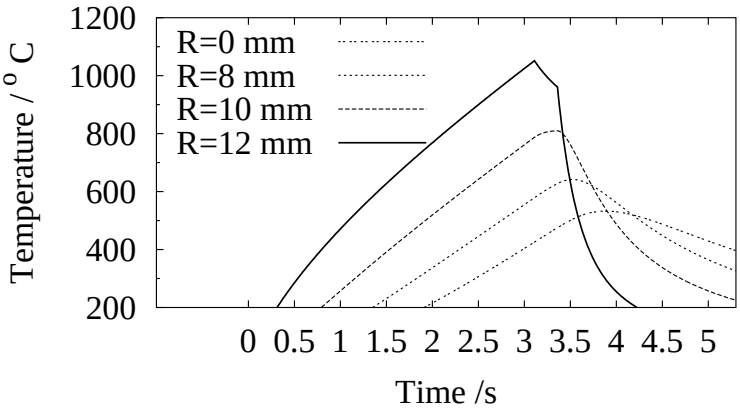

Figure 11.1: Temperature evolution during induction hardening at four positions in the shaft.

evolution of the microstructure is shown in figures 11.2 to 11.5, together with the thermal cycle, at each of those positions.

According to these calculations, the transition between the hard case and the softer core lies between 2 and 4 mm from the surface. The core region never reaches the temperature needed to form austenite, and retains the ferrite-pearlite microstructure (figures 11.4 and 11.5). Close to the surface of the shaft, there is a region in which the temperature has been enough to partially or totally austenitise the alloy, with subsequent transformation into martensite but leaving behind some retained austenite and untransformed phases (ferrite and pearlite). Figures 11.2 and 11.3 correspond to this region.

11.1.0.3 Hardness prediction after tempering

Once the microstructure of the component has been determined, the final hardness of the martensite case after low temperature tempering can be predicted using the neural network model presented in Chapter 10. The tempering conditions considered are 90 minutes (5400 s) in an oven at 175°C. After interrogating the model, a final hardness of

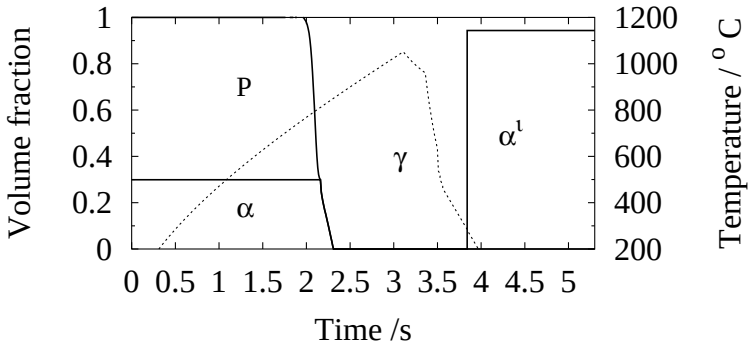

Figure 11.2: Calculated evolution of the microstructure at the surface of the shaft ($R =$ 12 mm) during induction hardening and the corresponding temperature cycle. α represents ferrite, P pearlite, γ austenite (including retained austenite) and α' martensite. Dotted line corresponds to temperature.

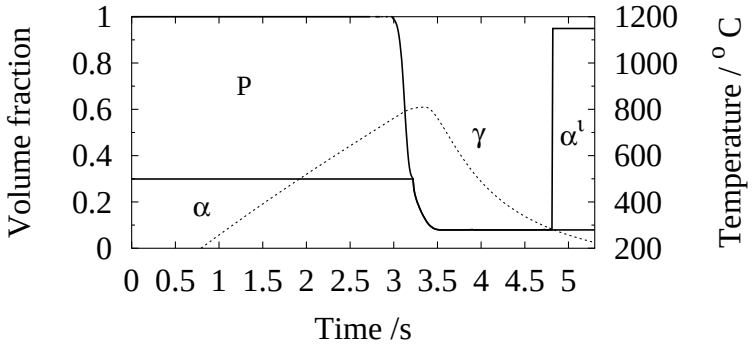

Figure 11.3: Calculated evolution of the microstructure at position $R = 10$ mm in the shaft during induction hardening and the corresponding temperature cycle. α represents ferrite, P pearlite, γ austenite (including retained austenite) and α' martensite. Dotted line corresponds to temperature.

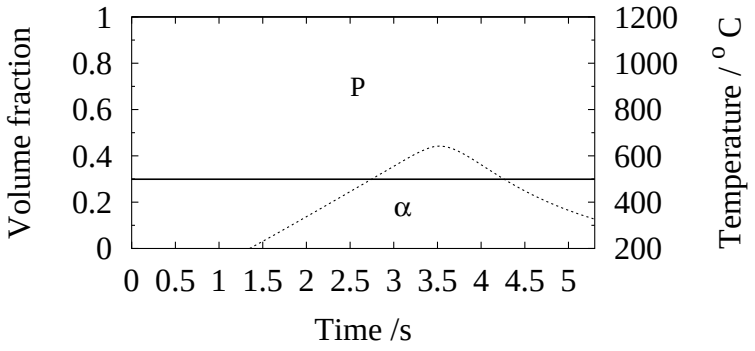

Figure 11.4: Calculated evolution of the microstructure at position $R = 8$ mm in the shaft during induction hardening and the corresponding temperature cycle. α represents ferrite, P pearlite. Dotted line corresponds to temperature.

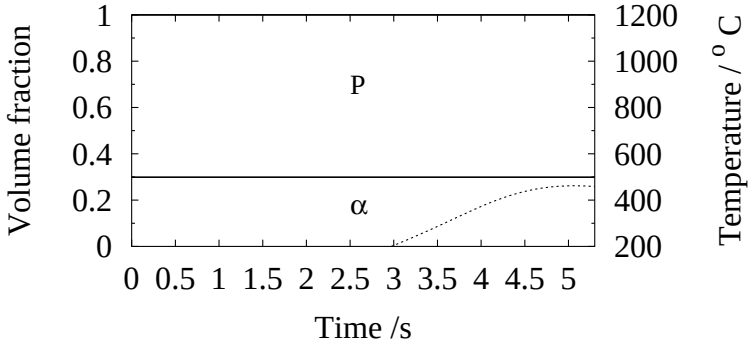

Figure 11.5: Calculated evolution of the microstructure at the centre of the shaft ($R = 0$ mm) during induction hardening and the corresponding temperature cycle. α represents ferrite, P pearlite. Dotted line corresponds to temperature.

the tempered martensite of 716 HV with a confidence level equivalent of one standard deviation [137, 113] within the range 704 to 726 HV is predicted.

11.1.0.4 Discussion and conclusions

Figure 11.6 shows the section of the shaft of an outer race bell that has been taken as example to compare the results of the model with a real component. The precise characteristics of manufacturing process of this shaft may not be exactly the same ones considered when using the model, but are certainly similar, and the dimensions, composition and microstructure of this component have been used in the calculations.

The accuracy of the microstructure prediction is remarkable. The sample presents a sharp change in microstructure at approximately 4 mm from the surface, as the model predicts. Vickers hardness measures close to the surface of the shaft give 705 HV with a standard deviation $\sigma = 5$ HV. The hardness of the (tempered) martensite case predicted by the model is in good agreement with this value.

11.2 Summary of the present work

Considerable work has been published on modelling the kinetics of isolated phase transformations. This sort of research has increased the understanding of the phenomena involved and of the parameters which influence transformations. Studies involving many simultaneous transformations as in real processes are, however, scarce. It is often the case that simple models dealing with individual transformations are poor representations of industrial problems. Models designed for manufacturing applications have to find the right compromise between accuracy, robustness and applicability.

The aim of the present work was the study of the phase transformations involved during the manufacture of certain steel components for the automotive industry, and the creation of a comprehensive model incorporating classic and novel phase transformation theory, in

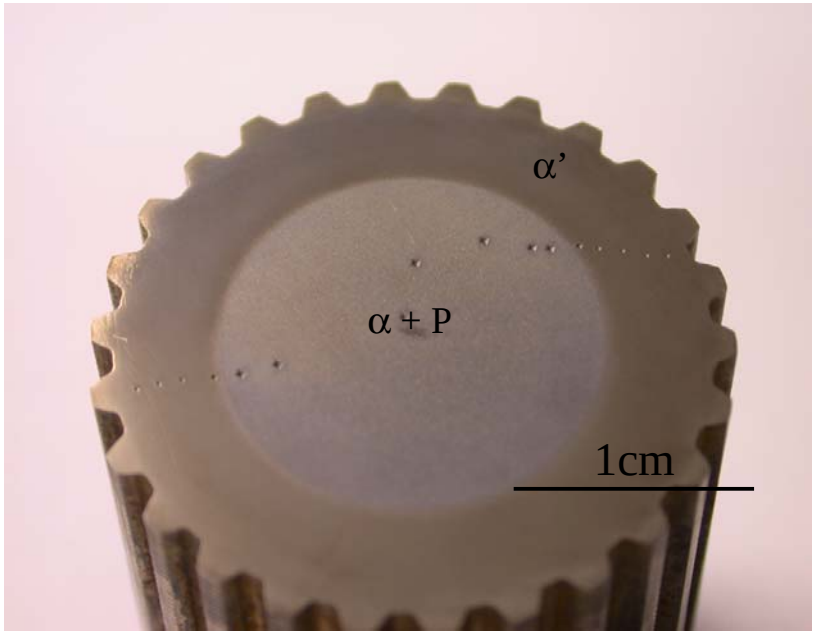

Figure 11.6: Section of the shaft of an outer bell race of similar characteristics to the example used with the model. The subsurface region with dark contrast presents a microstructure composed mostly of martensite, and the lighter core presents a microstructure formed by ferrite and pearlite. α represents ferrite, P pearlite and α' martensite. The hardness of the martensite case is 705 HV $\sigma = 5$ HV.

the context of induction hardening. The whole process has been studied and the effects of each of its stages on the phase transformation behaviour of the steel considered. However, an entirely modular approach has been adopted. The reasoning behind this decision was to achieve transparency even when the complexity of the overall model increases. At the same time a modular design has flexibility if modifications are necessary.

One of the vital inputs needed during the study of phase transformations is the temperature history of the alloy. Although that information can in principle be gathered experimentally, the first module of the model consists on a finite difference integration of the heat equation applied to induction hardening. This program allows the calculation of precise thermal cycles for several simple symmetries.

The austenitisation of hypoeutectoid steels with a pearlite/ferrite microstructure has been studied, as a function of composition and starting microstructure. It uses classical theory to determine the nucleation of austenite at the edges of pearlite colonies, and diffusion of carbon is assumed to limit the rate of transformation. The morphology of austenite growth into a pearlite colony is taken into account, as it is for the transformation of allotriomorphic ferrite. This model may not only be used for the purpose of process optimisation, but also to study the effect of different microstructure and composition parameters and heat cycle on austenitisation.

The effect of heating rate, prior deformation, and prior heat treatments on austenitisation of hypoeutectoid steels has been characterised. The kinetics of transformation are enhanced by prior deformation, as is the rate of spheroidisation of cementite. For annealed steels or slow heating rates, especially when the alloy has been cold-worked, lamellar pearlite-cementite may spheroidise. The rate of austenitisation from a microstructure containing a mixture of ferrite and spheroidised cementite is slower than from a mixture of lamellar pearlite and ferrite. In absence of spheroidisation annealing, and if the heating rate is large enough, austenite forms directly from lamellar pearlite. The combination of effects gives rise to a heating rate at which austenitisation occurs fastest. Due to the high heating rates involved in induction hardening there has not been the need to include this effect in the austenitisation model.

A model able to calculate the key transformation products of the decomposition of austenite during continuous cooling has been assembled. It integrates previous models by Robson, Bhadeshia and others dealing with simultaneous transformations and includes for the first time, the bainite reaction. This model is especially suitable for the calculation of continuous cooling diagrams.

The evolution of hardness during tempering at temperatures at which no substantial recovery or recrystallisation is expected has been studied experimentally. A small though accurate database has been gathered and used to train a semiempirical model based on an Avrami reaction rate equation but implemented using an artificial neural network. It has been assumed that at the temperature range considered only phenomena related to the diffusion of carbon and precipitation of carbides occurs. The activation energy for tempering has been calculated from the predictions made by the neural network model, and it has been found to be very close to that for the diffusion of carbon in martensite, establishing the ability of a sophisticated non-linear regression technique like artificial neural networks to grasp accurately the trends of physical phenomena given good experimental data.

In summary, all the parameters involved in the phase transformations occurring during a manufacturing process involving forming, induction hardening and tempering have been characterised and a set of models has been created that is suitable to make predictions on the evolution of the microstructure during the process.

11.3 Suggestions for future work

Although the aim of the research project behind this thesis has been already fulfilled with the work presented there are some aspects that could lead to thrillingly interesting research lines and to serious improvements in the models presented.

The spheroidisation of cementite prior to austenitisation should be characterised, and its dependence with the prior microstructure, prior deformation and thermal cycle de-

termined. Such information could then be incorporated into the austenitisation model already presented here. In fact, if the austenitisation of a mixture of spheroidised cementite and pearlite is also considered, the austenitisation model can be extended to cover all the range of iron, steel and cast irons. Including the effects of chemical composition, initial microstructure, deformation levels and thermal history would make it a comprehensive model for austenitisation of steel for all circumstances.

The models presented for the decomposition of austenite during cooling should be implemented in such a way that more flexible heat treatments could be studied. The model presented here converts any cooling curve to two constant cooling rates for the temperature ranges involving respectively reconstructive and displacive reactions. A tighter integration with the heat flow submodel would also open the possibility of considering the effect of the latent heat of transformation, which has been neglected in the present models.

Once it has been proven the suitability of a neural network implementation of a physically based approach to tempering, the effect of chemical composition in substitutional elements should be studied.

Bibliography

[1] G. E. Hollox. It started with the Mini. *Materials World*, 10:16–19, 2002.

[2] G. Hollox, N. Hurd, I. Capewell, J. Garnham, M. Dalton, M. Harvey, W. Beigang, R. J. Salomon, and J. Dimmock. ICE course, GEP 105. Materials, processing and performance. Technical report, GKNT, 1999.

[3] S. M. Hodson. *MTDATA–Metallurgical and Thermochemical Databank.* National Physical Laboratory, Teddington (UK), 1989.

[4] D. A. Porter and K. E. Easterling. *Phase transformations in metals and alloys.* Chapman & Hall, London, 1981.

[5] N. Saunders and A. P. Miodownik. *CALPHAD, calculation of phase diagrams, a comprehensive guide.* Pergamon Press, Oxford, 1998.

[6] J. W. Christian. *Theory of transformations in metals and alloys, Part I.* Pergamon Press, Oxford, 1975.

[7] A. N. Kolmogorov. Statistical theory of metallic crystallisation. *Izvestia Akademii Nauk USSR-Ser-Matemat.*, 1(3):355–359, 1937.

[8] W. A. Johnson and R. F. Mehl. Reaction kinetics in processes of nucleation and growth. *Transactions of the A.I.M.E.*, 135:416–458, 1939.

[9] M. Avrami. Kinetics of phase change. I. *Journal of Chemical Physics*, 7:1103–1112, 1939.

[10] M. Avrami. Kinetics of phase change. II. *Journal of Chemical Physics*, 8:212–224, 1940.

[11] M. Avrami. Kinetics of phase change. III. *Journal of Chemical Physics*, 9:177–184, 1941.

[12] J. D. Robson and H. K. D. H. Bhadeshia. Modelling precipitation sequences in power plant steels. Part 1 - Kinetic theory. *Materials Science and Technology*, 13:631–639, 1997.

[13] J. D. Robson and H. K. D. H. Bhadeshia. Modelling precipitation sequences in power plant steels. Part 2 - Application of kinetic theory. *Materials Science and Technology*, 13:640–644, 1997.

[14] S. J. Jones and H. K. D. H. Bhadeshia. Kinetics of the simultaneous decomposition of austenite into several transformation products. *Acta Materialia*, 45:2911–2920, 1997.

[15] M. P. Puls and J. S. Kirkaldy. The pearlite reaction. *Metallurgical Transactions*, 3:2777–2796, 1972.

[16] D. P. Koistinen and R. E. Marburger. A general equation prescribing the extent of the austenite-martensite transformation in pure iron-carbon alloys and plain carbon steels. *Acta Metallurgica*, 7:59–60, 1959.

[17] C. L. Magee. Nucleation of martensite. In *Phase transformations*, pages 115–156. ASM, Ohio, 1970.

[18] E. Scheil. Anlaufzeit der Austenitumwandlung. *Archiv für das Eisenhüttenwessen*, 8:565–567, 1935.

[19] R. A. Grange and J. M. Kiefer. Transformation of austenite on continuous cooling and its relation to transformation at constant temperature. *Transactions of the A.S.M.*, 29:85–116, 1941.

[20] Z. Zhang and R. A. Farrar. *An atlas of continuous cooling transformation (CCT) diagrams applicable to low carbon low alloy weld metals.* The Institute of Materials, Bournemouth, UK, 1995.

[21] T. Kunitake and H. Ohtani. Calculating the continuous cooling diagram of steel from its chemical composition. *The Sumitomo Search*, 2:18–21, 1969.

[22] M. Inagaki and H. Sekiguchi. Continuous cooling transformation diagrams of steels for welding and their applications. *Transactions of National Research Institute for Metals*, 2:102–125, 1960.

[23] J. C. Ion, K. E. Easterling, and M. F. Ashby. Diagrams of microstructure and hardness for HAZ's in welds. *Acta Metallurgica*, 32:1949–1962, 1984.

[24] J. Wang, P. J. Wolk, and S. Zwaag. Effects of carbon concentration and cooling rate on continuous cooling transformations predicted by artificial neural network. *ISIJ International*, 39:1038–1046, 1999.

[25] H. K. D. H. Bhadeshia. Thermodynamic analysis of isothermal transformation diagrams. *Metal Science*, 16:159–165, 1982.

[26] K. C. Russell. Grain boundary nucleation kinetics. *Acta Metallurgica*, 17:1123–1131, 1969.

[27] M. Hillert. *Lectures on the theory of transformations*, pages 1–50. ed. Aaronson, H.I., The Metallurgical Society of AIME, New York, 1975.

[28] H. I. Aaronson, H. A. Domian, and G. M. Pound. Thermodynamics of the austenite - proeutectoid ferrite transformation. I, Fe-C alloys. *Transactions of the Metallurgical Society of A.I.M.E.*, 236:753–767, 1966.

[29] H. I. Aaronson, H. A. Domian, and G. M. Pound. Thermodynamics of the austenite - proeutectoid ferrite transformation. II, Fe-C-X alloys. *Transactions of the Metallurgical Society of A.I.M.E.*, 236:768–781, 1966.

[30] A. M. Pokrovskii and V. G. Leshkovstsev. Computational determination of the structure and hardness of rolls after induction hardening. *Metal Science and Heat Treatment*, 39:396–400, 1997.

[31] A. Bokota and S. Iskierda. Numerical analysis of phase transformations and residual stresses in steel cone-shaped elements hardened by induction and flame methods. *International Journal of Mechanical Sciences*, 40:617–629, 1998.

[32] M. Melander. Computer predictions of progressive induction hardening of cylindrical components. *Materials Science and Technology*, 1:877–882, 1985.

[33] S. Sjöström. Interactions and constitutive models for calculating quench stresses in steel. *Materials Science and Technology*, 1:823–829, 1985.

[34] Y. Nagasaka, J. K. Brimacombe, E. B. Hawbolt, I. V. Samarasekera, B. Hernandez-Morales, and S. E. Chidiac. Mathematical model of phase transformations and elasto-plastic stress in the water spray quenching of steel bars. *Metallurgical Transactions A*, 24A:795–808, 1993.

[35] T. Inoue and B. Raniecki. Determination of thermal-hardening stress in steels by use of thermoplasticity theory. *Journal of Mechanics and Physics of Solids*, 26:187–212, 1978.

[36] D.H. Xu, Z.H. Li, and J.X. Luo. Expressions for predicting the residual stress in surface induction of steel bars. *Modelling and Simulation in Materials Science and Engineering*, 4:111–122, 1996.

[37] P. K. Agarwal and J. K. Brimacombe. Mathematical model of heat flow and austenite - pearlite transformation in eutectoid carbon steel rods for wire. *Metallurgical Transactions B*, 12B:121–133, 1981.

[38] J-B. Leblond, G. Mottet, J. Devaux, and J-C. Devaux. Mathematical models of anisothermal phase transformations in steels, and predicted plastic behaviour. *Materials Science and Technology*, 1:815–822, 1985.

[39] D. H. Xu and Z. B. Kuang. A study on the distribution of residual stress due to surface induction hardening. *Journal of Engineering Materials and Technology -Transactions of the ASME*, 118:571–575, 1996.

[40] S. Jahanian. Thermoelastoplastic and residual stress analysis during induction hardening of steel. *Journal of Engineering and Performance*, 4:737–744, 1995.

[41] J. Fuhrmann, D. Homberg, and M. Uhle. Numerical simulation of induction hardening of steel. *COMPEL- The International Journal for Computation and Mathematics in Electrical and Electronics Engineering*, 18:482–493, 1999.

[42] J-B. Leblond and J. Devaux. A new kinetic model for anisothermal metallurgical transformations in steels including the effect of austenite grain size . *Acta Metallurgica*, 32:137–146, 1985.

[43] H. K. D. H. Bhadeshia and D. V. Edmonds. Bainite in silicon steels: new composition-property approach. Part 1. *Metals Science*, 17:411–419, 1983.

[44] G. A. Roberts and R. F. Mehl. The mechanism and the rate of formation of austenite from ferrite-cementite aggregates. *Transactions of the A.S.M.*, 31:613–650, 1943.

[45] C. R. Brooks. *Principles of the austenitization of steels.* Elsevier Applied Science, London, 1992.

[46] G. R. Speich, A. Szirmae, and M. J. Richards. Formation of austenite from ferrite and ferrite-carbide aggregates. *Transactions of the Metallurgical Society of A.I.M.E.*, 245:1063–1074, 1969.

[47] A. Roòsz, Z. Gácsi, and E. G. Fuchs. Isothermal formation of austenite in eutectoid plain carbon steel. *Acta Metallurgica*, 31:509–517, 1983.

[48] N. C. Law and D. V. Edmonds. The formation of austenite in low-alloy steels. *Metallurgical Transactions A*, 11A:33–46, 1980.

[49] R. Kaspar, A. Streisselberger, and O. Pawelski. Einfluss der thermomechanisschen Behandlung auf die Austenitbildung bei der Rückumwandlung des Martensits eines Vergütungsstahls. *Zeitschrift fur Metallkunde*, 76:657–661, 1985.

[50] H. Kessler and W. Pitsch. On the nature of the martensite to austenite reverse transformation. *Acta Metallurgica*, 15:401–405, 1967.

[51] A. Ali and H. K. D. H. Bhadeshia. The reverse transformations in a high-strength high-hardenability Fe-C-Mn-Mo steel. *Journal of Materials Science*, 28:3137–3144, 1993.

[52] J. R. Yang and C. Y. Huang. Formation of austenite from a mixture of bainitic ferrite and austenite. *Materials Chemistry and Physics*, 35:168–175, 1993.

[53] L. Gavard, H. K. D. H. Bhadeshia, D. J. C. MacKay, and S. Suzuki. Bayesian neural network model for austenite formation in steels. *Materials Science and Technology*, 12:453–463, 1996.

[54] J. R. Yang and H. K. D. H. Bhadeshia. Reaustenitization experiments on some high-strength steel weld deposits. *Materials Science and Engineering A*, A118:155–170, 1989.

[55] R. C. Reed, Z. Shen, T. Akbay, and J. M. Robinson. Laser-pulse heat treatment: Aplication to reaustenitisation from ferrite/cementite mixtures. *Materials Science and Engineering A*, A232:140–149, 1997.

[56] C. I. Garcia and A. J. Deardo. Formation of austenite in 1.5 pct Mn steels. *Metallurgical transactions A*, 12A:521–530, 1981.

[57] R. A. Grange. Effect of microstructural banding in steels. *Metallurgical Transactions*, 2:417–426, 1971.

[58] R. D. Knutsen. Influence of compositional banding on grain anisotropy in 3CR12 steel. *Materials Science and Technology*, 8:621–627, 1992.

[59] F. G. Caballero, C. Capdevila, and C. García de Andrés. Influence of scale parameters of pearlite on the kinetics of anisothermal pearlite-to-austenite transformation in a eutectoid steel. *Scripta Materialia*, 42:1159–1165, 2000.

[60] A. S. Oddy, J. M. J. McDill, and L. Karlsson. Microstructural predictions including arbitrary thermal histories, reaustenization and carbon segregation effects. *Canadian Metallurgical Quarterly*, 35:275–283, 1996.

[61] T. Akbay, R. C. Reed, and C. Atkinson. Modelling reaustenitisation from ferrite/cementite mixtures in Fe-C steels. *Acta Metallurgica et Materialia*, 47:1469–1480, 1994.

[62] C. Atkinson, T. Akbay, and R. C. Reed. Theory for reaustenitisation from ferrite/cementite mixtures in Fe-C-X steels. *Acta Metallurgica Materialia*, 43:2013–2031, 1995.

[63] T. Akbay and C. Atkinson. The influence of diffusion of carbon in ferrite as well as in austenite on a model of reaustenitization from ferrite/cementite mixtures in Fe-C steels. *Journal of Materials Science*, 31:2221–2226, 1996.

[64] T. Akbay and C. Atkinson. The influence of diffusion of carbon in ferrite as well as in austenite on a model of reaustenitization from ferrite/cementite mixtures in Fe-C steels. *Journal of Materials Science*, 31:5004, 1996.

[65] C. Atkinson and T. Akbay. The effect of the concentration-dependent diffusivity of carbon in austenite on a model of reaustenitisation from ferrite/cementite mixtures in Fe-C steels. *Acta Materialia*, 44:2861–2868, 1996.

[66] A. Jacot and M. Rappaz. A two-dimensional model for the prediction of phase transformations: application to austenitization and homogeneization of hypoeutectoid Fe-C steels. *Acta Materialia*, 45:575–585, 1997.

[67] A. Jacot, M. Rappaz, and R. C. Reed. Modelling of reaustenitization from the pearlite structure in steel. *Acta Materialia*, 46:3949–3962, 1998.

[68] A. Jacot and M. Rappaz. A combined method for the description of austenitization, homogeneization and grain growth in hypoeutectoid Fe-C steels during heating. *Acta Materialia*, 47:1645–1651, 1999.

[69] R. Mancini and C. Budde. Reaustenitisation in Fe-C revisited. *Acta Materialia*, 47:2907–2911, 1999.

[70] C. A. L. Bailer-Jones, H. K. D. H. Bhadeshia, and D. J. C. MacKay. Gaussian process modelling of austenite formation in steel. *Materials Science and Technology*, 15:287–294, 1999.

[71] M. Ukemoto, H. Ohtsuka, and I. Tamura. Transformation to pearlite from work-hardened austenite. *Transactions ISIJ*, 23:775–784, 1983.

[72] D. J. Walker and R. W. K. Honeycombe. Effects of deformation on decomposition of austenite: Part I-The ferrite reaction. *Metal Science*, 14:445–452, 1978.

[73] D. J. Walker and R. W. K. Honeycombe. Effects of deformation on decomposition of austenite: Part II-Carbide precipitation. *Metal Science*, 16:184–188, 1980.

[74] S. B. Singh. *Phase transformations from deformed austenite.* PhD thesis, University of Cambridge. Department of Materials Science and Metallurgy, Cambridge, 1998.

[75] S. B. Singh and H. K. D. H. Bhadeshia. Quantitative evidence for mechanical stabilisation of bainite. *Materials Science and Technology*, 12:610–612, 1996.

[76] P. H. Shipway and H. K. D. H. Bhadeshia. The effect of small stresses on the kinetics of the bainite transformation. *Materials Science and Engineering A*, A201:143–149, 1995.

[77] T. C. Lei and J. Pan. Kinetics of Austenitization During Intercritical Annealing of Low Carbon Low Alloy Steels. In *HSLA Steels: Metallurgy and Applications; ASM International*, pages 823–830, 1986.

[78] M. Tokizane, K. Matsumura, N. Tsuzaki, T. Maki, and I. Tamura. Recrystalization and formation of austenite in deformed lath martensitic structure of low carbon steels. *Metallurgical Transactions A*, 13A:1379–1388, 1982.

[79] J. Toribio and E. Ovejero. Microstructure evolution in a pearlitic steel subjected to progressive plastic deformation. *Materials Science and Engineering*, A234-236:579–582, 1997.

[80] S. B. Singh and H. K. D. H. Bhadeshia. Topology of grain deformation. *Materials Science and Technology*, 14:832–834, 1998.

[81] J. D. Embury and R. M. Fisher. The structure and properties of drawn pearlite. *Acta Metallurgica*, 14:147–159, 1966.

[82] J. Gil Sevillano. Room temperature plastic deformation of pearlitic cementite. *Materials Science and Engineering*, 21:221–225, 1975.

[83] G. Langford. Deformation of pearlite. *Metallurgical Transactions A*, 8A:861–875, 1977.

[84] S. Chattopadhyay and C. M. Sellars. Quantitative measurements of pearlite spheroidization. *Metallography*, 10:89–105, 1977.

[85] D. Hernández-Silva, R. D. Morales, and J. G. Cabañas-Moreno. The spheroidization of cementite in a medium carbon steel by means of subcritical and intercritical annealing. *ISIJ International*, 32(12):1297–1305, 1992.

[86] S. Chattopadhyay and C. M. Sellars. Kinetics of pearlite spheroidisation during static annealing and during hot deformation. *Acta Metallurgica*, 30:157–170, 1982.

[87] L. Weijuan, Z. Hongmei, D. Linxiu, L. Xianghua, and W. Guodong. Influence of moderate temperature processing on microstructure of low carbon steel. *Research in Iron and Steel*, Sept.-Oct.:44–47, 2000.

[88] A. V. Korznikov, Yu.V. Ivanisenko, D. V. Laptionok, I. M. Safarov, V. P. Pilyugin, and R. Z. Valiev. Influence of severe plastic deformation on structure and phase composition of carbon steel. *NanoStructured Materials*, 4(2):159–167, 1994.

[89] F. S. Buffington, K. Hirano, and M. Cohen. Self diffusion in iron. *Acta Metallurgica*, 9:434–439, 1961.

[90] R. Fougères, M. Théolier, L. Peeters, and G. Vella. Traitements mécanothermiques de courte durée. Application au tréfilage des aciers eutectoïdes. *Mémoires et Études Scientifiques Revue de Métallurgie*, January:25–36, 1981.

[91] M. H. Hong, W. T. Reynolds Jr., T. Tarui, and K. Hono. Atom probe and transmission electron microscopy investigations of heavily drawn pearlitic steel wire. *Metallurgical and Materials Transactions A*, 30A:717–727, 1999.

[92] J. Languillaume, G. Kapelski, and B. Baudelet. Cementite dissolution in heavily cold drawn pearlitic steel wires. *Acta Materialia*, 45(3):1201–1212, 1997.

[93] H. G. Read, W. T. Reynolds Jr., K. Hono, and T. Tarui. APFIM and TEM studies of drawn pearlitic wire. *Scripta Materialia*, 37(8):1221–1230, 1997.

[94] D. H. Shin, B. C. Kim, Y-S. Kim, and K-T. Park. Microstructural evolution in a commercial low carbon steel by equal channel angular pressing. *Acta Materialia*, 48:2247–2255, 2000.

[95] K. Hono, M. Ohnuma, M. Murayama, S. Nishida, A. Yoshie, and T. Takahashi. Cementite decomposition in heavily drawn pearlite steel wire. *Scripta Materialia*, 44(6):977–983, 2001.

[96] X. J. Hao, Z. G. Liu, K. Masuyama, T. Rikimaru, M. Umemoto, K. Tsuchiya, and S. M. Hao. Deformation and dissolution of spheroidal cementite in eutectoid steel by heavy cold rolling. *Materials Science and Technology*, 17:1347–1352, 2001.

[97] F. V. J. R. Nolfi, P. G. Shewmon, and J. S. Foster. Dissolution kinetics of Fe_3C in ferrite - A theory of interface migration. *Metallurgical Transactions*, 1:2291–2298, 1970.

[98] H. Abe, T. Suzuki, and J. J. Lavigne. Dissociation and dissolution of cementite in low-carbon steel by cold rolling and annealing. *Transactions ISIJ*, 21:332–337, 1981.

[99] M. F. Ashby and D. R. H. Jones. *Engineering materials 2.* Pergamon Press, Oxford, 1998.

[100] A. R. Cox. The tempering of steels: a review. *Iron and Steel*, 41:539–543, 1968.

[101] G. R. Speich. Tempering of low-carbon martensite. *Transactions of the A.I.M.E.*, 245:2553–2564, 1969.

[102] R. W. K. Honeycombe and H. K. D. H. Bhadeshia. *Steels, microstructure and properties, 2nd Edition.* Edward Arnold, London, 1995.

[103] ASTM. *Standard test methods for determining average grain size*, E-112-96 edition, 1996.

[104] J. H. Hollomon and L. D. Jaffe. Time-temperature relations in tempering steel. *Transactions T.M.S.-A.I.M.E.*, 162:223–249, 1945.

[105] Ph. Maynier, B. Jungman, and J. Dollet. *Hardenability concepts with applications to steels*, pages 518–545. eds. D. V. Doane and J. S. Kirkaldy, The Metallurgical Society of A.I.M.E., Warrendale, 1978.

[106] R. A. Grange, C. R. Hribal, and L. F. Porter. Hardness of tempered martensite in carbon and low-alloy steels. *Metallurgical Transactions A*, 8A:1775–1785, 1977.

[107] T. Réti, M. Gergely, and P. Tardy. Mathematical treatment of non-isothermal transformations. *Materials Science and Technology*, 3:365–371, 1987.

[108] M. Takahashi and H. K. D. H. Bhadeshia. Model for transition from upper to lower bainite. *Materials Science and Technology*, 6:592–603, 1990.

[109] W. S. McCulloc and W. H. Pitts. A logical calculus of the ideas immanent in nervous activity. *Bulletin of Mathematical Biophysics*, 5:115–133, 1943.

[110] D. Raabe. *Computational materials science.* Wiley-VCH, Weinheim, 1998.

[111] M. T. Hagan, H. B. Demuth, and M. Beale. *Neural network design.* PWS Publishing, Boston, 1996.

[112] H. K. D. H. Bhadeshia. Neural networks in materials science. *ISIJ International*, 39:966–979, 1999.

[113] D. J. C. MacKay. Probable networks and plausible predictions - a review of practical Bayesian methods for supervised neural networks. In http://wol.ra.phy.cam.ac.uk/mackay/.

[114] F. Tancret, H. K. D. H. Bhadeshia, and D. J. C. MacKay. Comparison of artificial neural networks with gaussian processes to model the yield strength of nickel-base superalloys. *ISIJ International*, 39:1020–1026, 1999.

[115] S. H. Lalam. *Modelling of mechanical properties of ferritic steel weld metals.* PhD thesis, University of Cambridge, Cambridge (UK), 2000.

[116] D. R. Poirier and G. H. Geiger. *Transport phenomena in materials processing.* The Minerals, Metals & Materials Society, Warrendale, 1994.

[117] H. S. Carslaw and J. C. Jaeger. *Conduction of heat in solids.* Oxford University Press, Oxford, 1959.

[118] J. Crank and P. Nicholson. A practical method for numerical evaluation of solutions of partial differential equations of the heat-conduction type. *Proceedings of the Cambridge Philosophical Society*, 43:50–67, 1947.

[119] S. Zhang and J. Jin. *Computation of special functions.* John Wiley & sons, inc, New York, 1996.

[120] W. C. Leslie. *The physical metallurgy of steels.* McGraw-Hill, New York, 1981.

[121] W. H. Press, B. P. Flannery, S. A. Teukolsky, and W. T. Vetterling. *Numerical recipes*. Cambridge University Press, Cambridge, 1986.

[122] M. Abramowitz and I. A. Stegun. *Handbook of mathematical functions*. Dover Publications, New York, 1972.

[123] D. G. Zill and M. R. Cullen. *Differential equations with boundary-value problems*. Brooks/Cole Publishing Company, Pacific Grove, 1997.

[124] T. M. R. Ellis. *Fortran 77 programming*. Addison-Wesley, Wokingham, England, 1990.

[125] C. Bonet, A. Jorba, M. T. M-Seara, J. Masdemont, M. Ollé, A. Susín, and M. València. *Càlcul numèri*. CPDA - Universitat Politècnica de Catalunya, Barcelona, 1991.

[126] M. Hillert. The formation of pearlite. In V. F. Zackay and H. I. Aaronson, editors, *Decomposition of austenite by diffusional processes*, pages 197–247. Interscience, New York, 1962.

[127] C. M. Sellars. Quantitative metallography. Technical report, Escuela Superior de Ingenieros Industriales de San Sebastian, 1981.

[128] L. C. Chang and H. K. D. H. Bhadeshia. Austenite films in bainitic microstructures. *Materials Science and technology*, 11:874–881, 1995.

[129] S. J. Jones and H. K. D. H. Bhadeshia. Competitive formation of inter- and intragranularly nucleated ferrite. *Metallurgical and Materials Transactions A*, 28A:2005–2013, 1997.

[130] C. Zener. Impact of magnetism upon metallurgy. *Transactions of the A.I.M.E.*, 203:619–630, 1955.

[131] L. Kaufman, E. V. Clougherty, and R. J. Weiss. The lattice stability of metals -III. Iron. *Acta Metallurgica*, 11:323–335, 1963.

[132] H. I. Aaronson, H. A. Domian, and G. M. Pound. Thermodynamics of the austenite - proeutectoid ferrite transformation. II Fe-C-X alloys. *Transactions of the A.I.M.E.*, 236:768–781, 1966.

[133] H. I. Aaronson, H. A. Domian, and G. M. Pound. Thermodynamics of the austenite - proeutectoid ferrite transformation. I Fe-C alloys. *Transactions of the A.I.M.E.*, 236:753–767, 1966.

[134] A. Prat, X. Tort-Martorell, and P. Grima. *Estadística teórica y aplicada: entregas 1 a 4.* C.P.D.A. - Universitat Politècnica de Catalunya, Barcelona, 1992.

[135] O. L. Davies. *Design and analysis of industrial experiments.* Oliver and Boyd, London, 1954.

[136] T. Sourmail. Neuromat Ltd.:Models manager, 2000.

[137] D. J. C. MacKay. Bayesian non-linear modelling with neural networks. In H. Cerjak, editor, *Mathematical modelling of weld phenomena 3*, pages 359–389. The Institute of Materials, London, 1997.

[138] J. Crank. *The mathematics of diffusion.* Oxford University Press, Oxford, 1975.

[139] T. Ericsson. The effect of final shaping prior to heat treatment. In G. Totten and T. Howes, M. Inoue, editors, *Handbook of residual stresses and deformation of steel*, pages 150–158. ASM International, Ohio, 2002.

[140] G. E. Dieter. *Mechanical metallurgy.* McGraw-Hill, London, 1988.

[141] Fuju Electronic Industrial Co, Ltd. *Thermecmastor-Z. Instruction manual*, 1986.

[142] S. V. Tsivinsky, L. I. Kogan, and R. I. Entin. Investigation of the distribution of chromium and tungsten during the decomposition of austenite, using the radioactive tracer method. In *Problems of metallography and the physics of metals.* Consultants Bureau, New York, 1959.

[143] S. A. Al-Salman, G. W. Lorimer, and N. Ridley. Pearlite growth kinetics and partitioning in a Cr-Mn eutectoid steel. *Metallurgical Transactions*, A10:1703–1709, 1979.

[144] J. Chance and N. Ridley. Chromium partitioning during isothermal transformation of a eutectoid steel. *Metallurgical Transactions*, A12:1205–1213, 1981.

[145] H. I. Aaronson and H. A. Domian. Partition of alloying elements between austenite and proeutectoid ferrite or bainite. *Transactions of the Metallurgical Society of A.I.M.E.*, 236:781–796, 1966.

[146] L. I. Kogan, G. M. Murashko, and R. I. Entin. Redistribution of elements during austenitization in the intercritical temperature range. *Physics of Metals and Metallography*, 58:115–120, 1984.

[147] M. Takahashi and H. K. D. H. Bhadeshia. A model for the microstructure of some advanced bainitic steels. *Materials transactions, JIM*, 32(8):689–696, 1991.

[148] J. W. Cahn. The kinetics of grain boundary nucleated reactions. *Acta Metallurgica*, 4:449–459, 1956.

[149] Hillert. M. The role of interface energy during solid state phase transformations. *Jernkontorets Annaler*, 141:757–789, 1957.

[150] M. Takahashi. *Reaustenitisation from bainite in steels.* PhD thesis, University of Cambridge. Department of Materials Science and Metallurgy, Cambridge, 1992.

[151] H. K. D. H. Bhadeshia. A rationalisation of shear transformations in steels. *Acta Metallurgica*, 29:1117–1130, 1981.

[152] G. I. Rees and H. K. D. H. Bhadeshia. Bainite transformation kinetics. Part 1 Modified model. *Materials Science and Technology*, 8:985–993, 1992.

[153] G. I. Rees and H. K. D. H. Bhadeshia. Bainite transformation kinetics. Part 2 Non-uniform distribution of carbon. *Materials Science and Technology*, 8:994–996, 1992.

[154] R. Trivedi. The role of interfacial free energy and interface kinetics during the growth of precipitate plates and needles. *Metallurgical Transactions*, 1:921–927, 1970.

[155] C. Zener. Kinetics of the decomposition of austenite. *Transactions of the A.I.M.E.*, 167:550–595, 1946.

[156] K. C. Russell. Linked flux analysis of nucleation in condensed phases. *Acta Metallurgica*, 16:761–769, 1968.

[157] H. K. D. H. Bhadeshia and D. V. Edmonds. The bainite transformation in a silicon steel. *Metallurgical Transactions A*, 10A:895–907, 1979.

[158] H. K. D. H. Bhadeshia and D. V. Edmonds. The mechanism of bainite formation in steels. *Acta Metallurgica*, 28:1265–1273, 1980.

[159] G. J. Shiflet, J. R. Bradley, and H. I. Aaronson. A re-examination of the thermodynamics of the proeutectoid ferrite transformation in Fe-C alloys. *Metallurgical Transactions A*, 9A:999–1008, 1978.

[160] H. K. D. H. Bhadeshia. *Bainite in steels.* The Institute of Materials, London, 1992.

[161] H. K. D. H. Bhadeshia. Thermodynamic extrapolation and martensite-start temperature of substitutionally alloyed steels. *Metal Science*, 15:178–181, 1981.

[162] H. K. D. H. Bhadeshia. Driving force for martensitic transformation in steels. *Metal Science*, 15:175–177, 1981.

[163] J. C. Fisher. The free energy change accompanying the martensite transformation in steels. *Metals Transactions*, 185:688–690, 1949.

[164] R. W. Hertzberg. *Deformation and fracture mechanics of engineering materials.* John Wiley & sons, inc., New York, 1996.

[165] M. Hillert. The kinetics of the first stage of tempering. *Acta Metallurgica*, 7:653–658, 1959.

[166] C. Zener. *Elasticity and anelasticity of metals.* University of Chicago Press, Chicago, 1948.

[167] Y. Iijima. Magnetic effect on diffusion of carbon and nitrogen in iron. *Journal of alloys and Compounds*, 234:290–294, 1996.

[168] J. P. Jakubovics. *Magnetism and magnetic materials.* The Institute of Materials, London, 1994.

Appendix A

MAP documentation of software developed